SAPIENZA
UNIVERSITÀ DI ROMA

FACOLTÁ DI INGEGNERIA CIVILE E INDUSTRIALE
DOTTORATO DI RICERCA IN INGEGNERIA DELLE STRUTTURE
XXVIII CICLO

Modeling and Characterization of the Mechanical and Damping Response of Carbon Nanotube Nanocomposites

PHD CANDIDATE:
MICHELA TALÓ

ADVISOR:
PROF. WALTER LACARBONARA

PHD COORDINATOR:
PROF. ACHILLE PAOLONE

ROME, NOVEMBER 2016

To everyone who supported, believed, care and guided me during this path: family, friends, colleagues and mentors.

ABSTRACT

Modeling and Characterization of the Mechanical and Damping Response of Carbon Nanotube Nanocomposites

Multifunctionality is a current trend in material design. The fast growing needs of industries are challenging the design of structures made of advanced lightweight composites that possess the capability of performing multiple functions. The superior mechanical properties of carbon nanotubes (CNTs) – besides the excellent electrical and thermal properties – make them ideal candidates to be used as reinforcement fillers in composite materials. CNT nanocomposites, made of suitable polymeric matrices filled with carbon nanotubes, have shown enhanced mechanical and electrical features with an additional extraordinary feature, namely, a high structural damping capacity.

The main objective of this work is to explore the mechanical and damping response of CNT nanocomposites, aiming at reaching a better understanding of the macroscopic behavior of the nanocomposite materials by taking into account their complex micro/nanostructural features.

The practical goal is to effectively explore the potential exploitation of these nanostructured materials in demanding structural applications.

In order to investigate and optimize not only the mechanical properties but also the damping capacity of CNT/polymer composites, a specific analytical model, based on the Eshelby and Mory-Tanaka approaches, is here presented.

The proposed model is an effective tool for predicting nonlinear stress-strain curves, energy dissipation mechanisms and hysteresis of nanocomposite materials. A great deal of studies were conducted on the ability of CNT-reinforced materials to absorb vibrations and noise (*damping capacity*), analyzing the orientation, dispersion and aspect ratio of CNTs as main parameters that affect the mechanical and damping properties.

As a step forward from the current state of the art, the present work suggests an innovative theoretical method to describe the macroscopic response of nanocomposites and explore energy dissipation mechanisms arising from the shear slippage of nanotubes within the hosting matrix. The major mechanism through which energy is dissipated, the *stick-slip mechanism*, can be properly treated by introducing a plastic eigenstrain in the CNT inclusions whose evolutive law is accordingly shaped after the physical phenomenology.

A set of numerical tests are performed to estimate the elastic properties and the nonlinear response of nanocomposites, characterizing the hysteresis loops in the stress-strain curves. Parametric studies are conducted to investigate the influence of the main constitutive parameters of the model on the mechanical response including the damping capacity. The numerical simulations revealed that the interfacial shear strength, the CNT volume fraction, the exponent of the evolution law for the plastic eigenstrain, as well as the strain amplitude, have a significant effect on the hysteresis of CNT nanocomposites.

Moreover, it is shown that an optimal combination of these micro-structural parameters can be achieved via differential evolutionary algorithms that allow to maximize the damping capacity, while preserving the high elastic properties of the nanostructured materials. Such approach further enables the calibration of the model and design the nanomaterial in order to provide an effective response according to the structural vibration control requirements and high mechanical performance goals.

The validation of the effectiveness of the predictive computational tool, together with its theoretical framework, is also sought via an ad hoc experimental approach.

The experimental campaign of featuring mechanical tests on a variety of CNT nanocomposite materials was indeed a fundamental step towards the refinement of the model and a reasonable tuning of the model parameters. In addition, a morphology investigation of the prepared CNT/polymer composites was a decisive step to define the microstructural properties.
The experimental activities highlighted and confirmed the relevance of several morphological aspects, such as the actual CNT aspect ratio variability within the nanocomposite, the CNT dispersion and agglomeration degree and the polymer matrix chemical structure, to mention but a few. Those results shed light to which nanocomposites constituents features can influence the macroscopic response of the material. The conducted experimental work aimed also at identifying and introducing parameters that can better enhance the nanocomposite mechanical and damping behavior, by investigating also aspects of the fabrication processes that can help improve the CNT dispersion or the CNT adhesion like, for instance, the CNT functionalization.
These experimental findings allowed a final model update by overcoming the main limitations, generally present in the most common micromechanical theories for multi-phase materials, i.e., (i) the perfect nanofiller dispersion and distribution in the surrounding matrix, and (ii) the perfect interfacial adhesion between the carbon nanotubes and polymer chains.

Contents

List of Figures

List of Tables

Chapter 1

Introduction, Background and Objectives

1.1 Introduction

The design of high-performance multi-functional composite materials represents the current challenge in material science and engineering.
In recent years, the conducted research and studies on the remarkable mechanical, thermal and electrical properties of *carbon nanotubes (CNTs)*, suggested their use as ideal fillers for reinforcement of polymer-based materials, opening horizons for a new generation of nanostructured composites. In fact, CNTs/polymer composites demonstrated to fulfill not only the mechanical and structural requirements but also more advanced and special needs of the growing industry, such as fire reaction and vibro-acustic requirements.
Among the major properties exhibited by these materials, their ability to absorb and dissipate energy, typically referred to as the *damping capacity*, turns out to be the most astonishing, in particular, in view of the many potential applications in aerospace, automotive and structural engineering.
The damping capacity has become a necessary feature for a variety of composite structures as well as dynamic components, in order to reduce and contain vibrations and noise. Such a capability of converting the mechanical energy - introduced into the system by vibrations - into heat, leads to enhancements in performance, safety and reliability of structures.
In order to analyze the main features of the CNT nanocomposites, first the various, significant properties of carbon nanotubes are assessed by trying to understand what make them an extremely valuable reinforcement for composite materials.

1.2 Carbon nanotubes features

The tubular fullerene structures (CNTs), discovered by Iijima in 1991, today, represent a great promise for potential industrial applications. Carbon nanotubes (CNTs) are the strongest nano-fibers currently known, and exhibit several special properties that were not found in any other material before.

1.2.1 Hystory of CNTs

In 1985 Robert Curl, Richard Smalley and Harold Kroto discovered that carbon exists, in the nature, in a third form besides graphite and diamond. They found strange results in mass spectra of evaporated carbon samples, obtaining a new compound made of C-atoms placed in hexagons and pentagons. The combination of these arranged and bonded C-atoms rings, gives rises to closed-cages with a minimal local curvature and surface stress, called *fullerenes*. The smallest stable structure of fullerene, made in this way, is C_{60}, also termed buckyball; it is a nanometer-size ball made of 60 carbon atoms. This revolutionary discovery earned Curl, Smalley and Kroto the Nobel Prize in chemistry (1996).
The discovery of fullerenes is closely connected with that of carbon nanotubes. In 1991 Iijima and coworkers investigated carbon deposits produced by an electric arc discharge technique [51]. By the employment of a high-resolution transmission electron microscopy (TEM), they observed the existence of cylindrical graphene structures with closed ends, which are now known as CNTs. Carbon nanotubes are a kind of fullerene structure; in particular, they are constituted of a graphene sheet rolled up in a certain direction, forming a closed cylinder. The importance of Iijima's work lies in having pointed out the exceptional properties of these nanostructures, discovering and identifying also multi-walled and single-walled nanotubes. The Single Walled Nanotubes (SWNTs) are the most interesting finding since they are the basis of a large number of theoretical studies and predictions in many engineering fields.
Their large length ($1 \div 500\,\mu m$) and small diameter ($1 \div 90\,nm$) lead to a large aspect ratio ($\alpha = L/D$), usually grater than 1000; thus, they can be seen as the nearly one-dimensional form of fullerenes. Such a particular one-dimensional structure characterizing CNTs, confers to this nanomaterial additional superior electrical, mechanical and chemical properties, that will be examined in the next sections.

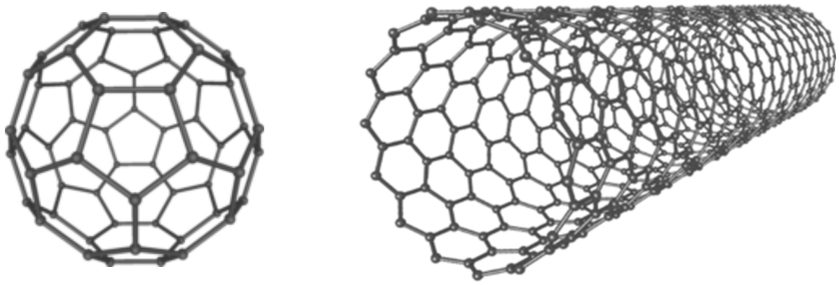

Figure 1.1: Fullerene structures: buckyball (on the left), single-walled carbon nanotube (on the right).

1.2.2 Synthesis of CNTs

Several techniques can be used to produce carbon nanotubes but the growth mechanism, which seems to be almost the same for each fabrication process, is still not exactly known. Three of these synthesis methods represent the most important and are widely used: arch discharge, laser ablation and chemical vapor deposition.
In arch discharge technique, an electric arch between two graphite electrodes is generated. While the anode is usually filled with a catalyst, carbon nanotubes self-assemble at the

cathode. In laser ablation, a high-power laser is used to vaporize a compound consisting of graphite and catalyst, at very high temperatures. This technique synthesizes CNTs with high purity. Finally, in chemical vapor deposition (CVD), gaseous molecules, called precursors, are employed at high temperature and pressure; thus, they become solid materials and deposit on a substrate, where CNTs are produced.
All the methods described are in continuous development and each of these fabrication processes offers specific advantages and disadvantages, implying some critical problems, such as scalability, purity and costs. Moreover, various processing parameters are involved in synthesis of single- or multi-walled carbon nanotubes and the particular setups and surrounding conditions, such as temperature and pressure, can improve the quality of the CNTs produced or can generate defects in the molecular structure of the nanomaterials.

1.2.3 Structure and special properties of CNTs

A carbon nanotube consists of a cylindrical central structure composed of a graphene sheet wrapped in a specific direction and, at least, one end cap for the tube, derived from a hemisphere of a fullerene buckyball, such as C_{60}. In order to form a closed cylinder, the graphene sheet can be rolled up in a discrete set of directions, obtained by choosing two reference atoms in the graphene plane and connecting them. The vector pointing from the first C-atom towards the second is called chiral vector and identifies the rolling angle. The chiral vector is characterized by two integer numbers (n, m), that indicate the periodic disposition of the C-atoms around the nanotube axis. Together with the diameter of CNT, the preferential rolling direction determines the main properties of the nanomaterial. If $n = m$ the nanotube is called armchair and behaves as a metal conductor; if $m = 0$, it is called zigzag, otherwise it is called chiral and, generally, both behave as semiconductors. From the chiral vector and, hence, the rolling angle depend the optical activity, mechanical strength and, in particular, electrical and thermal conductivity of CNTs.
Carbon nanotubes, indeed, exhibit remarkable **thermal** and **electrical properties**. They

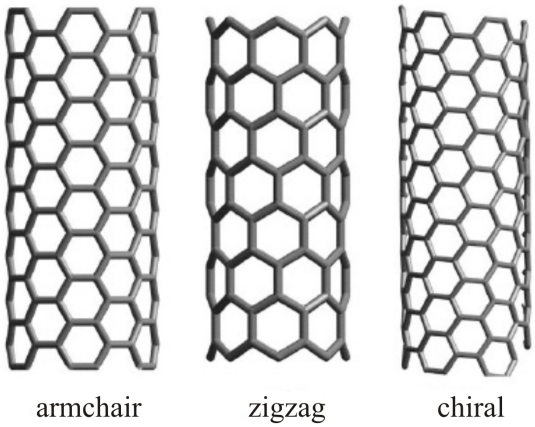

Figure 1.2: Carbon nanotubes with different rolling angles.

are excellent thermal conductors along the tube axis, but very good insulators laterally to the tube and can withstand very high temperatures without being subjected to chemical structure modifications. This property may be useful for thermal management applications, such as heat sinking of silicon processors and other types of heat dissipation. Furthermore, the superior electrical conductivity and mechanical properties of CNTs suggest their use in

nano-devices, for instance, in integrated circuits built with nanotube transistors, or even in manufacturing high-performance supercapacitors for energy storage, as well as sensors for monitoring and measuring environmental conditions [53].

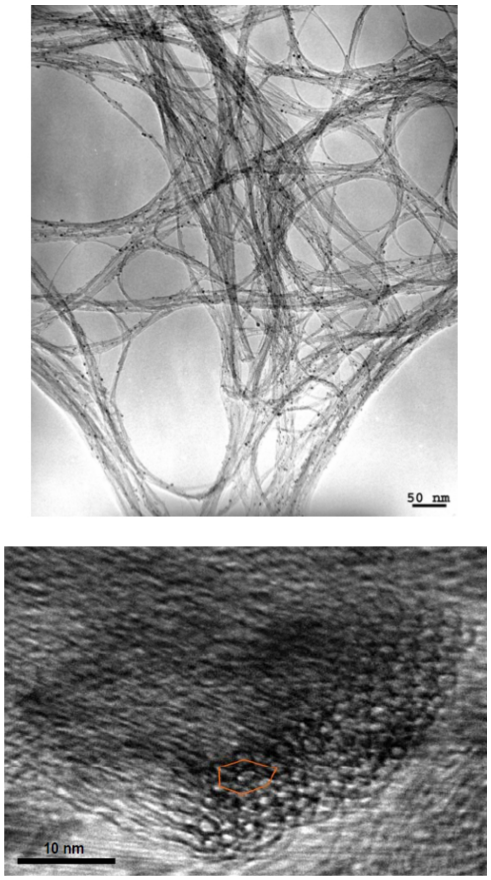

Figure 1.3: Single walled carbon nanotubes are observed using the Transmission Electron Microscopy (TEM). The tubular structures, that carbon atoms bonding together form, are well visible.

Finally, we have to focus on the outstanding **mechanical properties** of carbon nanotubes, which depend on the nature of bonds between C-atoms. The strong covalent (in-plane) bonding of C-atoms is responsible for the high stiffness and strength of this nanomaterial. In fact, CNT is the strongest and stiffest material yet discovered in terms of tensile strength and Young modulus, that rivals even diamond. Tensile strength of SWCNTs was theoretically investigated and can reach values of 100 GPa and the Young modulus has been estimated, by Atomic Force Microscopy (AFM), to be of the order of 1 TPa [91], while the Young modulus of conventional carbon fibers is around 500-800 GPa. Moreover, due to their large aspect ratio, they are also extremely flexible and have much lower specific weight and mass density of steel and many other reinforcement materials, suggesting their use in structural and aerospace engineering applications, for instance, for aircraft fuselages or space elevators.
Considering all these extraordinary characteristics, carbon nanotubes are the natural choice as reinforcement fillers for polymer materials.

1.3 CNT-reinforced composites: a literature review

By incorporating a low volume fraction of carbon nanotubes into a polymer matrix, a nanocomposite material with dramatically improved properties is produced. CNT-reinforced composites are being used for an increasing number of advanced industrial applications, in particular, because of the multi-functionality of these nanostructured materials, that was proved and intensively investigated in the last decades.

1.3.1 Mechanical and damping behavior of CNT-based composites

As described in section 1.2.3, CNTs possess excellent mechanical properties with a Young modulus as high as 1.3 TPa and a tensile strength of 50–200 GPa [54]. The combination of these high mechanical properties along with the low density, high aspect ratio and high surface area to volume ratio, make the CNTs ideal candidates for reinforcement in composite materials. Both SWCNTs and MWCNTs have been used to reinforce thermosetting polymers, such as epoxy [10, 58], polyurethane, and phenol-formaldehyde resins, as well as thermoplastic polymers, including polyethylene, polypropylene [63], polycarbonate [23, 61], and other high performance engineering polymers, such as nylon [9] or poly-ether-ether-ketone [68]. The CNT-reinforced nanocomposites can be considered a kind of particular composites with filler dimensions on the nanometer scale and the aspect ratio as high as 1000.
The mechanical properties of nanocomposites are strongly dependent on the *aspect ratio* of the CNTs. A high aspect ratio can, in fact, maximize the elastic modulus and tensile strength of the material, since continuous and long nanotubes allow a better adhesion at the CNT/matrix interface and, consequently, a better transfer of the shear stresses at the interface. But a strong interface may not be an advantage for enhancing damping properties. Since recent studies showed that damping capacity is primarily dependent on the interfacial bond strength between CNT and matrix, apart from the great contribution of a large interfacial area of CNTs, the loss factor characteristic of the nanomaterial can be further improved using discontinuous nanotubes with low aspect ratio. This is also confirmed by the results of pull-out tests of carbon nanotubes and using Atomic Force Microscopy (AFM) to observe the chemical bonds at the CNT/matrix interface [35].
In addition to the CNTs aspect ratio, there are other major requirements that need to be satisfied for effective reinforcement of CNTs in composites. These requirements include a good dispersion of CNTs, a preferential alignment of CNTs in the loading direction, and interfacial interactions between the CNT and polymer matrix. A good *CNT dispersion* is one of the most important issues in the manufacturing of CNT/polymer nanocomposites. Many different techniques have been employed for improving CNT dispersion [59, 80]. A good and homogeneous CNTs dispersion not only makes more filler surface area available for bonding with the polymer matrix, but also prevents that the filler aggregations act as stress concentrators [7]. Hence, this feature represents an important requirement for the mechanical properties as well as for the damping capacity of the composite.

Furthermore the *alignment* of CNTs is necessary to maximize the strength and elastic modulus in a certain direction, but it is not always beneficial because the aligned CNT composites tend to have highly anisotropic properties, that is, the mechanical properties along the alignment direction can be enhanced, whereas these properties are sacrificed along the direction perpendicular to this orientation. However, for the design of specific damping properties of a nanomaterial, the perfect alignment of the nanofibers in a preferential direction allows to fabricate particular dynamic components that are subjected to a specific directional load.

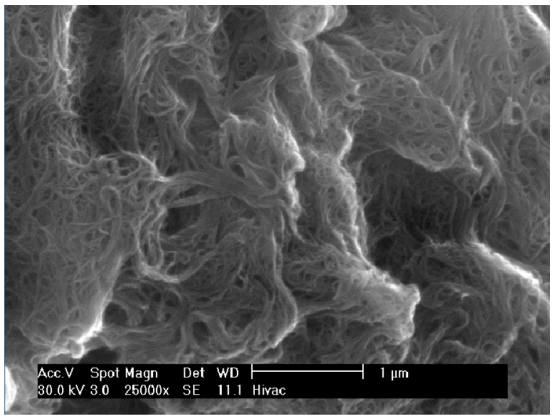

Figure 1.4: Dispersion of single walled carbon nanotubes observed using the Scanning Electron Microscopy (SEM).

As for fiber-reinforced composites, another important requirement for CNT nano-composites for any structural application, is the efficient transfer of the external load applied to the composite, to the nanotubes, allowing them to take up the major share of the load. The *load transfer* depends on the *interfacial bond* between the CNT and the matrix, in the same way as in fiber composites. If the composite is subjected to a load and there is a perfect bonding between the CNTs and the matrix, then the load can be transferred to the CNTs. Since the strength of CNTs is much higher than that of the matrix, the composite can withstand high loads, resulting in improved mechanical properties. In contrast, if the CNT-polymer interfacial bond is weak, then the interface would debond prematurely; thus the composites exhibit a lower strength and ultimate deformation at break. Many specific chemical and physical functionalization techniques have been shown to be efficient in enhancing interfacial interactions between CNTs and various polymers [86, 75].
As already anticipated, while a strong interface enhances the mechanical features of CNT-composites, the dominant factor that affects the damping mechanisms and ability of these nanocomposites is the *frictional energy dissipation* due to a weak bonding at interfaces between the constituents of the multi-phase material.
Damping describes the ability of the material to absorb vibrational energy and reduce the amplitude of induced oscillations. The damping properties of nanocomposites can be measured by loss factor and damping ratio, essential design parameters for many engineering applications. High damping properties can be achieved in nanocomposites by taking advantage of the interfacial friction between the nanofillers and the polymer matrix [30]. The combination of extremely large surface area, weak interfacial bonding with the polymer, along with low mass density of the CNTs implies that frictional sliding of nanotubes with the matrix causes significant dissipation of energy with a minimal weight penalty and provides a high damping capability in the CNT-filled polymer. Recent studies have shown that the damping properties of polymer nanocomposites were enhanced by more than 200% by incorporating a very small amount of CNTs.
The mechanism behind this enhancement can be explained by shear lag theory and *stick-slip theory*. When the nano-composite is subjected to an external load, the composite starts elongating and shear stresses are generated between the CNT walls and the surrounding matrix due to the difference in their elastic properties. The load is transferred to the CNTs, which starts to elongate accordingly with the matrix, if they are well bonded *(sticking phase)*. As the external load exceeds a critical value, leading to debonding of CNTs from the matrix,

the CNTs will stop elongating together with the matrix and a further increase of the load can only result in the deformation of the matrix. Thus, the polymer starts to flow over the surface of CNTs and deformation energy will be dissipated through the slippage between the CNTs and the matrix *(slipping phase)* [84]. This phenomenon leads to the enhanced damping properties of nano-composites compared to the neat polymer.
There are several factors governing the damping properties of CNT/polymer nanocomposites. First, a weak interfacial adhesion plays an important role in enhancing the dissipative properties of CNT composites, although it is detrimental to the mechanical properties of CNT/polymer composites. Then, the effects of a good CNT dispersion on the damping properties of the nanomaterial shows a trend similar to their elastic mechanical properties; on the contrary, the aspect ratio has an opposite effect on the two main features of the material, requiring a compromise on the basis of the functions that the composite needs.
Finally, in order to understand which kind of nanotubes is more appropriate to enhance the damping properties of the composite, we can refer to some studies conducted by Suhr et al. [82, 87] on the resulting properties shown by nanocomposites filled with SWCNTs and MWCNTs. While both types of CNTs give rise to higher damping than that obtained with the neat polymer, the loss modulus of the nanocomposite containing SWCNTs is significantly higher than that filled with MWCNTs, suggesting that the inner walls of the MWCNTs do not contribute to interfacial frictional sliding for energy dissipation. This is the reason for which, in this work, dispersed SWNTs have been suggested as the ideal reinforcement for polymer matrix.

1.3.2 Analytical models for CNT nanocomposites

In addition to the numerous studies and tests conducted in the last decades on the effective mechanical properties of CNT composite materials [3, 4, 15, 24, 25, 31, 47, 66, 68, 97], a considerable amount of experimental data was obtained to either characterize the interfacial CNT-matrix properties or to measure the damping capacity of these promising nanostructured materials [1, 5, 17, 28, 32, 34, 46, 73, 82, 89]. Indeed, it was proved that a low interfacial shear strength (ISS) between the CNTs and the hosting matrix together with a high interfacial contact area results in a significant increase of damping capacity [61, 65, 83, 87].
Rajoria and Jailili [74] showed that the low adhesion at the nanotubes-polymer interface together with a good alignment and dispersion of the CNTs maximize the damping capacity of the nanocomposites, observing in a series of vibration tests an increase up to 700% of damping ratio in epoxy composites integrated with 5% weight fraction of multi-walled carbon nanotubes. They assumed a stick-slip model to describe the main source of energy dissipation arising from the ability of the CNTs to slide inside the matrix.
Suhr et al. [84] showed how mechanical damping is related to the frictional energy dissipation during interfacial sliding all over the high contact areas between nanotubes and polymeric matrix, and discussed the effects of the applied strain amplitude on the interfacial slippage of CNTs.
Other relevant works investigated extensively the influence of some key parameters on the nanocomposite damping behavior, such as CNT volume fraction, surface treatments for the interfacial adhesion, dispersion and geometry of CNTs, showing that the loss modulus may increase up to 1000% with only 2% weight fraction of SWCNT fillers [1, 5, 55, 79].
In the context of the frictional energy dissipation phenomenology, as mentioned, the combination of an extremely large interfacial area and the weak CNT/matrix interfaces are the key physical aspects that give rise to improved hysteretic behavior [44], thus emphasizing the importance of constitutive parameters such as the CNT volume fraction and the interfacial

shear strength [76]. The mechanism behind this damping enhancement can be explained by the stick-slip theory as suggested by previous works.
Zhou et al. [99] developed a stick-slip damping model for aligned, well-dispersed SWCNT/polymer composites extending the stick-slip phenomenon observed at the atomic scale by [13] and [39] to the nanotube-resin interface. The damping model was later expanded by Liu et al. [57] in a three-phase micromechanical model, composed of resin, resin sheath acting as shear transfer zone, and CNT rope. More recently, an effective model incorporating the stick-slip mechanism for unidirectional nanocomposites has been proposed by Dwaikat et al. [20] to determine the hysteretic energy dissipation. They considered the effects of the CNT volume fraction, aspect ratio and fiber-to-matrix stiffness ratio on the damping capacity, and then adopted an optimal set of parameters to maximize the frictional energy dissipation. This result suggested the possibility to design and optimize CNT nanocomposites for advanced damping applications.
Following the same idea of designing ultra-damping materials to meet the high demands for innovative vibration and noise control systems, other interesting friction models for the interfacial energy dissipation in CNT composites have been proposed by Huang [41] and Lin [56].
At the same time, due to their low density, high stiffness and tensile strength, CNTs turn out to be a truly attractive reinforcing agent for metals, polymers or ceramics. This interest inspired the development of constitutive models capable of describing not only the CNT-matrix interface features, but also the overall nonlinear behavior of these nanostructured materials. These models exploited molecular dynamics using both atomistic and continuum theories. Over the past decade, several multi-scale models have been proposed to elucidate the influence of the CNT volume fraction, agglomeration, orientation and interfacial conditions on the overall mechanical properties of CNT composites [3, 4, 28, 67] leading to effective nonlinear elastoplastic constitutive models addressing issues such as agglomeration and load transfer at the CNT-matrix interface [43, 85, 88, 95, 96].
Among these works, the relevant study of Barai et al. [8] deals with the elastoplasticity of CNT composites described by a two-scale model, where an imperfect interface (spring-like) model is adopted at the smaller scale. Moreover, starting from the early works of Hill [38] and Mori and Tanaka [62], incremental elastoplastic meso-mechanical constitutive models were later developed. In particular, Gonzalez et al. [33] adopted the self-consistent method [38] to compute the elastoplastic behavior of a two-phase material considering the effects of a stress redistribution due to damage evolution, while [18] proposed a new incremental homogenization formulation featuring consistent tangent and secant operators to analyze the cyclic deformation of composite materials. These rich analytical models have been recently extended in several works [19], [36], [72] by developing finer cyclic visco-plastic constitutive models to describe hysteretic behaviors.
Finally, interesting attempts have been pursued to develop models that may incorporate dissipative mechanical features of the nanocomposites, including a multi-scale, mass-spring model [29] for foam materials integrated by carpets of unidirectional CNTs, where the dynamic dissipation shown by the material under cyclic compressive loading is accompanied by hysteresis and strain localization. The macroscopic hysteresis is interpreted as a rate-independent phenomenon that describes the damping and elastoplastic behavior of the nanocomposite.
Various other works were carried out by other authors and can be found in the literature. The present work aims to define a new analytical model, based on the main principles of continuum micro-mechanics, and describe the structural hysteretic dissipation mechanism. The fundamental principles, from which the theoretical model is derived, are defined in the Eshelby and Mori-Tanaka theory presented in the next chapter.

1.4 Objectives

The main objective of this work is to explore the mechanical and damping response of CNT nanocomposites, trying to reach a better understanding of the macroscopic behavior of CNT/polymer composites by taking into account their complex microstructural features.
The idea is to effectively estimate the potential of these nanostructured materials and envision their possible use in important structural applications, leveraging – as already mentioned – on their multi-functional properties.
Among the goals of the research work, the most important is to develop a nonlinear constitutive model able to incorporate and describe not only the mechanical properties but also dissipative and morphological features of CNT composites. The aim is to provide an effective predictive tool by which the mechanical properties and the damping mechanism, due to the stick-slip at the CNT/matrix interfaces, can be accurately described.
The approach adopted for this work is both theoretical and experimental. An accurate study about the most accredited theories for multi-phase materials is first conducted and one of the most popular theories of nano and micromechanics – the Eshelby and Mory-Tanaka theory – is employed as starting point for the development of a novel nonlinear meso-scale theory.
The proposed model is characterized by several micro- and macro-structural parameters, accounting for morphological and mechanical properties of the nanocomposites. To verify and validate the model as well as to directly investigate the material properties of the CNT/polymer composites, an experimental campaign is essential.
The experimental activities have the purpose of characterizing the nanocomposites materials through morphological analysis and mechanical tests. The experimental outcomes highlighted and confirmed the relevance of several aspects, such as the CNT aspect ratio, CNT dispersion, polymer matrix chemical structure, and shed light on how the properties of the nanocomposite constituents may influence the global response of the final material. The conducted experimental work had also the aim of identifying the parameters that could better enhance and optimize the nanocomposite mechanical and damping behavior, by investigating also the fabrication processes that could help to improve the CNT dispersion and the interfacial adhesion like, for instance, the CNT functionalization.

1.5 Outline

This work is organized as follows. In this Chapter, a first overview of the multifunctional properties of the CNTs was provided, as well as a state of the art on the experimental and modeling efforts already done to identify and describe the mechanical and dissipative properties of CNT nanocomposites. In Chapter 2, the Eshelby theory and Mori-Tanaka approach are exposed and discussed to introduce the main concepts on which the developed nonlinear stick-slip model is based. The Eshelby tensor is introduced in its general form and the Eshelby equivalent inclusion method is discussed together with the Mori and Tanaka average stress and strain theorem.
In Chapter 3, the novel nonlinear constitutive model is presented. The plastic eigenstrain field, that includes the interfacial stick-slip effects on the damping response of the CNT nanocomposites, is introduced and the constitutive equations of the model are cast in incremental form. Several sensitivity and parametric analysis are conducted in order to assess the influence of each model parameter. Furthermore, an optimization genetic algorithm is used to optimize the model parameters and lead to a guiding tool for the design of the mechanical and damping properties of the nanocomposites.

Starting from Chapter 4, the experimental activities are presented. In particular, Chapter 4 deals with the material features and the fabrication processes adopted to prepare a large variety of CNT nanocomposites samples to be characterized and tested.
Chapter 5 reports the accurate morphology characterization of the prepared samples conducted via optical light microscopy, SEM and TEM analysis in order to assess the nano- and macro-dispersion of the CNTs in the polymers and characterize the CNTs morphology, namely, the aspect ratio and shape. In Chapters 6 and 7 the mechanical and damping properties of the prepared nanocomposites are presented, respectively. A set of experimental mechanical quasi-static and dynamic tests were conducted via monotonic and cyclic tensile tests (Chap. 6) and DMA analysis (Chap.7). The most relevant findings are highlighted and exploited to better understand the nanocomposites mechanical response.
In Chapter 8, an update of the proposed theoretical model is attempted, driven by the experimental data. Interesting adjustments of the model developed in Chapter 3 are presented and discussed. The model is updated by exploiting the most relevant experimental outcomes, trying to overcome two of the most strong and not always reliable assumptions that are made in common multi-phase material models: (i) perfectly well dispersed and distributed nanofillers, and (ii) perfect adhesion between the nanofiller and the hosting matrix.
Finally, Chapter 9 summarizes the main issues addressed during this study and reports the final goals achieved by this theoretical and experimental work.

Chapter 2

Modeling CNT Nanocomposites: Eshelby and Mori-Tanaka Theories

2.1 Introduction

The most popular analytical modeling tools, available for predicting the mechanical properties of nanostructured materials, include Voigt and Reuss bounds, Hashin and Shtrikman bounds, Halpin-Tsai model, Cox model, and Eshelby and Mori-Tanaka models. Among these approaches, the Eshelby and Mori-Tanaka theories are employed in this work since are considered as foundational theories of nano and micromechanics. Several important problems in microelasticity, related to inclusions, dislocations, inhomogeneities, fractures and voids, are solved using the equivalent inclusion method proposed by Eshelby and the results are often generalized via the stress average theorem by Mori and Tanaka. This approach, also called EIAS (Equivalent Inclusion - Stress Average) method [12], has been widely used to compute the effective properties of composite materials and describe their mechanical behavior.

In order to introduce the Eshelby theory, the definition of eigenstrain is given first. An *Eigenstrain* is generally a nonelastic strain, such as thermal expansion, initial strain, plastic strain and misfit strain, defined in a sub-domain $\mathcal{B}_I$ of a body $\mathcal{B}$. The *Eigenstress* that derives from the application of the eigenstrain is the self-equilibrated internal stresses due to the mentioned eigenstrain in a body which is free from any other external force or surface constraint.
Consider an infinitely extended, linearly elastic homogeneous and isotropic body which occupies a reference configuration represented by the three-dimensional domain $\mathcal{B}$ in its stress-free (natural) state. When an eigenstrain E^*_{ij} is prescribed in a finite sub-domain $\mathcal{B}_I$ (with the same elastic moduli of the domain $\mathcal{B}$) and it is zero in the remaining domain $\mathcal{B}_M = \mathcal{B} - \mathcal{B}_I$, then $\mathcal{B}_I$ is called *inclusion* and $\mathcal{B}_M$ is called *matrix*.
If a sub-domain $\mathcal{B}_C$ in a material $\mathcal{B}$ has elastic moduli different from those of the matrix, then $\mathcal{B}_C$ is called *inhomogeneity*. In this case, a space-varying stress field, due to the existence of the inhomogeneity, can be simulated by an eigenstress field, given as the result of a fictitious eigenstrain field E^*_{ij} in the sub-domain $\mathcal{B}_C$ of a homogeneous material.

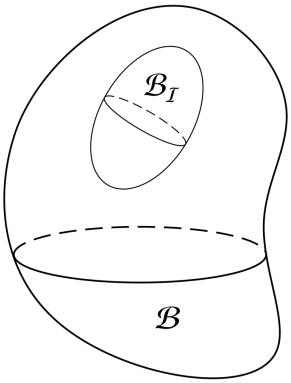

Figure 2.1: An inclusion $\mathcal{B}_I$ in a domain $\mathcal{B}$

The Eshelby theory provides solutions for all these eigenstrain problems, reviewing the fundamental equations of the elasticity theory. In fact, many problems consist of finding displacement, strain and stress fields at an arbitrary point x of the domain when it is subject to a given distribution of eigenstrains E^*_{ij}.

2.1.1 Fundamental equations of elasticity

The general equations of elasticity are here reviewed before introducing the eigenstrain method. Assuming $\mathcal{B}$ to be a linearly elastic homogeneous and isotropic material, the strain-displacement relationships are given by

$$\boldsymbol{E} = \frac{1}{2}\left((\nabla \boldsymbol{u})^\top + \nabla \boldsymbol{u}\right) \tag{2.1}$$

where $\boldsymbol{E}$ is the strain tensor and $\boldsymbol{u}$ is the displacement vector. Then, the constitutive relation is given by $\boldsymbol{T} = \boldsymbol{L} : \boldsymbol{E}$, where $\boldsymbol{T}$ is the stress tensor and $\boldsymbol{L}$ is the elastic tensor (or stiffness tensor, containing the elastic moduli), which can be also expressed using the Lamé constants as

$$\boldsymbol{T} = \lambda \operatorname{tr}(\boldsymbol{E})\boldsymbol{I} + 2\mu \boldsymbol{E} \tag{2.2}$$

and the equation of motion is written as

$$\boldsymbol{\nabla} \cdot \boldsymbol{T}^\top + \boldsymbol{b} = \rho \boldsymbol{u}_{tt} \tag{2.3}$$

where $\boldsymbol{b}$ indicates the volume forces and ρ is the mass density.
Substituting equation (2.1) into (3.2) we get

$$\boldsymbol{T} = \lambda \operatorname{tr}(\nabla \boldsymbol{u})\boldsymbol{I} + \mu\left((\nabla \boldsymbol{u})^\top + \nabla \boldsymbol{u}\right) \tag{2.4a}$$

$$\boldsymbol{T}^\top = \lambda \operatorname{tr}(\nabla \boldsymbol{u})\boldsymbol{I} + \mu\left(\nabla \boldsymbol{u} + (\nabla \boldsymbol{u})^\top\right) \tag{2.4b}$$

and using (2.4b) for $\boldsymbol{T}^\top$ in (2.3), we obtain the Navier equation where $\boldsymbol{u}$ is the only unknown

$$(\lambda + \mu)\boldsymbol{\nabla} \cdot (\nabla \boldsymbol{u})^\top + \mu \nabla^2 \boldsymbol{u} + \boldsymbol{b} = \rho \boldsymbol{u}_{tt} \tag{2.5}$$

Since the term $\rho \boldsymbol{u}_{tt}$ can be assumed to be zero in the static case, equation (2.5) becomes

$$(\lambda + \mu)\boldsymbol{\nabla} \cdot (\nabla \boldsymbol{u})^\top + \mu \nabla^2 \boldsymbol{u} + \boldsymbol{b} = \boldsymbol{0}. \tag{2.6}$$

2.1.2 The method of Green's functions in elasticity

If the body force is assumed to be an external point force $\boldsymbol{Q}$ acting at $\boldsymbol{x}$ within the infinitely extended homogeneous domain $\mathcal{B}$, the Green's function method can provide the following solution to the elastic problem.
The external point force $\boldsymbol{Q}$ is a concentrated force that can be expressed using the three-dimensional Dirac delta function $\delta(\boldsymbol{x})$ which is zero everywhere, except at $\boldsymbol{x} = \boldsymbol{0}$. By considering just the static problem, it is possible to rewrite the Navier equation given by (2.6) as

$$(\lambda + \mu)\boldsymbol{\nabla} \cdot (\nabla \boldsymbol{u})^{\top} + \mu \nabla^2 \boldsymbol{u} + \boldsymbol{Q}\delta(\boldsymbol{x}) = \boldsymbol{0} \tag{2.7}$$

or, using the tensorial indicial notation, in the form

$$(\lambda + \mu)\frac{\partial}{\partial x_j}\left(\frac{\partial u_i}{\partial x_i}\right) + \mu \nabla^2 u_j + Q_j \delta(\boldsymbol{x}) = 0 \tag{2.8}$$

To solve this equation, the method of Fourier integrals is applied and the displacement function is given by the Fourier transform[1], so that the differential problem can be solved as an algebraical problem. Some properties of the Fourier integrals are applied on equation (2.8), leading to the final expression of the displacement field as

$$\boldsymbol{u}(\boldsymbol{x}) = \boldsymbol{G}(\boldsymbol{x}) \cdot \boldsymbol{Q} \tag{2.9}$$

or

$$u_i(\boldsymbol{x}) = G_{ij}(\boldsymbol{x}) Q_j \tag{2.10}$$

where $G_{ij}(\boldsymbol{x})$ represents the *Green function for the elasticity theory*, also called *Kelvin-Somigliana* matrix

$$G_{ij}(\boldsymbol{x}) = \frac{1}{8\pi\mu(\lambda + 2\mu)x}\left[(\lambda + 3\mu)\delta_{ij} + (\lambda + \mu)\frac{x_i x_j}{x^2}\right] \tag{2.11}$$

where x is the length of the $\boldsymbol{x}$. Sometimes, the Kelvin-Somigliana matrix can be also written using the shear modulus μ and Poisson's ratio ν as

$$G_{ij}(\boldsymbol{x}) = \frac{1}{16\pi\mu(1 - \nu)x}\left[(3 - 4\nu)\delta_{ij} + \frac{x_i x_j}{x^2}\right]. \tag{2.12}$$

Since the linear theory of elasticity allows for the superpositions of solutions, this solution can be extended to any distribution of volume forces applied to $\mathcal{B}$. Using a convolution integral between the given external force $\boldsymbol{b}$ and the Green function, the displacement field is determined as

$$\boldsymbol{u}(\boldsymbol{x}) = \int_{\mathcal{B}} \boldsymbol{G}(\boldsymbol{x} - \boldsymbol{\zeta}) \cdot \boldsymbol{b}(\boldsymbol{\zeta})\, dV. \tag{2.13}$$

[1] The *Fourier transform* of the displacement function u_i is

$$U_i(\boldsymbol{\xi}) = \int_{\mathbb{R}^3} u_i(\boldsymbol{x}) e^{-i\boldsymbol{\xi}\cdot\boldsymbol{x}} d\boldsymbol{x}.$$

This relation can be inverted using the *inverse Fourier transform*

$$u_i(\boldsymbol{x}) = \frac{1}{(2\pi)^3}\int_{\mathbb{R}^3} U_i(\boldsymbol{\xi}) e^{-i\boldsymbol{\xi}\cdot\boldsymbol{x}} d\boldsymbol{\xi},$$

where the $\boldsymbol{\xi}$ vector represents the three-dimensional variable in the transformed domain. Therefore, equation (2.8) becomes

$$\mu\xi_i\xi_i U_j(\boldsymbol{\xi}) + (\lambda + \mu)\xi_j\xi_i U_i(\boldsymbol{\xi}) = Q_j$$

2.2 Inclusions: the Eshelby solution

Given an infinitely extended, linearly elastic homogeneous and isotropic body occupying domain $\mathcal{B}$, it is assumed that a finite sub-domain $\mathcal{B}_I$ of $\mathcal{B}$, with the same elastic moduli of the body, is subject to an eigenstrain $\boldsymbol{E}^*$. The eigenstrain field is defined only within the sub-domain $\mathcal{B}_I$ and is zero in all the remaining domain $\mathcal{B}_M = \mathcal{B} - \mathcal{B}_I$. Thus, $\mathcal{B}_I$ is called *inclusion* and $\mathcal{B}_M$ is called *matrix*.
It is possible to express the overall strain field of the body as follows

$$\boldsymbol{E} = \begin{cases} \boldsymbol{E}^{el} + \boldsymbol{E}^* & \text{in } \mathcal{B}_I \\ \boldsymbol{E}^{el} & \text{in } \mathcal{B}_M \end{cases} \tag{2.14}$$

where $\boldsymbol{E}$ indicates the overall strain tensor, which is the sum of the elastic strain tensor $\boldsymbol{E}^{el}$ and the nonelastic strain tensor $\boldsymbol{E}^*$. The constitutive equation takes the form

$$\boldsymbol{T} = \boldsymbol{L} : (\boldsymbol{E} - \boldsymbol{E}^*) \tag{2.15}$$

that is valid in all $\mathcal{B}$, because $\boldsymbol{E}^* = \boldsymbol{0}$ outside the inclusion. Thus, the constitutive relation (2.15) implies that $\boldsymbol{E}^*$ exists and is independent of the application of stresses[2].
Assume the eigenstrain is given and known in all $\mathcal{B}$ (and that it can also be zero somewhere) and no external body forces are applied, so that it is possible to study the only effects of the eigenstrain field. Rewriting the equilibrium equation (2.3) we have

$$\boldsymbol{\nabla} \cdot [\boldsymbol{L} : (\boldsymbol{E} - \boldsymbol{E}^*)] = \boldsymbol{0} \tag{2.16}$$

and, since the elastic tensor $\boldsymbol{L}$ is symmetric, we obtain

$$\boldsymbol{\nabla} \cdot (\boldsymbol{L} : \boldsymbol{E}) - \boldsymbol{\nabla} \cdot (\boldsymbol{L} : \boldsymbol{E}^*) = \boldsymbol{0} \tag{2.17}$$

It can be seen that the contribution of the eigenstrain to the equilibrium equation is similar to that of a body force

$$\boldsymbol{b}^*(\boldsymbol{x}) = -\boldsymbol{\nabla} \cdot (\boldsymbol{L} : \boldsymbol{E}^*) \tag{2.18}$$

Thus, it can be stated that the displacement field caused by an eigenstrain field in a free body is equivalent to that caused by a body force $\boldsymbol{b}^*(\boldsymbol{x})$.
Using the Green's function, given in section 2.1.2, the displacement due to the eigenstrain is described by a convolution integral. From equations (2.13) and (2.18), we obtain

$$\begin{aligned} \boldsymbol{u}(\boldsymbol{x}) &= \int_{\mathcal{B}} \boldsymbol{G}(\boldsymbol{x} - \boldsymbol{\zeta}) \cdot \boldsymbol{b}^*(\boldsymbol{x}) d\boldsymbol{\zeta} = \\ &= -\int_{\mathcal{B}} \boldsymbol{G}(\boldsymbol{x} - \boldsymbol{\zeta}) \cdot [\nabla \cdot (\boldsymbol{L} : \boldsymbol{E}^*(\boldsymbol{\zeta}))] d\boldsymbol{\zeta} \end{aligned} \tag{2.19}$$

or

$$u_i(\boldsymbol{x}) = -\int_{\mathcal{B}} G_{ij}(\boldsymbol{x} - \boldsymbol{\zeta}) L_{sjhk} \frac{\partial E^*_{hk}(\boldsymbol{\zeta})}{\partial \zeta_s} \, d\boldsymbol{\zeta}. \tag{2.20}$$

Applying the Gauss theorem, equation (2.19) becomes

$$\boldsymbol{u}(\boldsymbol{x}) = -\left[\boldsymbol{G}(\boldsymbol{x} - \boldsymbol{\zeta}) \cdot (\boldsymbol{L} : \boldsymbol{E}^*(\boldsymbol{\zeta}))\right]_{\partial \mathcal{B}} + \int_{\mathcal{B}} \boldsymbol{L} : \boldsymbol{E}^*(\boldsymbol{\zeta}) \cdot [\nabla \cdot (\boldsymbol{G}(\boldsymbol{x} - \boldsymbol{\zeta}))] d\boldsymbol{\zeta} \tag{2.21}$$

[2] An example of this case is when in a part of a domain $\mathcal{B}$ there is a thermal expansion, thus the eigenstrain tensor is given by $\boldsymbol{E}^* = \alpha \Delta\vartheta \boldsymbol{I}$, where α is the thermal expansion coefficient and $\Delta\vartheta$ is the variation of temperature. $\boldsymbol{E}^*$ exists and is independent of the application of stresses.

where the first term is zero[3], since the Green function goes to zero at infinity. Thus, using the tensorial indicial notation, equation (2.21) can be rewritten as

$$\begin{aligned} u_i(\boldsymbol{x}) &= \int_{\mathcal{B}} L_{sjhk} E^*_{hk} \frac{\partial G_{ij}(\boldsymbol{x}-\boldsymbol{\zeta})}{\partial \zeta_s}\, d\boldsymbol{\zeta} = \\ &= -\int_{\mathcal{B}} L_{sjhk} E^*_{hk} \frac{\partial G_{ij}(\boldsymbol{x}-\boldsymbol{\zeta})}{\partial x_s}\, d\boldsymbol{\zeta}. \end{aligned} \tag{2.22}$$

When the eigenstrain field E^*_{hk} is different from zero and uniform (constant) in a finite sub-domain $\mathcal{B}_I$ of the space $\mathcal{B}$, the displacement field will be only a function of the geometry of the sub-domain, independent of the eigenstrain applied inside $\mathcal{B}_I$. If these conditions are valid, $\mathcal{B}_I$ is defined as a *homogeneous inclusion* and the displacement field $u_i(\boldsymbol{x})$ in the inclusion is given by

$$u_i(\boldsymbol{x}) = -L_{sjhk} E^*_{hk} \int_{\mathcal{B}_I} \frac{\partial G_{ij}(\boldsymbol{x}-\boldsymbol{\zeta})}{\partial x_s}\, d\boldsymbol{\zeta} \tag{2.23}$$

where E^*_{hk} is assumed to be constant in $\mathcal{B}_I$, while $\boldsymbol{\zeta}$ can vary only within $\mathcal{B}_I$ and $\boldsymbol{x}$ can assume all the values in $\mathbb{R}^3$. Once the shape of the homogenous inclusion is given and the Green function is found, the convolution integral can be solved and the effects of the inclusion can be evaluated in all $\mathcal{B}$ using the fundamental equations of elasticity to find the strain and the stress fields.

2.2.1 The general solution for an ellipsoidal inclusion

An ellipsoidal inclusion $\mathcal{B}_I$ is considered in an isotropic infinite body $\mathcal{B}$. Eigenstrains are given in the ellipsoidal domain and assumed to be uniform (constants). A general solution for the problem has been given by Eshelby, where the ellipsoidal shape chosen for the domain of the inclusion allows to have an exact solution.
First, the convolution integral for the displacement field is introduced as already given in equation (2.23),

$$u_i(\boldsymbol{x}) = -L_{sjkh} E^*_{kh} \int_{\mathcal{B}_I} \frac{\partial G_{ij}(\boldsymbol{x}-\boldsymbol{\zeta})}{\partial x_s}\, d\boldsymbol{\zeta} \tag{2.24}$$

where the domain $\mathcal{B}_I$ is given by

$$\mathcal{B}_I = \left\{ \boldsymbol{x} \in \mathbb{R}^3 : \frac{x_1^2}{a_1^2} + \frac{x_2^2}{a_2^2} + \frac{x_3^2}{a_3^2} \leqslant 1 \right\} \tag{2.25}$$

and the Green function $G_{ij}(\boldsymbol{x}-\boldsymbol{\zeta})$ is, from equation (2.12), equal to

$$G_{ij}(\boldsymbol{x}-\boldsymbol{\zeta}) = \frac{1}{16\pi\mu(1-\nu)\mid \boldsymbol{x}-\boldsymbol{\zeta} \mid} \left[(3-4\nu)\delta_{ij} + \frac{(x_i-\zeta_i)(x_j-\zeta_j)}{\mid \boldsymbol{x}-\boldsymbol{\zeta} \mid^2} \right] \tag{2.26}$$

By substituting the Green function (2.26) and the expression of the elastic isotropic tensor L_{sjkh}, here reported in tensorial indicial notation,

$$L_{sjkh} = \lambda \delta_{sj}\delta_{kh} + \mu(\delta_{sk}\delta_{jh} + \delta_{sh}\delta_{jk}) \tag{2.27}$$

[3]In this case, the Gauss theorem may be interpreted as an integration by parts, since the domain is infinitely extended and the first term of the equation $([\boldsymbol{G}(\boldsymbol{x}-\boldsymbol{\zeta}) \cdot (\boldsymbol{L} : \boldsymbol{E}^*(\boldsymbol{\zeta}))]_{\mathcal{B}})$ goes rapidly to zero at infinity.

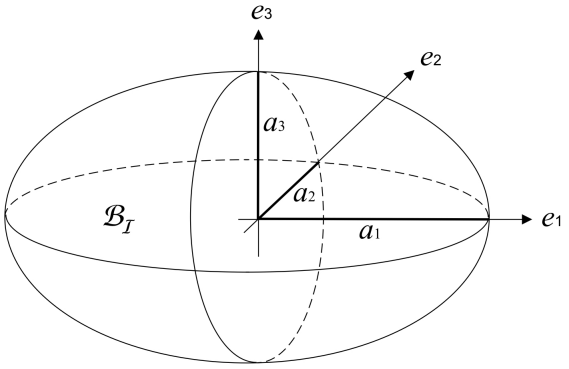

Figure 2.2: An ellipsoidal inclusion with principal half axes a_1, a_2 and a_3

into equation (2.24) the expression for the displacement field is finally obtained as

$$\begin{aligned} u_i(\boldsymbol{x}) = &- E^*_{kh} \int_{\mathcal{B}_I} \left[\frac{\delta_{ih}}{4\pi} \frac{\partial}{\partial x_k} \frac{1}{|\boldsymbol{x}-\boldsymbol{\zeta}|} + \frac{\delta_{ik}}{4\pi} \frac{\partial}{\partial x_h} \frac{1}{|\boldsymbol{x}-\boldsymbol{\zeta}|} \right] d\boldsymbol{\zeta} - \\ &- E^*_{kh} \int_{\mathcal{B}_I} \left[\frac{\nu}{(1-\nu)} \frac{\delta_{kh}}{4\pi} \frac{\partial}{\partial x_i} \frac{1}{|\boldsymbol{x}-\boldsymbol{\zeta}|} - \frac{1}{8\pi(1-\nu)} \frac{\partial^3 |\boldsymbol{x}-\boldsymbol{\zeta}|}{\partial x_i \partial x_k \partial x_h} \right] d\boldsymbol{\zeta}. \end{aligned} \tag{2.28}$$

It is important to introduce the two functions $\Phi(\boldsymbol{x})$ and $\Psi(\boldsymbol{x})$, that are the *harmonic* and *biharmonic potentials* defined on $\mathcal{B}_I$

$$\Phi(\boldsymbol{x}) = \int_{\mathcal{B}_I} \frac{1}{|\boldsymbol{x}-\boldsymbol{\zeta}|}\, d\boldsymbol{\zeta}, \tag{2.29}$$

$$\Psi(\boldsymbol{x}) = \int_{\mathcal{B}_I} |\boldsymbol{x}-\boldsymbol{\zeta}|\, d\boldsymbol{\zeta}. \tag{2.30}$$

These two potentials are solutions of particular partial differential equations[4] and provide an exact solution for the displacement field when $\mathcal{B}_I$ is an ellipsoidal domain. In fact, it is pointed out that $\Phi(\boldsymbol{x})$ and $\Psi(\boldsymbol{x})$ depend only of the geometry of the inclusion and, while $\boldsymbol{x}$ spans the whole space, vector $\boldsymbol{\zeta}$ represents the integration variable and is defined only in the inclusion sub-domain.
So, rewriting (2.28) as

$$u_i(\boldsymbol{x}) = E^*_{kh} \left[\frac{1}{8\pi(1-\nu)} \Psi_{,ikh} - \frac{\delta_{ih}}{4\pi} \Phi_{,k} - \frac{\delta_{ik}}{4\pi} \Phi_{,h} - \frac{\nu\, \delta_{kh}}{4\pi(1-\nu)} \Phi_{,i} \right] \tag{2.31}$$

we find the expression for the displacement vector that is valid for all points $\boldsymbol{x}$ inside and outside the inclusion.

[4]It is important to specify that the Green function for the Poisson equation $\boldsymbol{\nabla}^2\Phi(\boldsymbol{x}) = -4\pi\delta(\boldsymbol{x})$ is given by $\Phi(\boldsymbol{x}) = \frac{1}{|\boldsymbol{x}|}$. Thus, the harmonic potential is the solution of the differential problem

$$\boldsymbol{\nabla}^2\Phi(\boldsymbol{x}) = \begin{cases} -4\pi & \forall\, \boldsymbol{x} \in \mathcal{B}_I \\ 0 & \forall\, \boldsymbol{x} \notin \mathcal{B}_I \end{cases}$$

Moreover, the harmonic and biharmonic potentials have the following property: $\boldsymbol{\nabla}^2\Psi(\boldsymbol{x}) = 2\Phi(\boldsymbol{x})$, which allows to find the differential equation that is solved from the biharmonic potential

$$\boldsymbol{\nabla}^2\boldsymbol{\nabla}^2\Psi(\boldsymbol{x}) = 2\boldsymbol{\nabla}^2\Phi(\boldsymbol{x}) \begin{cases} -8\pi & \forall\, \boldsymbol{x} \in \mathcal{B}_I \\ 0 & \forall\, \boldsymbol{x} \notin \mathcal{B}_I \end{cases}$$

2.2.2 Eshelby's tensor

The strain tensor due to the inclusion can be determined applying the strain-displacement relationship (2.1) to equation (2.31):

$$\begin{aligned} E_{ij}(\boldsymbol{x}) &= E^*_{kh}\left[\frac{1}{8\pi(1-\nu)}\Psi_{,ijkh} - \frac{\nu\,\delta_{kh}}{4\pi(1-\nu)}\Phi_{,ij}\right] - \\ &\quad - \frac{1}{8\pi}E^*_{kh}\left(\delta_{ih}\Phi_{,jk} + \delta_{ik}\Phi_{,jh} + \delta_{jh}\Phi_{,ik} + \delta_{jk}\Phi_{,ih}\right) \end{aligned} \tag{2.32}$$

The definition of the *Eshelby tensor* $\boldsymbol{S}$ which is given by

$$\begin{aligned} S_{ijkh}(\boldsymbol{x}) &= \frac{1}{8\pi(1-\nu)}\Psi_{,ijkh} - \frac{\nu\,\delta_{kh}}{4\pi(1-\nu)}\Phi_{,ij} - \\ &\quad - \frac{1}{8\pi}\left(\delta_{ih}\Phi_{,jk} + \delta_{ik}\Phi_{,jh} + \delta_{jh}\Phi_{,ik} + \delta_{jk}\Phi_{,ih}\right). \end{aligned} \tag{2.33}$$

This allows to express equation (2.32) as

$$E_{ij}(\boldsymbol{x}) = S_{ijkh}(\boldsymbol{x})E^*_{kh} \tag{2.34}$$

or

$$\boldsymbol{E}(\boldsymbol{x}) = \boldsymbol{S}(\boldsymbol{x}) : \boldsymbol{E}^* \tag{2.35}$$

that is valid both inside and outside the inclusion.
The homogeneous inclusion problem with a uniform eigenstrain field can be solved when the harmonic and biharmonic potentials are determined, so that the convolution integral, which represents the displacement field, can be computed. In particular, equation (2.31) can have an analytical and exact solution when the inclusion is an ellipsoidal domain. Under these conditions, Eshelby's most valuable result is that *the strain and stress fields become uniform for the interior points.* This means that the Eshelby tensor is constant, and thus independent of $\boldsymbol{x}$, inside the inclusion. Consequently, we can write

$$\boldsymbol{S}(\boldsymbol{x}) = \begin{cases} \boldsymbol{S}^* & \forall\,\boldsymbol{x} \in \mathcal{B}_I \\ \boldsymbol{S}^\infty(\boldsymbol{x}) & \forall\,\boldsymbol{x} \notin \mathcal{B}_I \end{cases} \tag{2.36}$$

where the interior Eshelby tensor has been indicated with $\boldsymbol{S}^*(\boldsymbol{x})$ and exterior Eshelby tensor has been indicated with $\boldsymbol{S}^\infty(\boldsymbol{x})$.

Eshelby tensor for interior points

Given an ellipsoidal domain $\mathcal{B}_I$, the harmonic potential can be written in terms of the following elliptic integrals:

$$\Phi(\boldsymbol{x}) = \pi a_1 a_2 a_3 \int_0^{+\infty} \frac{1 - f(\boldsymbol{x}, s)}{R(s)}\,ds \qquad \forall\,\boldsymbol{x} \in \mathcal{B}_I \tag{2.37}$$

and

$$\Phi(\boldsymbol{x}) = \pi a_1 a_2 a_3 \int_\eta^{+\infty} \frac{1 - f(\boldsymbol{x}, s)}{R(s)}\,ds \qquad \forall\,\boldsymbol{x} \notin \mathcal{B}_I \tag{2.38}$$

where the functions $f(\boldsymbol{x}, s)$ and $R(s)$ are

$$f(\boldsymbol{x}, s) = \frac{x_1^2}{a_1^2 + s} + \frac{x_2^2}{a_2^2 + s} + \frac{x_3^2}{a_3^2 + s} \tag{2.39a}$$

$$R(s) = \sqrt{(a_1^2 + s) + (a_2^2 + s) + (a_3^2 + s)} \tag{2.39b}$$

and s can assume any real, non negative value. Then, the function η is defined as the largest positive root of $\frac{x_1^2}{a_1^2+\eta} + \frac{x_2^2}{a_2^2+\eta} + \frac{x_3^2}{a_3^2+\eta} = 1$ for exterior points $\boldsymbol{x}$, and zero ($\eta = 0$) for interior points of $\mathcal{B}_I$.
The same can be said for the biharmonic potential that can be written using the following elliptic integrals:

$$\Psi(\boldsymbol{x}),i = \pi a_1 a_2 a_3 x_i \int_0^{+\infty} \frac{1 - f(\boldsymbol{x}, s)}{R(s)} \frac{s}{(a_i^2 + s)}\, ds \qquad \forall\, \boldsymbol{x} \in \mathcal{B}_I \tag{2.40}$$

and

$$\Psi(\boldsymbol{x}),i = \pi a_1 a_2 a_3 x_i \int_\eta^{+\infty} \frac{1 - f(\boldsymbol{x}, s)}{R(s)} \frac{s}{(a_i^2 + s)}\, ds \qquad \forall\, \boldsymbol{x} \notin \mathcal{B}_I \tag{2.41}$$

Once the potentials are given in explicit form, we can compute their derivatives and obtain an expression for the Eshelby tensor (2.33) in the interior domain

$$\begin{aligned} S^*_{ijkh} = &- \frac{a_1 a_2 a_3}{4(1-\nu)} \int_0^{+\infty} \left[\frac{\delta_{ij}\delta_{kh}}{a_k^2 + s} + \frac{\delta_{ik}\delta_{jh}}{a_h^2 + s} + \frac{\delta_{ih}\delta_{jk}}{a_j^2 + s} \right] \frac{s\, ds}{(a_i^2 + s)R(s)} \\ &+ a_1 a_2 a_3 \frac{\nu}{(1-\nu)} \frac{\delta_{kh}\delta_{ij}}{2} \int_0^{+\infty} \frac{ds}{(a_i^2 + s)R(s)} \\ &+ \frac{a_1 a_2 a_3}{4} \delta_{ih}\delta_{jk} \left[\int_0^{+\infty} \frac{ds}{(a_k^2 + s)R(s)} + \int_0^{+\infty} \frac{ds}{(a_h^2 + s)R(s)} \right] \\ &+ \frac{a_1 a_2 a_3}{4} \delta_{jh}\delta_{ik} \left[\int_0^{+\infty} \frac{ds}{(a_i^2 + s)R(s)} + \int_0^{+\infty} \frac{ds}{(a_j^2 + s)R(s)} \right]. \end{aligned} \tag{2.42}$$

This expression shows that the Eshelby tensor is independent of $\boldsymbol{x}$ since the integrals are not function of $\boldsymbol{x}$.
Equation (2.42) leads to one of the main results of the Eshelby theory, also previous mentioned and now demonstrated: *the Eshelby tensor $\boldsymbol{S}^*$ for interior points of an ellipsoidal homogeneous inclusion is constant inside the inclusion; therefore, even the generated strain tensor $\boldsymbol{E}$ is constant in the inclusion.*
Using the Voigt notation, the Eshelby tensor becomes

$$\mathbf{S}^* = \begin{bmatrix} S^*_{1111} & S^*_{1122} & S^*_{1133} & 0 & 0 & 0 \\ S^*_{2211} & S^*_{2222} & S^*_{2233} & 0 & 0 & 0 \\ S^*_{3311} & S^*_{3322} & S^*_{3333} & 0 & 0 & 0 \\ 0 & 0 & 0 & S^*_{1212} & 0 & 0 \\ 0 & 0 & 0 & 0 & S^*_{2323} & 0 \\ 0 & 0 & 0 & 0 & 0 & S^*_{1313} \end{bmatrix} \tag{2.43}$$

where $S^*_{ijkh} = S^*_{jikh} = S^*_{jihk}$ and $tr(\mathbf{S}^*) = 3$; and the eigenstrain $\mathbf{E}^*$ in Voigt notation is given by $\mathbf{E}^* = \{E^*_{11}, E^*_{22}, E^*_{33}, 2E^*_{12}, 2E^*_{23}, 2E^*_{13}\}^\top$.

Explicit expression of the Eshelby tensor for special shapes of inclusions

Considering the Eshelby tensor expressed by (2.42), we can compute its nontrivial components by evaluating the integrals that appear in the formula

$$\begin{aligned}
S^*_{1111} =& \frac{3}{8\pi(1-\nu)} a_1^2 I_{11} + \frac{1-2\nu}{8\pi(1-\nu)} I_1, \\
S^*_{1122} =& \frac{1}{8\pi(1-\nu)} a_2^2 I_{12} - \frac{1-2\nu}{8\pi(1-\nu)} I_1, \\
S^*_{1133} =& \frac{1}{8\pi(1-\nu)} a_3^2 I_{13} - \frac{1-2\nu}{8\pi(1-\nu)} I_1, \\
S^*_{1212} =& \frac{a_1^2+a_2^2}{16\pi(1-\nu)} I_{12} + \frac{1-2\nu}{16\pi(1-\nu)} (I_1 + I_2),
\end{aligned} \tag{2.44}$$

where

$$\begin{aligned}
I_1 =& 2\pi a_1 a_2 a_3 \int_0^{+\infty} \frac{1}{(a_1^2+s)R(s)}\, ds, \\
I_{11} =& 2\pi a_1 a_2 a_3 \int_0^{+\infty} \frac{1}{(a_1^2+s)^2 R(s)}\, ds, \\
I_{12} =& 2\pi a_1 a_2 a_3 \int_0^{+\infty} \frac{1}{(a_1^2+s)(a_2^2+s)R(s)}\, ds.
\end{aligned} \tag{2.45}$$

All the remaining nontrivial components can be obtained by the cyclic permutation of the indices (1, 2, 3). The components that cannot be obtained by the cyclic permutation are zero (for instance $S^*_{1112} = S^*_{1223} = S^*_{1232} = 0$).
Assuming $a_1 > a_2 > a_3$, the I-integrals in (2.45) are expressed by standard elliptic integrals[5]
One of the cases we are most interested is that of a ***cylindrical inclusion*** with $a_1 \to \infty$ and $a_3/a_2 = 1$. Therefore, applying the procedure described and using the formulas found, the interior-point Eshelby tensor, in Voigt notation, is given by

$$\mathbf{S}^* = \begin{bmatrix}
0 & 0 & 0 & 0 & 0 & 0 \\
\frac{\nu}{2(1-\nu)} & \frac{5-4\nu}{8(1-\nu)} & \frac{4\nu-1}{8(1-\nu)} & 0 & 0 & 0 \\
\frac{\nu}{2(1-\nu)} & \frac{4\nu-1}{8(1-\nu)} & \frac{5-4\nu}{8(1-\nu)} & 0 & 0 & 0 \\
0 & 0 & 0 & \frac{3-4\nu}{8(1-\nu)} & 0 & 0 \\
0 & 0 & 0 & 0 & \frac{1}{4} & 0 \\
0 & 0 & 0 & 0 & 0 & \frac{1}{4}
\end{bmatrix}. \tag{2.46}$$

[5]The I-integrals (2.45) can be expressed as elliptic integrals by introducing the aspect ratios $e = \frac{a_3}{a_2}$, $g = \frac{a_2}{a_1}$, with e and $g \in (0,1)$, and the elliptic incomplete integrals of first and second species $P(v,q)$ and $Q(v,q)$ that are given by

$$P(v,q) = \int_0^v \frac{dw}{\sqrt{1-q^2\sin^2(w)}}, \qquad Q(v,q) = \int_0^v \sqrt{1-q^2\sin^2(w)}\, dw$$

where v and q are functions of the aspect ratios and w is an integration variable.

Eshelby tensor for exterior points

The expression of the Eshelby tensor for exterior points can be determined using a slightly different approach. According to equation (2.33), $\boldsymbol{S}$ is given by

$$\begin{aligned} S_{ijkh}(\boldsymbol{x}) &= \frac{1}{8\pi(1-\nu)}\Psi_{,ijkh} - \frac{\nu\,\delta_{kh}}{4\pi(1-\nu)}\Phi_{,ij} - \\ &\quad - \frac{1}{8\pi}\left(\delta_{ih}\Phi_{,jk} + \delta_{ik}\Phi_{,jh} + \delta_{jh}\Phi_{,ik} + \delta_{jk}\Phi_{,ih}\right) \end{aligned} \tag{2.47}$$

where the harmonic and biharmonic potentials for exterior points have been expressed by equations (2.38) and (2.41). Hence, the two potentials, Φ and Ψ, are rewritten by using the I-integrals

$$\begin{aligned} I(\eta) =& 2\pi a_1 a_2 a_3 \int_\eta^{+\infty} \frac{1}{R(s)}\,ds, \\ I_i(\eta) =& 2\pi a_1 a_2 a_3 \int_\eta^{+\infty} \frac{1}{(a_i^2+s)R(s)}\,ds, \\ I_{ij}(\eta) =& 2\pi a_1 a_2 a_3 \int_\eta^{+\infty} \frac{1}{(a_i^2+s)(a_j^2+s)R(s)}\,ds. \end{aligned} \tag{2.48}$$

which have been introduced in equations (2.45) for interior points, and are now considered for exterior points. The function $R(s)$ has been defined from (2.39b) and s can assume any real, non negative value. Furthermore, the function η is taken positive and uniquely determined as the largest positive root of $\frac{x_1^2}{a_1^2+\eta} + \frac{x_2^2}{a_2^2+\eta} + \frac{x_3^2}{a_3^2+\eta} = 1$ for exterior points $\boldsymbol{x}$, and it is zero ($\eta = 0$) for interior points of the inclusion $\mathcal{B}_I$. Consequently, the result for the two potentials is

$$\begin{aligned} \Phi =& \frac{1}{2}\left[I(\eta) - x_l x_l I_L(\eta)\right] \\ \Psi_{,i} =& \frac{1}{2}x_i\left\{I(\eta) - x_l x_l I_L(\eta) - a_I^2[I_I(\eta) - x_l x_l I_{IL}(\eta)]\right\} \end{aligned} \tag{2.49}$$

where the summation convention of Mura[6] has been adopted [64]. By substituting expressions (2.49) in equation (2.47), the exterior-point Eshelby tensor is obtained

$$\begin{aligned} S^{\infty}_{ijkh}(\boldsymbol{x}) =& \frac{1}{8\pi(1-\nu)}\left\{8\pi(1-\nu)S_{ijkh}(\eta) + 2\nu\delta_{kh}x_i I_{I,j}(\eta) + \right. \\ &+ (1-\nu)\left[\delta_{ih}x_k I_{K,j} + \delta_{ih}x_k I_{K,i} + \delta_{ik}x_h I_{H,j} + \delta_{ik}x_h I_{H,i}\right] - \\ &- \delta_{ih}x_k[I_K(\eta) - a_I^2 I_{KI}(\eta)]_{,h} - (\delta_{ik}x_j + \delta_{jk}x_i)\left[I_J(\eta) - \right. \\ &- \left. a_I^2 I_{IJ}(\eta)\right]_{,h} - (\delta_{ih}x_j + \delta_{jh}x_i)\left[I_J(\eta) - a_I^2 I_{IJ}(\eta)\right]_{,k} - \\ &- \left. x_i x_j[I_J(\eta) - a_I^2 I_{IJ}(\eta)]_{,lk}\right\}, \end{aligned} \tag{2.50}$$

with

$$\begin{aligned} S_{ijkh}(\eta) =& \frac{1}{8\pi(1-\nu)}\left\{\delta_{ij}\delta_{kh}\left[2\nu I_I(\eta) - I_K(\eta) + a_I^2 I_{KI}(\eta)\right] + (\delta_{ik}\delta_{jh} + \right. \\ &\left. + \delta_{ih}\delta_{jk})\left[a_I^2 I_{IJ}(\eta) - I_J(\eta) + (1-\nu)[I_K(\eta) + I_H(\eta)]\right]\right\}. \end{aligned} \tag{2.51}$$

[6] According to the summation convention used from Mura, the repeated lower case indices are summed up from 1 to 3, like in the Einstein notation; instead upper case indices take on the same numbers of the corresponding lower case ones, but are not summed. In example,

$$\frac{x_i x_i}{(a_I^2+\eta)} = \frac{x_1^2}{a_1^2+\eta} + \frac{x_2^2}{a_2^2+\eta} + \frac{x_3^2}{a_3^2+\eta}.$$

To obtain the closed-form Eshelby tensor, by following the study by Kim and Lee [48], the I-integrals and their derivatives are given in terms of an outward unit normal vector $\hat{\boldsymbol{n}}$

$$\hat{n}_i = \frac{\frac{x_i}{a_I^2+\eta}}{\sqrt{\frac{x_j x_j}{(a_J^2+\eta)^2}}} \tag{2.52}$$

The introduction of the outward unit normal vector is due to Ju and Sun [42] and allows also to assign a geometric and physical meaning to the above mentioned derivatives, which can be better understood if we consider an imaginary ellipsoid based on a real inclusion constructed, for any point x of the matrix phase, as (see Fig. fig1-8)

$$\frac{x_i x_i}{a_I^2+\eta} = 1 \tag{2.53}$$

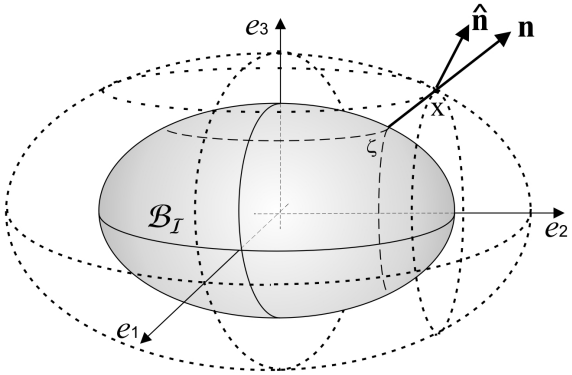

Figure 2.3: Representation of an imaginary ellipsoid passing through a point x of the matrix and its outward unit normal vector $\hat{\boldsymbol{n}}$.

Thus, the derivative of η is

$$\eta_{,i} = \frac{2}{\sqrt{\frac{x_j x_j}{(a_J^2+\eta)^2}}}\hat{n}_i \tag{2.54}$$

and all the derivatives of the I-integrals that appear in (2.50) can be found as functions of $\hat{\boldsymbol{n}}$. With the help of these definitions and after lengthy derivations and computations the exterior-point Eshelby tensor can be finally expressed in terms of $\hat{\boldsymbol{n}}$. This formulation of $\boldsymbol{S}^{\infty}$ is more explicit and compact in comparison of that of Mura [64] and can be easily reduced to the Eshelby tensor for special shapes of the inclusion.
Indeed, in the special case of a cylindrical inclusion, as treated above for the interior-point Eshelby tensor, if $a_1 \to \infty$ and the ratio $\alpha = a_3/a_2 = 1$, we have that the exterior-point Eshelby tensor assumes the form

$$S^{\infty}_{ijkh} = \frac{\rho^2}{8(1-\nu)} F_{ijkh}[B_m], \tag{2.55}$$

$$S^{\infty}_{ij11} = \frac{\nu\rho^2}{2(1-\nu)}\left[\delta_{ij} - 2\hat{n}_i\hat{n}_j\right], \quad S^{\infty}_{1i1j} = \frac{\rho^2}{4}\left[\delta_{ij} - 2\hat{n}_i\hat{n}_j\right] \tag{2.56}$$

where the fourth-order tensor $\boldsymbol{F}$ is defined as

$$\begin{aligned} F_{ijkh}\left[B_m\right] =& B_1\hat{n}_i\hat{n}_j\hat{n}_k\hat{n}_h + B_2(\delta_{ik}\hat{n}_j\hat{n}_h + \delta_{ih}\hat{n}_j\hat{n}_k + \delta_{jk}\hat{n}_i\hat{n}_h + \delta_{jh}\hat{n}_i\hat{n}_k) + \\ &+ B_3\delta_{ij}\hat{n}_k\hat{n}_l + B_4\delta_{kh}\hat{n}_i\hat{n}_j + B_5\delta_{ij}\delta_{kh} + B_6(\delta_{ik}\delta_{jh} + \delta_{ih}\delta_{jk}) \end{aligned} \tag{2.57}$$

and the components of the B_m vector are

$$B_m = \begin{bmatrix} 8(4\rho^2 - 3) \\ 4(\nu - \rho^2) \\ 4(1 - \rho^2) \\ 4(\rho^2 - 2\nu - 1) \\ 4\nu - 2 + \rho^2 \\ 2 - 4\nu + \rho^2 \end{bmatrix}. \tag{2.58}$$

2.3 Inhomogeneities

Consider an homogeneous isotropic and infinitely extended domain $\mathcal{B}^\infty$ with elastic tensor $\boldsymbol{L}^\infty$. When the elastic moduli of a sub-domain $\mathcal{B}_C$ differ from those of the remainder $\mathcal{B}_M = \mathcal{B}^\infty - \mathcal{B}_C$, the sub-domain is called *inhomogeneity* and $\mathcal{B}_M$ is called *matrix*.
So, if a uniform stress $\boldsymbol{f}^\infty$ is applied at infinity, it will generate a non uniform stress field in the neighborhood of the inhomogeneity. This stress disturbance due to the presence of the inhomogeneity can be simulated by an eigenstress field caused by an inclusion, when the associated eigenstrain field is chosen properly. This method to solve the problem is called *equivalent inclusion method* and has been introduced, first, from Eshelby.

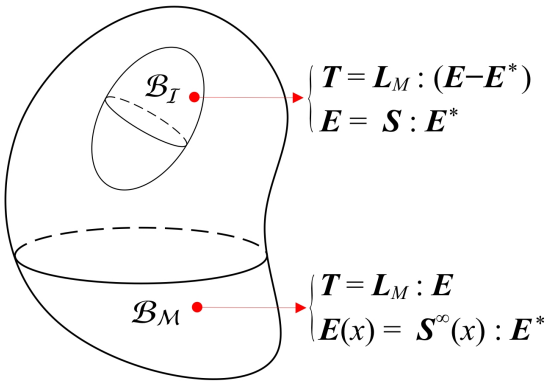

Figure 2.4: A homogeneous ellipsoidal inclusion $\mathcal{B}_I$ in a domain $\mathcal{B}$

2.3.1 The equivalent inclusion method

In order to study the above introduced problem, we consider an ellipsoidal inhomogeneity $\mathcal{B}_C$ (inside the domain $\mathcal{B}^\infty$) which has a different elastic tensor $\boldsymbol{L}_C$ from that of the hosting matrix $\mathcal{B}_M$. The system is in equilibrium without any stress or strain inside the inhomogeneity.
If a uniform stress $\boldsymbol{f}^\infty$ is applied at infinity, it generates a strain $\boldsymbol{E}^\infty$ and a stress $\boldsymbol{T}^\infty$ that are uniform at infinity. Since the regions that are far from the neighborhood of $\mathcal{B}_C$, are

not affected by its presence, $\boldsymbol{E}^{\infty}$ and $\boldsymbol{T}^{\infty}$ can satisfy the relation $\boldsymbol{T}^{\infty} = \boldsymbol{L}_M : \boldsymbol{E}^{\infty}$, where $\boldsymbol{L}_M = \boldsymbol{L}^{\infty}$ is the tensor of the elastic moduli of the matrix.
Thus, in the neighborhood of the inhomogeneity the *equivalent inclusion method* is used to simulate the stress disturbance by the eigenstress resulting from an inclusion which occupies the same space $\mathcal{B}_C$ (having its same geometry and dimensions). The effects of the inhomogeneity are investigated and the problem is addressed by using the superposition method. Two cases are considered.
In the first case, called A, we consider an infinitely extended domain $\mathcal{B}^{\infty}$ with elastic tensor $\boldsymbol{L}^{\infty}$, without any inclusions or inhomogeneities. In this domain, a strain field $\boldsymbol{E}^{\infty}$ and the associated stress field $\boldsymbol{T}^{\infty}$ are given and easily determined.
In the second case, called B, we consider an ellipsoidal inclusion $\mathcal{B}_C$ with the same shape of the inhomogeneity, in an infinitely extended domain $\mathcal{B}^{\infty} = \mathcal{B}_C + \mathcal{B}_M$. The elastic tensor is everywhere equal, $\boldsymbol{L}_C = \boldsymbol{L}_M = \boldsymbol{L}^{\infty}$, and an eigenstrain $\boldsymbol{E}^*$ is given in the inclusion $\mathcal{B}_C$. This problem B is completely defined by Eshelby's theory developed in section 2.2.1, where the unknown is the eigenstrain $\boldsymbol{E}^*$ that must be determined in such a manner that the equivalence between the inhomogeneity problem and the $A + B$ problem holds.
Using the following notation,

$$
\begin{aligned}
\boldsymbol{E}_C &\rightarrow \text{total strain field for interior points (C = carbon nanotube)} \\
\boldsymbol{E}_M &\rightarrow \text{total strain field for exterior points (M = matrix)} \\
\boldsymbol{T}_C &\rightarrow \text{total stress field for interior points} \\
\boldsymbol{T}_M &\rightarrow \text{total stress field for exterior points} \\
\boldsymbol{E}_C^{(A)} &\rightarrow \text{strain field for interior points of problem } A \\
\boldsymbol{E}_M^{(A)} &\rightarrow \text{strain field for exterior points of problem } A \\
\boldsymbol{T}_C^{(A)} &\rightarrow \text{stress field for interior points of problem } A \\
\boldsymbol{T}_M^{(A)} &\rightarrow \text{stress field for exterior points of problem } A \\
\boldsymbol{E}_C^{(B)} &\rightarrow \text{strain field for interior points of problem } B \\
\boldsymbol{E}_M^{(B)} &\rightarrow \text{strain field for exterior points of problem } B \\
\boldsymbol{T}_C^{(B)} &\rightarrow \text{stress field for interior points of problem } B \\
\boldsymbol{T}_M^{(B)} &\rightarrow \text{stress field for exterior points of problem } B
\end{aligned}
$$

for problem A, the strain and stress fields are

$$
\begin{aligned}
\boldsymbol{E}_C^{(A)} &= \boldsymbol{E}^{\infty} \\
\boldsymbol{E}_M^{(A)} &= \boldsymbol{E}^{\infty} \\
\boldsymbol{T}_C^{(A)} &= \boldsymbol{T}^{\infty} \\
\boldsymbol{T}_M^{(A)} &= \boldsymbol{T}^{\infty}
\end{aligned}
\tag{2.59}
$$

According to the ellipsoidal inclusion theory (section 2.2.1), for problem B, the strain fields are given as

$$
\begin{aligned}
\boldsymbol{E}_C^{(B)} &= \boldsymbol{S}^* : \boldsymbol{E}^* \\
\boldsymbol{E}_M^{(B)}(\boldsymbol{x}) &= \boldsymbol{S}^{\infty}(\boldsymbol{x}) : \boldsymbol{E}^*
\end{aligned}
\tag{2.60}
$$

and, the constitutive laws are

$$\begin{aligned} \boldsymbol{T}_C^{(B)} &= \boldsymbol{L}_M : (\boldsymbol{E}_C^{(B)} - \boldsymbol{E}^*) \\ \boldsymbol{T}_M^{(B)}(\boldsymbol{x}) &= \boldsymbol{L}_M : (\boldsymbol{S}^\infty : \boldsymbol{E}^*) \end{aligned} \tag{2.61}$$

Finally, for the inhomogeneity problem, the constitutive equations are given by

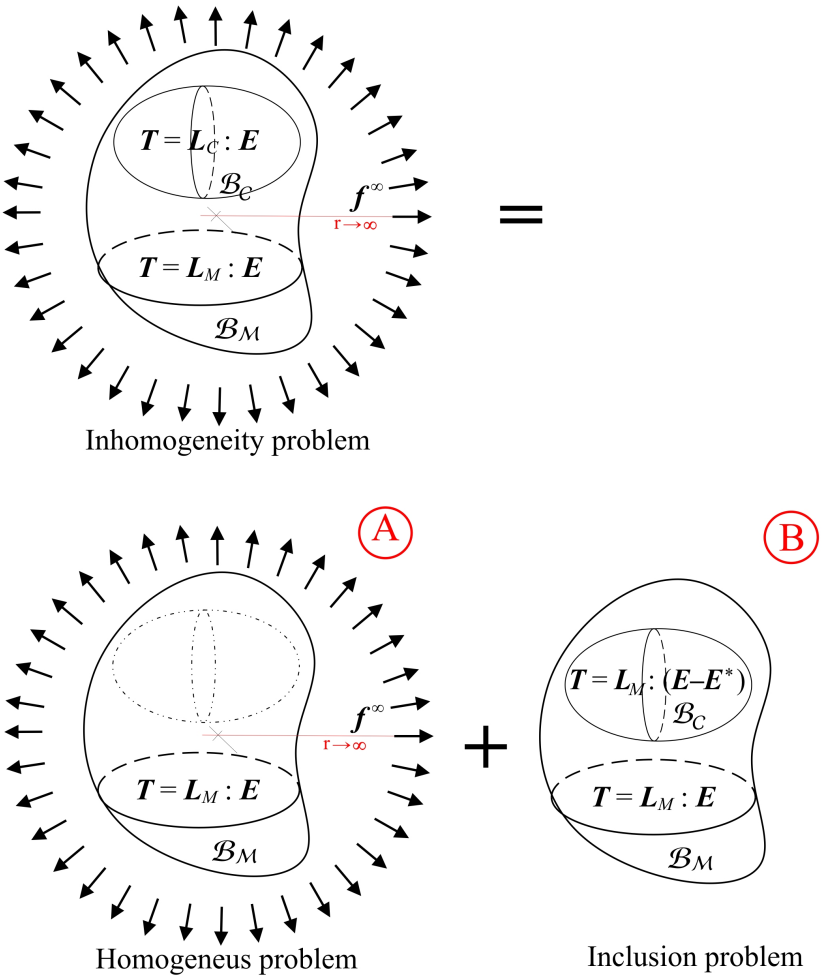

Figure 2.5: Equivalent inclusion method for the inhomogeneity problem

$$\begin{aligned} \boldsymbol{T}_C &= \boldsymbol{L}_C : \boldsymbol{E}_C \quad \text{in} \quad \mathcal{B}_C \\ \boldsymbol{T}_M &= \boldsymbol{L}_M : \boldsymbol{E}_M \quad \text{in} \quad \mathcal{B}_M \end{aligned} \tag{2.62}$$

and the boundary conditions can be set as

$$\begin{aligned} &\boldsymbol{u}_C(\boldsymbol{x}) = \boldsymbol{u}_M(\boldsymbol{x}) && \forall \quad \boldsymbol{x} \in \partial\mathcal{B}_C \\ &\boldsymbol{T}_C(\boldsymbol{x}) \cdot \boldsymbol{n} = \boldsymbol{T}_M(\boldsymbol{x}) \cdot \boldsymbol{n} && \forall \quad \boldsymbol{x} \in \partial\mathcal{B}_C \\ &\boldsymbol{E}_M(\boldsymbol{x}) \to \boldsymbol{E}^\infty && \forall \quad |\boldsymbol{x}| \to \infty \\ &\boldsymbol{T}_M(\boldsymbol{x}) \to \boldsymbol{T}^\infty && \forall \quad |\boldsymbol{x}| \to \infty \end{aligned} \tag{2.63}$$

where $\boldsymbol{u}_C$ and $\boldsymbol{u}_M$ represent the displacement fields inside and outside the inhomogeneity respectively, and $\boldsymbol{n}$ is the outward unit normal to $\partial\mathcal{B}_C$. It is worth to note that the first

boundary condition accounts for a perfectly bonded interface between the inhomogeneity and the matrix, so that continuity of the displacements on the interfacial surface must hold, while the second condition requires that stresses are perfectly transferred at the interface (i.e., interface equilibrium condition).
Thus, the required conditions for the equivalence of strains and stresses in the two stated problems (inhomogeneity problem and $A + B$ superposition problem) are, from (2.59) and (2.60),

$$\boldsymbol{E}_C = \boldsymbol{E}_C^{(A)} + \boldsymbol{E}_C^{(B)} = \boldsymbol{E}^{\infty} + \boldsymbol{S}^* : \boldsymbol{E}^* \tag{2.64}$$

and, from (2.59) and (2.61),

$$\begin{aligned} \boldsymbol{T}_C &= \boldsymbol{T}_C^{(A)} + \boldsymbol{T}_C^{(B)} = \\ &= \boldsymbol{L}_M : \boldsymbol{E}^{\infty} + \boldsymbol{L}_M : (\boldsymbol{E}_C^{(B)} - \boldsymbol{E}^*) = \\ &= \boldsymbol{L}_M : \boldsymbol{E}^{\infty} + \boldsymbol{L}_M : (\boldsymbol{S}^* : \boldsymbol{E}^* - \boldsymbol{E}^*). \end{aligned} \tag{2.65}$$

Since $\boldsymbol{T}_C$ is also given by the constitutive relation for interior points of the inhomogeneity $\boldsymbol{T}_C = \boldsymbol{L}_C : \boldsymbol{E}_C$ from equation (2.62), we have

$$\boldsymbol{L}_C : \boldsymbol{E}_C = \boldsymbol{L}_M : \boldsymbol{E}^{\infty} + \boldsymbol{L}_M : (\boldsymbol{S}^* : \boldsymbol{E}^* - \boldsymbol{E}^*) \tag{2.66}$$

and substituting the expression of $\boldsymbol{E}_C$ (2.64), equation (2.66) can be rewritten as

$$\boldsymbol{L}_C : (\boldsymbol{E}^{\infty} + \boldsymbol{S}^* : \boldsymbol{E}^*) = \boldsymbol{L}_M : \boldsymbol{E}^{\infty} + \boldsymbol{L}_M : (\boldsymbol{S}^* : \boldsymbol{E}^* - \boldsymbol{E}^*), \tag{2.67}$$

from which follows

$$[(\boldsymbol{L}_C - \boldsymbol{L}_M) : \boldsymbol{S}^* + \boldsymbol{L}_M] : \boldsymbol{E}^* = -(\boldsymbol{L}_C - \boldsymbol{L}_M) : \boldsymbol{E}^{\infty}. \tag{2.68}$$

Using matrix notation, the unknown eigenstrain $\boldsymbol{E}^*$ is finally determined

$$\mathbf{E}^* = -\left[(\mathbf{L}_C - \mathbf{L}_M)\mathbf{S}^* + \mathbf{L}_M\right]^{-1} (\mathbf{L}_C - \mathbf{L}_M)\mathbf{E}^{\infty}. \tag{2.69}$$

This result can be expressed in a more compact manner[7] as follows

$$\mathbf{E}^* = \left[(\mathbf{I} - \mathbf{L}_M^{-1}\mathbf{L}_C)^{-1} - \mathbf{S}\right]^{-1} \mathbf{E}^{\infty} \tag{2.70}$$

and the elastic fields for the inhomogeneity $\mathcal{B}_C$ can be, now, obtained substituting (2.70) into equations (2.64) and (2.65)

$$\mathbf{E}_C = \left[\mathbf{I} - \mathbf{S}^*(\mathbf{I} - \mathbf{L}_M^{-1}\mathbf{L}_C)\right]^{-1} \mathbf{E}^{\infty} \tag{2.71a}$$

$$\mathbf{T}_C = \mathbf{L}_C \left[\mathbf{I} - \mathbf{S}^*(\mathbf{I} - \mathbf{L}_M^{-1}\mathbf{L}_C)\right]^{-1} \mathbf{E}^{\infty} \tag{2.71b}$$

[7] Applying the property $(AB)^{-1} = B^{-1}A^{-1}$ to the expression (2.69), we have

$$\begin{aligned} \mathbf{E}^* &= -\left[(\mathbf{L}_C - \mathbf{L}_M)\mathbf{S}^* + \mathbf{L}_M\right]^{-1} \left[(\mathbf{L}_C - \mathbf{L}_M)^{-1}\right]^{-1} \mathbf{E}^{\infty} = \\ &= -\left[(\mathbf{L}_C - \mathbf{L}_M)^{-1}(\mathbf{L}_C - \mathbf{L}_M)\mathbf{S}^* + (\mathbf{L}_C - \mathbf{L}_M)^{-1}\mathbf{L}_M\right]^{-1} \mathbf{E}^{\infty} = \\ &= -\left[\mathbf{S}^* + (\mathbf{L}_C - \mathbf{L}_M)^{-1}\left(\mathbf{L}_M^{-1}\right)^{-1}\right]^{-1} \mathbf{E}^{\infty} = \\ &= \left[(\mathbf{I} - \mathbf{L}_M^{-1}\mathbf{L}_C)^{-1} - \mathbf{S}^*\right]^{-1} \mathbf{E}^{\infty}. \end{aligned}$$

The same can be done for the elastic fields of the matrix, using again the superposition, and writing the equations for the strain $\mathbf{E}_M$ and the stress $\mathbf{T}_M$

$$\boldsymbol{E}_M(\boldsymbol{x}) = \boldsymbol{E}_M^{(A)}(\boldsymbol{x}) + \boldsymbol{E}_M^{(B)}(\boldsymbol{x}) = \boldsymbol{E}^\infty + \boldsymbol{S}^\infty(\boldsymbol{x}) : \boldsymbol{E}^* \tag{2.72a}$$

$$\boldsymbol{T}_M(\boldsymbol{x}) = \boldsymbol{T}_M^{(A)}(\boldsymbol{x}) + \boldsymbol{T}_M^{(B)}(\boldsymbol{x}) = \boldsymbol{L}_M : [\boldsymbol{E}^\infty + \boldsymbol{S}^\infty(\boldsymbol{x}) : \boldsymbol{E}^*] \tag{2.72b}$$

where $\boldsymbol{E}^*$ is always given by equation (2.70).

2.4 The equivalent inclusion method for inhomogeneous inclusions

Suppose we have a linearly elastic body $\mathcal{B}$ subjected to an external surface force system $\boldsymbol{f}$ applied at infinity, and containing an inhomogeneity $\mathcal{B}_C$ which is characterized by its own eigenstrain $\boldsymbol{E}^p$. In this case, the sub-domain $\mathcal{B}_C$ is called *inhomogeneous inclusion* and, to analyze this particular situation, the approach given by Mura is here followed.
Since in the body $\mathcal{B}$ there is the presence of a uniform strain field, $\boldsymbol{E}^\infty$, caused by the external forces $\boldsymbol{f}$, the total strain acting on the body, $\boldsymbol{E}$, can be defined as the sum of two contributions

$$\boldsymbol{E} = \boldsymbol{E}^\infty + \tilde{\boldsymbol{E}} \tag{2.73}$$

which are the uniform strain field generated by the external surface forces and a strain disturbance $\tilde{\boldsymbol{E}}$ caused by the inhomogeneity and its associated eigenstrain.
The constitutive laws for the two phases, which are the inhomogeneous inclusion phase and the hosting matrix phase, can be written as

$$\boldsymbol{T}_M = \boldsymbol{L}_M : \left(\boldsymbol{E}^\infty + \tilde{\boldsymbol{E}}\right) \qquad \text{in } \mathcal{B}_M \tag{2.74a}$$

$$\boldsymbol{T}_C = \boldsymbol{L}_C : \left(\boldsymbol{E}^\infty + \tilde{\boldsymbol{E}} - \boldsymbol{E}^p\right) \qquad \text{in } \mathcal{B}_C. \tag{2.74b}$$

Applying the Eshelby equivalent inclusion method the inhomogeneous inclusion can be simulated by an inclusion with the mentioned eigenstrain $\boldsymbol{E}^p$ plus a fictitious equivalent eigenstrain $\boldsymbol{E}^*$ which accounts for the different elastic moduli of $\mathcal{B}_C$. Rewriting the constitutive equations for each phase, we have

$$\boldsymbol{T}_M = \boldsymbol{L}_M : \left(\boldsymbol{E}^\infty + \tilde{\boldsymbol{E}}\right) \qquad \text{in } \mathcal{B}_M \tag{2.75a}$$

$$\boldsymbol{T}_C = \boldsymbol{L}_M : \left(\boldsymbol{E}^\infty + \tilde{\boldsymbol{E}} - \boldsymbol{E}^p - \boldsymbol{E}^*\right) \qquad \text{in } \mathcal{B}_C. \tag{2.75b}$$

For the equivalence between the inhomogeneous inclusion problem and the inclusion problem the following relation must hold:

$$\boldsymbol{L}_C : \left(\boldsymbol{E}^\infty + \tilde{\boldsymbol{E}} - \boldsymbol{E}^p\right) = \boldsymbol{L}_M : \left(\boldsymbol{E}^\infty + \tilde{\boldsymbol{E}} - \boldsymbol{E}^p - \boldsymbol{E}^*\right) \qquad \text{in } \mathcal{B}_C. \tag{2.76}$$

If, besides $\boldsymbol{E}^\infty$, we assume the eigenstrain $\boldsymbol{E}^p$ is uniform too, then it is possible to exploit the Eshelby solution for inclusions with uniform eigenstrain $(\boldsymbol{E}^p + \boldsymbol{E}^*)$. So, the strain disturbance can be expressed in terms of the Eshelby tensor:

$$\tilde{\boldsymbol{E}} = \boldsymbol{S} : (\boldsymbol{E}^p + \boldsymbol{E}^*) = \boldsymbol{S} : \boldsymbol{E}^{**} \tag{2.77}$$

where, following the treatment of Mura, we indicate the sum of the two uniform eigenstrains with $\boldsymbol{E}^{**}$.

Substituting (2.77) in the relation (2.76), in order to satisfy the equivalence, we have

$$\begin{aligned}
&\boldsymbol{L}_C : \left(\boldsymbol{E}^{\infty} + \boldsymbol{S} : \boldsymbol{E}^{**} - \boldsymbol{E}^{p}\right) = \boldsymbol{L}_M : \left(\boldsymbol{E}^{\infty} + \boldsymbol{S} : \boldsymbol{E}^{**} - \boldsymbol{E}^{**}\right) \Rightarrow \\
\Rightarrow &\left[\boldsymbol{L}_M + (\boldsymbol{L}_C - \boldsymbol{L}_M) : \boldsymbol{S}\right] : \boldsymbol{E}^{**} = (\boldsymbol{L}_M - \boldsymbol{L}_C) : \boldsymbol{E}^{\infty} + \boldsymbol{L}_C : \boldsymbol{E}^{p} \Rightarrow \\
\Rightarrow &\boldsymbol{E}^{**} = \left[\boldsymbol{L}_M + (\boldsymbol{L}_C - \boldsymbol{L}_M) : \boldsymbol{S}\right]^{-1} : \left[\boldsymbol{L}_C : \boldsymbol{E}^{p} - (\boldsymbol{L}_C - \boldsymbol{L}_M) : \boldsymbol{E}^{\infty}\right].
\end{aligned} \tag{2.78}$$

Defining $[\![\boldsymbol{L}]\!]$ as the jump of the elastic tensor between $\mathcal{B}_C$ and $\mathcal{B}_M$

$$[\![\boldsymbol{L}]\!] = \boldsymbol{L}_C - \boldsymbol{L}_M, \tag{2.79}$$

it is possible to derive the stress fields in the the two phases of the body substituting equation (2.77) and the expression of $\boldsymbol{E}^{**}$, (3.12), in (2.75).
Consequently, we obtain the following constitutive law for the hosting matrix:

$$\begin{aligned}
&\boldsymbol{T}_M = \boldsymbol{L}_M : \left(\boldsymbol{E}^{\infty} + \boldsymbol{S} : \boldsymbol{E}^{**}\right) \Rightarrow \\
\Rightarrow &\boldsymbol{T}_M = \boldsymbol{L}_M : \left[\boldsymbol{I} - \boldsymbol{S} : \left[\boldsymbol{L}_M + [\![\boldsymbol{L}]\!] : \boldsymbol{S}\right]^{-1} : [\![\boldsymbol{L}]\!]\right] : \boldsymbol{E}^{\infty} + \\
&+ \boldsymbol{L}_M : \left[\boldsymbol{S} : \left[\boldsymbol{L}_M + [\![\boldsymbol{L}]\!] : \boldsymbol{S}\right]^{-1} : \boldsymbol{L}_C\right] : \boldsymbol{E}^{p}.
\end{aligned} \tag{2.80}$$

and the following expression for the inhomogeneous inclusion:

$$\begin{aligned}
&\boldsymbol{T}_C = \boldsymbol{L}_M : \left[\boldsymbol{E}^{\infty} + (\boldsymbol{S} - \boldsymbol{I}) : \boldsymbol{E}^{**}\right] \Rightarrow \\
\Rightarrow &\boldsymbol{T}_C = \boldsymbol{L}_M : \left[\boldsymbol{I} - (\boldsymbol{S} - \boldsymbol{I}) : \left[\boldsymbol{L}_M + (\boldsymbol{L}_C - \boldsymbol{L}_M) : \boldsymbol{S}\right]^{-1} : [\![\boldsymbol{L}]\!]\right] : \boldsymbol{E}^{\infty} + \\
&+ \boldsymbol{L}_M : \left[(\boldsymbol{S} - \boldsymbol{I}) : \left[\boldsymbol{L}_M + (\boldsymbol{L}_C - \boldsymbol{L}_M) : \boldsymbol{S}\right]^{-1} : \boldsymbol{L}_C\right] : \boldsymbol{E}^{p}.
\end{aligned} \tag{2.81}$$

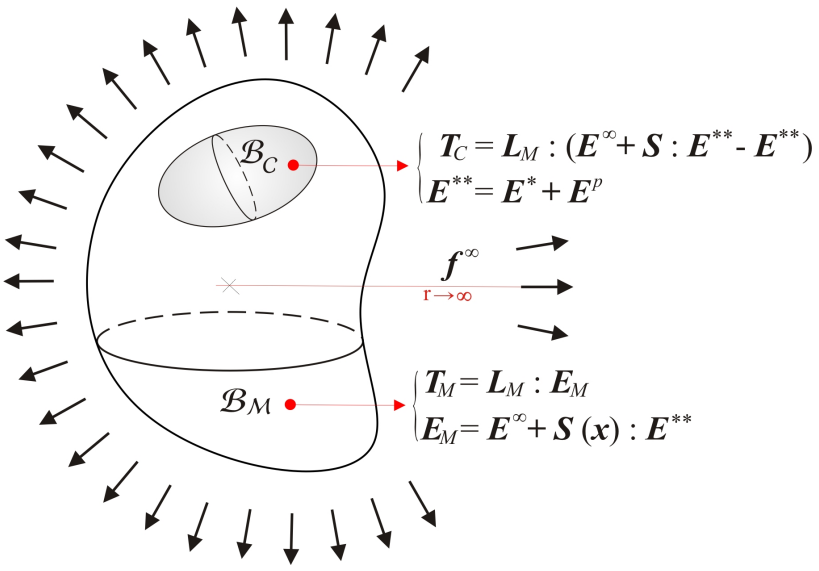

Figure 2.6: Equivalent inclusion method for the inhomogeneous inclusions. Governing equations for the two sub-domains of the body.

2.5 Mori-Tanaka theory: random distribution of inclusions

The Eshelby theory and, in particular, the inclusion problem along with the equivalent inclusion method for the inhomogeneities allow to investigate the effective elastic properties of heterogeneous materials, such as a dispersion of particles in an homogeneous matrix. The Mori-Tanaka theory applies the results of Eshelby theory to estimate macroscopic mechanical properties of aggregates and, thus, it determines the average internal stress in a matrix of a material containing inclusions with a given eigenstrain.

First, some general properties of the internal stresses and strains of inclusions are given. Consider an elastic homogeneous body $\mathcal{B}_0$ with constant elastic moduli. The *average of internal stresses* can be defined as the volume integral on $\mathcal{B}_0$ of the stress $\boldsymbol{T}$

$$\int_{\mathcal{B}_0} T_{ij}\, dV = \int_{\mathcal{B}_0} T_{ik}\delta_{jk}\, dV = \int_{\mathcal{B}_0} T_{ik}x_{j,k}\, dV \tag{2.82}$$

since $\delta_{jk} = x_{j,k}$. Integrating by parts and noting $T_{ik,k} = 0$ in $\mathcal{B}_0$ and $T_{jk}n_k = 0$ on its boundary $\partial\mathcal{B}_0$, the volume integral of internal stresses becomes equal to zero

$$\int_{\mathcal{B}_0} T_{ij}\, dV = \int_{\partial\mathcal{B}_0} T_{ik}x_j n_k\, dS - \int_{\mathcal{B}_0} T_{ik,k}x_j\, dV = 0 \tag{2.83}$$

Now, suppose that a uniform eigenstrain $\boldsymbol{E}^*$ is given to an aggregate $\mathcal{B}_{NC}$ of inclusions in the $\mathcal{B}_0$ domain. The eigenstrain produces an internal stress field $\boldsymbol{T}$ and a strain field $\boldsymbol{E}$. Computing the average of the total strain over the whole body, called *macroscopic strain*, we have

$$\begin{aligned} \langle E_{ij}\rangle_{\mathcal{B}_0} &= \frac{1}{V}\int_{\mathcal{B}_0} E_{ij}\, dV = \frac{1}{V}\int_{\mathcal{B}_0} (E^{el}_{ij} + E^*_{ij})\, dV = \\ &= \frac{1}{V}L^{-1}_{ijkl}\int_{\mathcal{B}_0} T_{kl}\, dV + \frac{1}{V}\int_{\mathcal{B}_0} E^*_{ij}\, dV \end{aligned} \tag{2.84}$$

which, for the result (2.83), gives

$$\langle E_{ij}\rangle_{\mathcal{B}_0} = \frac{1}{V}\int_{\mathcal{B}_0} E^*_{ij}\, dV \tag{2.85}$$

where V is the volume of the body $\mathcal{B}_0$.
Since $\boldsymbol{E}^*$ is given only in the subdomain $\mathcal{B}_{NC}$, we can define the volume fraction of the inclusions as $\phi_C = V_{NC}/V$, and rewrite equation (2.85) as

$$\langle E_{ij}\rangle_{\mathcal{B}_0} = \phi_C E^*_{ij} \tag{2.86}$$

or, indicating $\langle E_{ij}\rangle_{\mathcal{B}_0}$ as $\overline{\boldsymbol{E}}$,

$$\overline{\boldsymbol{E}} = \phi_C \boldsymbol{E}^* \tag{2.87}$$

This result implies that the macroscopic strain is directly related with the uniform eigenstrain $\boldsymbol{E}^*$ and it is valid not only for inclusions, but also for inhomogeneities, applying the equivalent inclusion method.

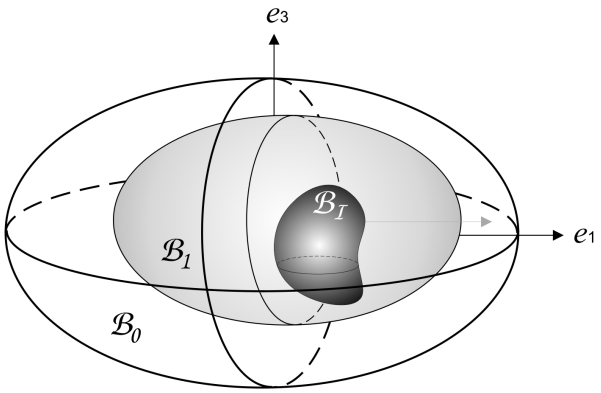

Figure 2.7: Inclusion $\mathcal{B}_I$ with an arbitrary shape in an infinite domain

2.5.1 The Mori-Tanaka theorem

Consider a homogeneous domain containing an inclusion $\mathcal{B}_I$ which has an arbitrary shape. A given uniform eigenstrain $\boldsymbol{E}^*$ produces an interal stress $\boldsymbol{T}^\infty$ that is evaluated assuming the domain to be infinitely extended. We can integrate $\boldsymbol{T}^\infty$ over a domain $\mathcal{B}_0 - \mathcal{B}_1$ as shown in the figure, where $\mathcal{B}_0$ and $\mathcal{B}_1$ are both ellipsoidal and $\mathcal{B}_0 \supset \mathcal{B}_1 \supset \mathcal{B}_I$; thus, from the Eshelby theory, we have

$$\int_{\mathcal{B}_0 - \mathcal{B}_1} \boldsymbol{T}^\infty \, dV = V_I \, \boldsymbol{L} : [\boldsymbol{S}_0 : \boldsymbol{E}^* - \boldsymbol{S}_1 : \boldsymbol{E}^*] \tag{2.88}$$

where V_I is the volume of the inclusion and $\boldsymbol{S}_0$ and $\boldsymbol{S}_1$ are the Eshelby tensors defined in the domains $\mathcal{B}_0$ and $\mathcal{B}_1$ respectively. This equation leads to an interesting conclusion: *the volume integral of $\boldsymbol{T}^\infty$ over a domain $\mathcal{B}_0 - \mathcal{B}_1$ is proportional to the volume V_I of the inclusion and it depends only on the shape of $\mathcal{B}_0$ and $\mathcal{B}_1$. The volume integrals of the stress and strain vanish when $\mathcal{B}_0$ and $\mathcal{B}_1$ have the same shape and orientation*[8], that is, when the half axes of the two ellipsoids are: $a_1/b_1 = a_2/b_2 = a_3/b_3$ (where a_i are half axes of the ellipsoidal domain $\mathcal{B}_0$ and b_i half axes of $\mathcal{B}_1$). If the inclusion has an ellipsoidal shape we have a limit

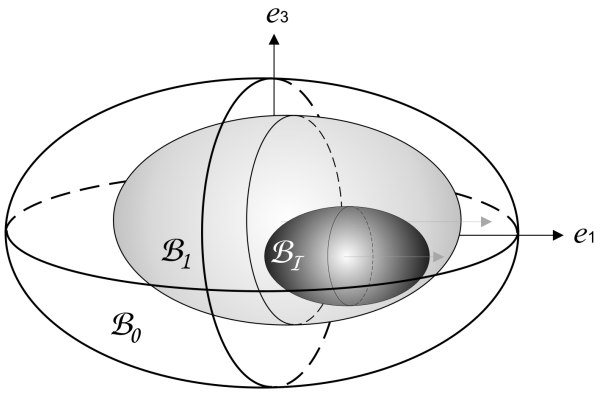

Figure 2.8: Inclusion $\mathcal{B}_I$, domain $\mathcal{B}_0$ and $\mathcal{B}_1$ have the same shape and orientation

[8]This conclusion is valid even when the eigenstrains in $\mathcal{B}_I$ are non-uniform and if $\mathcal{B}_I$ is an inhomogeneity.

case, with $\mathcal{B}_I \to \mathcal{B}_1$; thus

$$\int_{\mathcal{B}_0-\mathcal{B}_I} \boldsymbol{T}^\infty \, dV = V_I \, \boldsymbol{L} : [\boldsymbol{S}_0 : \boldsymbol{E}^* - \boldsymbol{S}^* : \boldsymbol{E}^*] \,, \quad \mathcal{B}_0 \supset \mathcal{B}_I \tag{2.89}$$

where $\boldsymbol{S}^*$ is the Eshelby tensor in the inclusion.
Since $\mathcal{B}_0$ and $\mathcal{B}_I$ have the same shape, the volume integral vanishes

$$\int_{\mathcal{B}_0-\mathcal{B}_I} \boldsymbol{T}^\infty \, dV = 0. \tag{2.90}$$

Similarly, for the corresponding strain

$$\int_{\mathcal{B}_0-\mathcal{B}_I} \boldsymbol{E}^\infty \, dV = 0. \tag{2.91}$$

These properties have been demonstrated by Mori and Tanaka [62].

2.5.2 Image stresses and strains

Consider a finite homogeneous domain $\mathcal{B}_0$ and assume there is an inclusion $\mathcal{B}_I$ inside, with an assigned uniform eigenstrain $\boldsymbol{E}^*$. Then, assume $\mathcal{B}_I$ is similar to $\mathcal{B}_0$, so that properties (2.90) and (2.91) hold. In order to find the internal stress $\boldsymbol{T}$ due to $\mathcal{B}_I$, we make a first approximation, where the internal stress is taken as $\boldsymbol{T}^\infty$ previously defined; so we can write

$$\int_{\mathcal{B}_0} \boldsymbol{T}^\infty \, dV = \int_{\mathcal{B}_I} \boldsymbol{T}^\infty \, dV + \int_{\mathcal{B}_0-\mathcal{B}_I} \boldsymbol{T}^\infty \, dV \tag{2.92}$$

where the second term vanishes because of the property (2.90); thus

$$\int_{\mathcal{B}_0} \boldsymbol{T}^\infty \, dV = \int_{\mathcal{B}_I} \boldsymbol{T}^\infty \, dV \tag{2.93}$$

It is possible to note that equation (2.93) cannot be rewritten, applying integration by parts, like equation (2.83) because $\boldsymbol{T}^\infty$ does not satisfy the traction free condition $\boldsymbol{T}^\infty \cdot \boldsymbol{n} = \boldsymbol{0}$ on $\partial\mathcal{B}_0$. Therefore, we add a correction term $\boldsymbol{T}^{im}$ to $\boldsymbol{T}^\infty$ to obtain the exact solution for the internal stress. This term, $\boldsymbol{T}^{im}$, is called *image stress*, and is chosen so that $\boldsymbol{\nabla} \cdot \left(\boldsymbol{T}^{im}\right)^\top = \boldsymbol{0}$ in $\mathcal{B}_0$, and $\boldsymbol{T}^\infty \cdot \boldsymbol{n} + \boldsymbol{T}^{im} \cdot \boldsymbol{n} = \boldsymbol{0}$ on $\partial\mathcal{B}_0$:

$$\boldsymbol{T} = \boldsymbol{T}^\infty + \boldsymbol{T}^{im} \tag{2.94}$$

The average of $\boldsymbol{T}^{im}$, which is denoted by $\overline{\boldsymbol{T}}^{im}$, is given by

$$\overline{\boldsymbol{T}}^{im} = \langle T_{ij}^{im} \rangle_{\mathcal{B}_0} = \frac{1}{V} \int_{\mathcal{B}_0} T_{ij}^{im} \, dV = -\frac{1}{V} \int_{\mathcal{B}_0} T_{ij}^{\infty} \, dV = -\frac{1}{V} \int_{\mathcal{B}_I} T_{ij}^{\infty} \, dV \tag{2.95}$$

where V is the volume of $\mathcal{B}_0$. Since the eigenstrain is uniform

$$\overline{\boldsymbol{T}}^{im} = -\left(\frac{V_I}{V}\right) \boldsymbol{L} : [\boldsymbol{S}^* : \boldsymbol{E}^* - \boldsymbol{E}^*] \tag{2.96}$$

Finally, we can obtain a similar result for the strain; so defining the strain as

$$\boldsymbol{E} = \boldsymbol{E}^\infty + \boldsymbol{E}^{im} \tag{2.97}$$

where $\boldsymbol{E}^{im}$ indicates the *image strain* due to the presence of the free surface. From equation (2.91), we have

$$\overline{\boldsymbol{E}}^{\infty} = \langle E_{ij}^{\infty} \rangle_{\mathcal{B}_0} = \frac{1}{V} \int_{\mathcal{B}_0} \boldsymbol{E}^{\infty} \, dV = \frac{1}{V} \int_{\mathcal{B}_I} T_{ij}^{\infty} \, dV = \left(\frac{V_I}{V} \right) \boldsymbol{S}^* : \boldsymbol{E}^* \tag{2.98}$$

while the average of $\boldsymbol{E}^{im}$ is

$$\overline{\boldsymbol{E}}^{im} = \langle E_{ij}^{im} \rangle_{\mathcal{B}_0} = - \left(\frac{V_I}{V} \right) [\boldsymbol{S} : \boldsymbol{E}^* - \boldsymbol{E}^*] \tag{2.99}$$

Hence, the macroscopic strain is given by

$$\overline{\boldsymbol{E}} = \overline{\boldsymbol{E}}^{\infty} + \overline{\boldsymbol{E}}^{im} = c_I \boldsymbol{E}^* \tag{2.100}$$

where $c_I = V_I/V$ is the volume fraction of the inclusion. In this way, we get the same result of equation (2.87).
At this point, all fundamental concepts to discuss the Mori-Tanaka theory have been introduced.

2.5.3 Random distribution of inclusions: Mori-Tanaka method

Consider an elastic homogeneous domain $\mathcal{B}_0$ with constant elastic moduli. Suppose the domain has N homogeneous ellipsoidal inclusions, indicated as $\mathcal{B}_{NC}$, that are uniformly distributed in the matrix and have a given uniform eigenstrain $\boldsymbol{E}^*$. First we define the average stresses in the matrix $\mathcal{B}_M = \mathcal{B}_0 - \mathcal{B}_{NC}$ as $\overline{\boldsymbol{T}}_M$ and those in the inclusions as $\overline{\boldsymbol{T}}_{NC}$. From equation (2.83), we have

$$\phi_C \overline{\boldsymbol{T}}_{NC} + (1 - \phi_C) \overline{\boldsymbol{T}}_M = 0 \tag{2.101}$$

where $\phi_C = V_{NC}/V$ is the volume fraction of the inclusions.

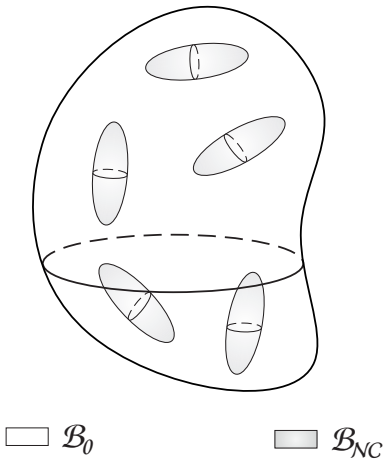

Figure 2.9: A finite domain with randomly distributed ellipsoidal inclusions

Suppose to introduce a new inclusion and that the number of inclusions is so large that this does not influence ϕ_C. Since we have a random distribution of inclusions, the new one is inserted randomly. Therefore, within any inclusion the stress becomes

$$\boldsymbol{T} = \boldsymbol{T}^{\infty} + \overline{\boldsymbol{T}}_M \tag{2.102}$$

where $\boldsymbol{T}^{\infty}$ is the stress due to an inclusion present in an infinite domain

$$\boldsymbol{T}^{\infty} = \boldsymbol{L} : [\boldsymbol{S} : \boldsymbol{E}^{*} - \boldsymbol{E}^{*}] \tag{2.103}$$

and $\overline{\boldsymbol{T}}_M$ is the stress already present in the matrix. Since the inclusion, as said above, can be inserted in any place, the internal stress $\boldsymbol{T}$ must be equal to $\overline{\boldsymbol{T}}_{NC}$. Thus, from (2.102),

$$\overline{\boldsymbol{T}}_{NC} = \boldsymbol{T}^{\infty} + \overline{\boldsymbol{T}}_M \tag{2.104}$$

and substituting equation (2.104) into (2.101), we obtain the following equations

$$\overline{\boldsymbol{T}}_M = -\phi_C \boldsymbol{T}^{\infty} \tag{2.105}$$

$$\overline{\boldsymbol{T}}_{NC} = \boldsymbol{T}^{\infty} - \phi_C \boldsymbol{T}^{\infty} \tag{2.106}$$

It is important to note that the average stress in the matrix is the sum of the average of $\boldsymbol{T}^{\infty}$ and $\boldsymbol{T}^{im}$ caused by all the inclusions: $-\phi_C \boldsymbol{T}^{\infty} = \overline{\boldsymbol{T}}^{\infty} + \overline{\boldsymbol{T}}^{im}$.

The conclusions obtained are extremely useful, because they allow to express the average stress and the elastic strain energy in such simple forms when inclusions are randomly distributed in a homogeneous domain. These results have been found by Mori and Tanaka and the given definitions of the stresses are known as the outcome of the stress average theorem. The results can be also applied when eigenstrains are not uniform and when inclusions are inhomogeneous.

Chapter 3

A Stick-Slip Model for CNT Nanocompostes

3.1 Introduction

Among the major properties exhibited by nanocomposites, their unique ability to absorb vibrations and noise turns out to be one of the most attractive features in view of various applications in diverse fields of engineering such as aerospace, automotive, and civil engineering. The ability to absorb and dissipate mechanical energy, typically referred to as damping capacity, has become a necessary feature for multi-functional composite structures, such as multi-stable morphing composites, and more general dynamic systems.

In order to provide effective predictive tools by which the damping mechanism due to the stick-slip at the CNT/matrix interfaces can be accurately described, a theoretical nonlinear model is here proposed [27]. The proposed model is intentionally constructed to be easily and efficiently implemented in standard finite element computational codes.

The presented model is a meso-scale nonlinear incremental constitutive theory which adopts and reviews the Eshelby and Mori-Tanaka theories basic principles. A combination of the mean-field homogenization method based on the Eshelby equivalent inclusion method [21, 22], and the Mori–Tanaka average stress and strain theorem [12, 62] is adopted together wit the idea of inhomogeneous inclusions with inelastic eigenstrains [64]. Indeed, the novelty idea consists in introducing inelastic eigenstrains in the CNT inclusions to model the shear stick-slip between CNTs and the polymer matrix. The evolution of the plastic eigenstrains is regulated by a constitutive law based on a micromechanical adjustment of the von Mises criterion whereby the effective stress function is the second invariant of the deviatoric part of the stress discontinuity at the CNT-matrix interface. The resulting elastoplastic model can be framed within the unified theory of viscoplasticity of [14], with suitable prescriptive assumptions that ensure the rate independence of the model.

The meso-scale phenomenological model has the virtue of accounting for various micro-scale features such as the nano-fillers geometry, orientation, interface properties, as well as macroscopic features such as the elastic properties and volume fractions of the phases. No explicit nano-scale effects due to the nanofibers are accounted for in the model. This is because the model accounts just at the macroscopic level for the presence of the *inclusions*. Typical nano-size effects such as the weak van der Waals interaction forces between the carbon

atoms and the polymer chains are only indirectly taken into account by averaged values of characteristic parameters, such the ISS as reported in previous studies (see, for example, [20]; [76]). The interfacial energy dissipation mechanism described by the present model is peculiar for CNT composites, and the kind of dissipation taking place at the CNT-matrix interface. This dissipation is due to the weak van der Waals forces linking the CNTs with the polymer chains which can be overcome by relatively low levels of interfacial shear stresses.

A set of fundamental constitutive parameters are identified and their effects on material dissipation are explored through differential evolution-based optimization studies aimed at maximizing the damping capacity of the nanocomposites. The validity of the proposed constitutive theory is confirmed by a reasonable agreement between previous experimental damping measurements for Epoxy and PEEK nanocomposites and the theoretically computed damping.

3.2 Modeling stick-slip mechanism for carbon nanotube composites

The established model for the equivalent continuum macroscopic material response is framed within the Eshelby theory for elastic inclusions combined with the results of the Mori-Tanaka theory for the average stress.

Carbon nanotube/polymer composites are assumed as two-phase materials, where the phase of linearly elastic isotropic hosting matrix occupies the region denoted by $\mathcal{B}_{\mathrm{M}}$, and the phase of inhomogeneous inclusions (here CNTs) occupies the region denoted by $\mathcal{B}_{\mathrm{C}}$. If the volume of the inhomogeneous inclusions is denoted by V_{C} and V represents the volume of the nanocomposite in its natural state $\mathcal{B} = \mathcal{B}_{\mathrm{M}} \cup \mathcal{B}_{\mathrm{C}}$, the volume fractions of the inclusions and the matrix are defined as $\phi_{\mathrm{C}} := V_{\mathrm{C}}/V$ and $\phi_{\mathrm{M}} = 1 - \phi_{\mathrm{C}}$, respectively.

The CNTs embedded in the matrix can be randomly oriented or aligned along a given direction, as chosen in the present formulation (see Fig. 3.1).

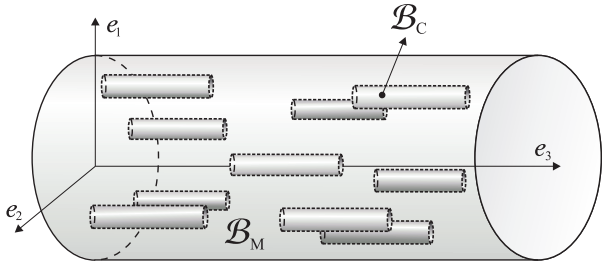

Figure 3.1: Unidirectional nanocomposite material. The CNTs are perfectly aligned along the principal axis of the cylindrical body.

In the Eshelby equivalent inclusion method, the concept of eigenstrain was introduced to solve the stress equilibrium at the interface, thus determining the stress disturbance due to the presence of inhomogeneities (inclusions) in the body. Such stress perturbation can be simulated by an eigenstress field caused by the inclusions, when an associated eigenstrain field is suitably chosen within the continuum possessing the elastic properties of the matrix. Therefore, the eigenstrain is a fictitious strain field defined only inside the subdomain spanned by the inhomogeneities.

In this formulation, the idea of an additional inelastic eigenstrain field [64] is exploited to

incorporate the description of the nonlinear stick-slip phenomenon between CNTs and matrix, phenomenon that gives rise to interfacial CNT-matrix energy dissipation.

3.2.1 Incremental constitutive equations

In consonance with previous works [18, 38, 71], the Mori-Tanaka average stress approach [62, 94] is cast in incremental form to define an equivalent continuum model capable of describing the nano/micro hysteresis associated with the shear slip of the CNTs.

The equivalent incremental strain and stress tensors – denoted by $\dot{\boldsymbol{E}}$ and $\dot{\boldsymbol{T}}$, respectively – are expressed in terms of equivalent continuum average quantities as

$$\dot{\boldsymbol{E}} = \phi_{\mathrm{M}}\dot{\boldsymbol{E}}_{\mathrm{M}} + \phi_{\mathrm{C}}\dot{\boldsymbol{E}}_{\mathrm{C}}, \tag{3.1a}$$

$$\dot{\boldsymbol{T}} = \phi_{\mathrm{M}}\dot{\boldsymbol{T}}_{\mathrm{M}} + \phi_{\mathrm{C}}\dot{\boldsymbol{T}}_{\mathrm{C}} \tag{3.1b}$$

where $(\dot{\boldsymbol{E}}_{\mathrm{M}}, \dot{\boldsymbol{T}}_{\mathrm{M}})$ and $(\dot{\boldsymbol{E}}_{\mathrm{C}}, \dot{\boldsymbol{T}}_{\mathrm{C}})$ are the average strain and stress rates in $\mathcal{B}_{\mathrm{M}}$ and $\mathcal{B}_{\mathrm{C}}$, respectively. Relative slippage between the CNTs and the surrounding matrix induces a kind of interfacial local elastoplastic behavior which is aimed to be described starting from an elastoplastic behavior localized in the CNTs, and consequently averaged out throughout the equivalent composite material according to the Eshelby equivalent inclusion method. This modeling assumption does not exactly reflect the nature of the frictional interfacial behavior but is expected to give rise to the same type of local inelastic behavior.

The incremental constitutive laws are given in the form

$$\dot{\boldsymbol{T}}_{\mathrm{C}} = \boldsymbol{L}_{\mathrm{C}} : (\dot{\boldsymbol{E}}_{\mathrm{C}} - \dot{\boldsymbol{E}}^{\mathrm{P}}) \qquad \text{in } \mathcal{B}_{\mathrm{C}}\,, \tag{3.2a}$$

$$\dot{\boldsymbol{T}}_{\mathrm{M}} = \boldsymbol{L}_{\mathrm{M}} : \dot{\boldsymbol{E}}_{\mathrm{M}} \qquad \text{in } \mathcal{B}_{\mathrm{M}}\,, \tag{3.2b}$$

where $(\boldsymbol{L}_{\mathrm{C}}, \boldsymbol{L}_{\mathrm{M}})$ are the elastic tensors of the inclusion and matrix phases, respectively, while $\dot{\boldsymbol{E}}^{\mathrm{P}}$ is the incremental plastic strain in the CNTs.
The incremental stress $\dot{\boldsymbol{T}}_{\mathrm{C}}$ acting in the inclusions may be expressed in terms of the elastic tensor $\boldsymbol{L}_{\mathrm{M}}$ introducing a fictitious incremental eigenstrain denoted by $\dot{\boldsymbol{E}}^{*}$, according to the Eshelby equivalent inclusion method [21]:

$$\boldsymbol{L}_{\mathrm{C}} : (\dot{\boldsymbol{E}}_{\mathrm{C}} - \dot{\boldsymbol{E}}^{\mathrm{P}}) = \boldsymbol{L}_{\mathrm{M}} : (\dot{\boldsymbol{E}}_{\mathrm{C}} - \dot{\boldsymbol{E}}^{\mathrm{P}} - \dot{\boldsymbol{E}}^{*})\,. \tag{3.3}$$

Thus, an incremental *stress discontinuity* at the interface can be defined as

$$[\![\dot{\boldsymbol{T}}]\!] := [\boldsymbol{L}_{\mathrm{C}} - \boldsymbol{L}_{\mathrm{M}}] : (\dot{\boldsymbol{E}}_{\mathrm{C}} - \dot{\boldsymbol{E}}^{\mathrm{P}}) = -\boldsymbol{L}_{\mathrm{M}} : \dot{\boldsymbol{E}}^{*}\,. \tag{3.4}$$

Such a stress discontinuity turns out to be related to the incremental stress in the inclusions as

$$[\![\dot{\boldsymbol{T}}]\!] = \left(\boldsymbol{I} - \boldsymbol{L}_{\mathrm{M}} : \boldsymbol{L}_{\mathrm{C}}^{-1}\right) : \dot{\boldsymbol{T}}_{\mathrm{C}}\,. \tag{3.5}$$

The major mechanical consequence is that any limit condition, enforced on the interface, can be directly translated into a limit condition on the stress states in the inclusions.

According to the Mori-Tanaka average stress theorem [62], the incremental strain fields of the two phases can be given in terms of the equivalent incremental strain $\dot{\boldsymbol{E}}$ and increments of perturbation strain:

$$\dot{\boldsymbol{E}}_{\mathrm{M}} = \dot{\boldsymbol{E}} + \tilde{\dot{\boldsymbol{E}}}_{\mathrm{M}}\,, \qquad \dot{\boldsymbol{E}}_{\mathrm{C}} = \dot{\boldsymbol{E}}_{\mathrm{M}} + \tilde{\dot{\boldsymbol{E}}}_{\mathrm{C}}\,, \tag{3.6}$$

where $\tilde{\dot{\boldsymbol{E}}}_{\mathrm{M}}$ is the unknown perturbation incremental strain field in $\mathcal{B}_{\mathrm{M}}$ with respect to the uniform equivalent strain field $\dot{\boldsymbol{E}}$ while $\tilde{\dot{\boldsymbol{E}}}_{\mathrm{C}}$ is the perturbation incremental strain field in $\mathcal{B}_{\mathrm{C}}$ with respect to the strain field $\dot{\boldsymbol{E}}_{\mathrm{M}}$.
By substituting Eq. (3.6) into Eq. (3.1a), the perturbation incremental strain fields turn out to be related by

$$\tilde{\dot{\boldsymbol{E}}}_{\mathrm{M}} = -\phi_{\mathrm{C}} \tilde{\dot{\boldsymbol{E}}}_{\mathrm{C}} \,. \tag{3.7}$$

Thus, the average incremental strains in the two phases given by Eq. (3.6) can be expressed as

$$\dot{\boldsymbol{E}}_{\mathrm{M}} = \dot{\boldsymbol{E}} - \phi_{\mathrm{C}}\, \tilde{\dot{\boldsymbol{E}}}_{\mathrm{C}} \,, \qquad \dot{\boldsymbol{E}}_{\mathrm{C}} = \dot{\boldsymbol{E}} + \phi_{\mathrm{M}}\, \tilde{\dot{\boldsymbol{E}}}_{\mathrm{C}} \,. \tag{3.8}$$

Since the incremental plastic strain $\dot{\boldsymbol{E}}^{\mathrm{P}}$ can be treated as an additional eigenstrain [64], the overall incremental eigenstrain becomes

$$\dot{\boldsymbol{E}}^{**} := \dot{\boldsymbol{E}}^{*} + \dot{\boldsymbol{E}}^{\mathrm{P}} . \tag{3.9}$$

In turn, by means of the Eshelby tensor $\boldsymbol{S}$, the perturbation field can be defined as

$$\tilde{\dot{\boldsymbol{E}}}_{\mathrm{C}} = \boldsymbol{S} : (\dot{\boldsymbol{E}}^{*} + \dot{\boldsymbol{E}}^{\mathrm{P}}) = \boldsymbol{S} : \dot{\boldsymbol{E}}^{**} . \tag{3.10}$$

Thus, the equivalent incremental strains, given by Eq. (3.8), are expressed as

$$\dot{\boldsymbol{E}}_{\mathrm{M}} = \dot{\boldsymbol{E}} - \phi_{\mathrm{C}}\, \boldsymbol{S} : \boldsymbol{E}^{**} \,, \quad \dot{\boldsymbol{E}}_{\mathrm{C}} = \dot{\boldsymbol{E}} + \phi_{\mathrm{M}}\, \boldsymbol{S} : \boldsymbol{E}^{**} \,. \tag{3.11}$$

By introducing the incremental strain definitions of Eqs. (3.11) into the stress equivalence condition Eq. (3.3), the total incremental eigenstrain of Eq. (3.9) can be obtained as

$$\dot{\boldsymbol{E}}^{**} = \boldsymbol{B} : \left(\boldsymbol{L}_{\mathrm{C}} : \dot{\boldsymbol{E}}^{\mathrm{P}} - [\![\boldsymbol{L}]\!] : \dot{\boldsymbol{E}} \right) \,, \tag{3.12}$$

where $[\![\boldsymbol{L}]\!] := \boldsymbol{L}_{\mathrm{C}} - \boldsymbol{L}_{\mathrm{M}}$ is the jump in the material elastic tensors of the two phases and the tensor $\boldsymbol{B}$ is defined as:

$$\boldsymbol{B} := \left(\boldsymbol{L}_{\mathrm{M}} + \phi_{\mathrm{M}}\, [\![\boldsymbol{L}]\!] : \boldsymbol{S} \right)^{-1} . \tag{3.13}$$

Therefore, by using the constitutive equations (3.2b) and exploiting the incremental strain fields (3.11) together with Eqs. (3.10) and (3.12), the incremental equivalent stress given by Eq. (3.1b) turns out to be

$$\begin{aligned} \dot{\boldsymbol{T}} &= \phi_{\mathrm{M}}\, \dot{\boldsymbol{T}}_{\mathrm{M}} + \phi_{\mathrm{C}}\, \dot{\boldsymbol{T}}_{\mathrm{C}} = \boldsymbol{L}_{\mathrm{M}} : \left(\dot{\boldsymbol{E}} - \phi_{\mathrm{C}}\, \dot{\boldsymbol{E}}^{**} \right) \\ &= \boldsymbol{L}_{\mathrm{M}} : \left[(\boldsymbol{I} + \phi_{\mathrm{C}}\, \boldsymbol{B} : [\![\boldsymbol{L}]\!]) : \dot{\boldsymbol{E}} - \phi_{\mathrm{C}}\, \boldsymbol{B} : \left(\boldsymbol{L}_{\mathrm{C}} : \dot{\boldsymbol{E}}^{\mathrm{P}} \right) \right] . \end{aligned} \tag{3.14}$$

Thus, the equivalent constitutive equation can be rewritten as

$$\dot{\boldsymbol{T}} = \boldsymbol{L}_1 : \dot{\boldsymbol{E}} - \boldsymbol{L}_2 : \dot{\boldsymbol{E}}^{\mathrm{P}} \tag{3.15}$$

where

$$\boldsymbol{L}_1 := \boldsymbol{L}_{\mathrm{M}} : (\boldsymbol{I} + \phi_{\mathrm{C}}\, \boldsymbol{B} : [\![\boldsymbol{L}]\!]) \,, \qquad \boldsymbol{L}_2 := \phi_{\mathrm{C}}\, \boldsymbol{L}_{\mathrm{M}} : \boldsymbol{B} : \boldsymbol{L}_{\mathrm{C}} \,. \tag{3.16}$$

This is a well-established approach to obtain the constitutive equations within the framework of Eshelby-Mori-Tanaka method, since the resulting equivalent elastic tensor $\boldsymbol{L}_1$ represents

the equivalent elastic tensor obtained for a purely elastic two-phase composite [62, 12]. Subsequently, the equivalent constitutive law for the inclusions in terms of average incremental strains can be obtained by the following steps. Substituting the incremental strains given by Eq. (3.11) into Eq. (3.2a), the incremental stress $\dot{\boldsymbol{T}}_{\mathrm{C}}$ turns out to be

$$\dot{\boldsymbol{T}}_{\mathrm{C}} = \boldsymbol{L}_{\mathrm{C1}} : \dot{\boldsymbol{E}} - \boldsymbol{L}_{\mathrm{C2}} : \dot{\boldsymbol{E}}^{\mathrm{P}} \tag{3.17}$$

where

$$\begin{aligned} \boldsymbol{L}_{\mathrm{C1}} &:= \boldsymbol{L}_{\mathrm{C}} - \phi_{\mathrm{M}}\, \boldsymbol{L}_{\mathrm{C}} : \boldsymbol{S} : \boldsymbol{B} : [\![\boldsymbol{L}]\!], \\ \boldsymbol{L}_{\mathrm{C2}} &:= \boldsymbol{L}_{\mathrm{C}} - \phi_{\mathrm{M}}\, \boldsymbol{L}_{\mathrm{C}} : \boldsymbol{S} : \boldsymbol{B} : \boldsymbol{L}_{\mathrm{C}}\,. \end{aligned} \tag{3.18}$$

Direct relationships between the stress descriptions. The equivalent constitutive equation can be more systematically derived by substituting into Eq. (3.1b) the constitutive equations for the individual phases and the associated equivalent strains, Eqs. (3.2) and (3.11), whereby the elastic tensors (3.16) appearing in Eq. (3.15) become can be rewritten in terms of those given by Eqs.(3.17) and (3.18):

$$\begin{aligned} \boldsymbol{L}_1 &= \phi_{\mathrm{C}}\, \left([\![\boldsymbol{L}]\!] : \boldsymbol{L}_{\mathrm{C}}^{-1}\right) : \boldsymbol{L}_{\mathrm{C1}} + \boldsymbol{L}_{\mathrm{M}}, \\ \boldsymbol{L}_2 &= \phi_{\mathrm{C}}\, \left([\![\boldsymbol{L}]\!] : \boldsymbol{L}_{\mathrm{C}}^{-1}\right) : \boldsymbol{L}_{\mathrm{C2}}\,, \end{aligned} \tag{3.19}$$

where $\left([\![\boldsymbol{L}]\!] : \boldsymbol{L}_{\mathrm{C}}^{-1}\right) \equiv \left(\boldsymbol{I} - \boldsymbol{L}_{\mathrm{M}} : \boldsymbol{L}_{\mathrm{C}}^{-1}\right)$ is a positive-definite tensor. Substituting Eqs. (3.19) into Eqs. (3.15) and (3.17) yields

$$\dot{\boldsymbol{T}} = \boldsymbol{L}_{\mathrm{M}} : \dot{\boldsymbol{E}} + \phi_{\mathrm{C}}\, \left([\![\boldsymbol{L}]\!] : \boldsymbol{L}_{\mathrm{C}}^{-1}\right) : \dot{\boldsymbol{T}}_{\mathrm{C}}\,. \tag{3.20}$$

Such an expression implies that, to within the elastic contribution $\boldsymbol{L}_{\mathrm{M}} : \dot{\boldsymbol{E}}$ of the homogenous elastic medium made of matrix material only, the equivalent incremental stress in the composite material corresponds to the incremental stress in the inclusions pre-multiplied by the positive-definite tensor $\phi_{\mathrm{C}}\, \left([\![\boldsymbol{L}]\!] : \boldsymbol{L}_{\mathrm{C}}^{-1}\right)$.

3.2.2 Evolution law for the plastic eigenstrain

As shown in the literature, a significant enhancement of damping capacity in CNT composites is obtained by dispersing CNTs aligned along a preferential direction. Moreover, in several applications (e.g., [11]; [29]), the CNTs are directly fabricated as aligned forests immersed in a hosting material. Thus, the CNTs can be assumed to be cylindrical inhomogeneous inclusions aligned, for example, along the 3-direction (see Fig. 3.2) that leads to a specific form of the Eshelby tensor $\boldsymbol{S}$ [64].

Note that, as mentioned, Eq. (3.5) states that limit conditions, enforced on the interfacial stress discontinuity, are automatically satisfied by limit conditions imposed on the stress within the inclusions. Thus, the activation of the interfacial stick-slip mechanism can be regulated through the CNT shear stresses (T_{C23}, T_{C13}), whence the stick-slip mechanism is described by the associated incremental plastic shear strains $\dot{\gamma}^{\mathrm{P}}_{13}$ and $\dot{\gamma}^{\mathrm{P}}_{23}$, corresponding to the only nontrivial components of $\dot{\boldsymbol{E}}^{\mathrm{P}}$. These shear strain rates turn to be the same (i.e., $\dot{\gamma}^{\mathrm{P}}_{13} = \dot{\gamma}^{\mathrm{P}}_{23} = \dot{\gamma}^{\mathrm{P}}$) as a result of the relevant symmetry.

The presented model for the elastoplastic-like behavior of the CNT inclusions can be framed within the *unified theory of viscoplasticity* of [14]. A simplification of such a general theory is adopted, by considering a perfect elastoplastic behavior, and a constitutive restriction in order to ensure rate independence. The evolution law for the effective plastic strain

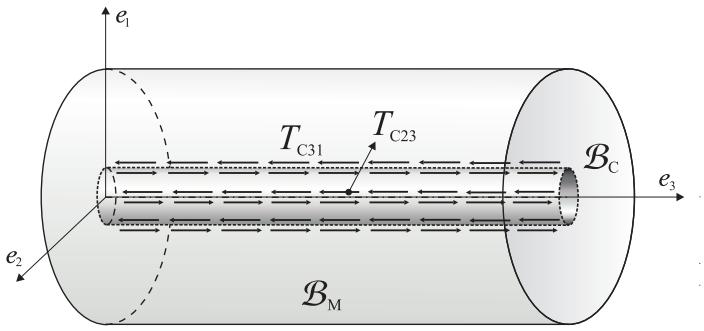

Figure 3.2: Representative volume element of a unidirectional CNT composite. Slippage of a carbon nanotube in the hosting matrix and the interfacial shear stress distribution.

rate $\dot{\gamma}^{\mathrm{P}}$ is then defined by the following functions and rules:

$$\dot{\gamma}^{\mathrm{P}} = \begin{cases} 0 & \text{if } \boldsymbol{T}_{\mathrm{C}} : \dot{\boldsymbol{E}} < 0, \\ \dot{\bar{\gamma}}^{\mathrm{P}} \left(\dfrac{\bar{T}^{\mathrm{VM}}}{S_{\mathrm{o}}} \right)^{m} \operatorname{sgn}(T_{\mathrm{C23}}) & \text{if } \boldsymbol{T}_{\mathrm{C}} : \dot{\boldsymbol{E}} \geq 0, \end{cases} \tag{3.21}$$

where the power function is regulated by the constitutive parameters S_{o} and m, whence $\dot{\bar{\gamma}}^{\mathrm{P}}$ is a constitutive function to be prescribed in order to ensure the rate independence of the model while $\bar{T}^{\mathrm{VM}}$ is a suitable measure of the effective stress taken in its ratio to the threshold stress S_{o}. The inequalities on the right-hand sides of the equation define the *loading/unloading* conditions. This equation, combined with the constitutive law of Eq. (3.15), leads to an equivalent nonlinear model which can be easily implemented in standard finite element codes. Moreover, it benefits from low computational costs, since there is no need to implement return mapping algorithms (see e.g. [77]). Indeed, definitions of either yielding functions or elastic domains are not explicitly used.

The main parameters introduced in the power function are the parameter S_{o} which represents the *interfacial shear strength* (ISS) between the two constituents, thus regulating the value of the CNT shear stress for which slippage at the CNT-matrix interface takes place, and the parameter m which determines the smoothness of the nonlinear stress-strain curves describing the behavior of the CNT phase.
Finally, in Eq. (3.21), the definition of $\bar{T}^{\mathrm{VM}}$ is consistent with the mechanical meaning of S_{o}; in fact, it represents the effective shear stress for the onset of inelastic strain at the CNT interface, derived by a micromechanical adjustment of the von Mises criterion. To this end, the octahedral (von Mises) shear stress function is applied to the interfacial stress discontinuity $\bar{\boldsymbol{T}} := [\![\boldsymbol{T}]\!]$:

$$\bar{T}^{\mathrm{VM}} = \left(\tfrac{3}{2}\, \bar{\boldsymbol{T}}^{\mathrm{dev}} : \bar{\boldsymbol{T}}^{\mathrm{dev}} \right)^{1/2} \tag{3.22}$$

where $\bar{\boldsymbol{T}}^{\mathrm{dev}}$ is the deviatoric part of the interfacial stress discontinuity $\bar{\boldsymbol{T}}$. The condition given by Eq. (3.5) allows to use the inclusion stress $\boldsymbol{T}_{\mathrm{C}}$ instead of the stress discontinuity $\bar{\boldsymbol{T}}$ and, in particular, to prove that both expressions for the stress deviatoric part and the von Mises stress are equivalent except for the non-dimensional scalar quantity c_μ, i.e.,

$$\bar{\boldsymbol{T}}^{\mathrm{dev}} = c_\mu\, \boldsymbol{T}_{\mathrm{C}}^{\mathrm{dev}}\,, \qquad \bar{T}^{\mathrm{VM}} = c_\mu\, T_{\mathrm{C}}^{\mathrm{VM}} \tag{3.23}$$

where c_μ is given by

$$c_\mu := (1 - \mu_{\mathrm{M}}/\mu_{\mathrm{C}})\,, \tag{3.24}$$

with μ_{M} and μ_{C} being the elastic shear moduli of the matrix and CNT phases, respectively. Therefore, the plastic evolution law given by Eq. (3.21) can be recast in terms of the stress $\boldsymbol{T}_{\mathrm{C}}$ only, as

$$\dot{\gamma}^{\mathrm{P}} = \begin{cases} 0 & \text{if } \boldsymbol{T}_{\mathrm{C}} : \dot{\boldsymbol{E}} < 0, \\ \dot{\bar{\gamma}}^{\mathrm{P}} \left(\dfrac{c_\mu T_{\mathrm{C}}^{\mathrm{VM}}}{S_{\mathrm{o}}} \right)^m \operatorname{sgn}(T_{\mathrm{C}23}) & \text{if } \boldsymbol{T}_{\mathrm{C}} : \dot{\boldsymbol{E}} \geq 0, \end{cases} \tag{3.25}$$

Rate independence in the one-dimensional problem

The rate-independent nature of the elastoplastic model is guaranteed by a suitable definition of the function $\dot{\bar{\gamma}}^{\mathrm{P}}$ in Eq. (3.25). As [14] suggested, a general *viscoplastic model* can be modified to become rate independent by zeroing the *overstress*. In the specific case, this is equivalently obtained by imposing $\dot{T}_{\mathrm{C}}^{\mathrm{VM}} \to 0$ as $T_{\mathrm{C}}^{\mathrm{VM}} \to S_{\mathrm{o}}$.

To this end, the investigation is limited to a one-dimensional problem, where all stress and strain tensors have as nontrivial components those corresponding to the nontrivial components of $\dot{\boldsymbol{E}}^{\mathrm{P}}$.

Consequently, the plastic consistency condition $\dot{T}_{\mathrm{C}}^{\mathrm{VM}} \to 0$ reduces to $\dot{T}_{\mathrm{C}\,23} \to 0$, while the incremental constitutive law, given by Eq. (3.17), can be expressed as

$$\dot{T}_{\mathrm{C}23} = L_{\mathrm{C}}^{\mathrm{E}}\, \dot{\gamma} - L_{\mathrm{C}}^{\mathrm{P}}\, \dot{\gamma}^{\mathrm{P}}. \tag{3.26}$$

Substituting Eq. (3.25) into Eq. (3.26) enforces the rate independence assuming

$$\dot{\bar{\gamma}}^{\mathrm{P}} = \frac{L_{\mathrm{C}}^{\mathrm{E}}\, \dot{\gamma}}{L_{\mathrm{C}}^{\mathrm{P}}}\,. \tag{3.27}$$

Thus, the evolution law (3.25) can be rewritten as

$$\dot{\gamma}^{\mathrm{P}} = \begin{cases} 0 & \text{if } \boldsymbol{T}_{\mathrm{C}} : \dot{\boldsymbol{E}} < 0, \\ \dfrac{L_{\mathrm{C}}^{\mathrm{E}}}{L_{\mathrm{C}}^{\mathrm{P}}}\, \dot{\gamma} \left(\dfrac{c_\mu T_{\mathrm{C}}^{\mathrm{VM}}}{S_{\mathrm{o}}} \right)^m & \text{if } \boldsymbol{T}_{\mathrm{C}} : \dot{\boldsymbol{E}} \geq 0. \end{cases} \tag{3.28}$$

The incremental constitutive laws can also be cast in terms of an elastoplastic tangent modulus for the CNT phase

$$\dot{T}_{\mathrm{C}23} = L_{\mathrm{C}}^{\mathrm{E}} \left[1 - \left(\frac{T_{\mathrm{C}}^{\mathrm{VM}}}{S_{\mathrm{o}}} \right)^m \right] \dot{\gamma} \tag{3.29}$$

while for the composite material the tangent modulus can be derived from

$$\dot{T}_{23} = \left[L_{1\,(23)} - L_{2\,(23)}\, \frac{L_{\mathrm{C}}^{\mathrm{E}}}{L_{\mathrm{C}}^{\mathrm{P}}} \left(\frac{T_{\mathrm{C}}^{\mathrm{VM}}}{S_{\mathrm{o}}} \right)^m \right] \dot{\gamma}. \tag{3.30}$$

Thermodynamical consistency

Considering general three-dimensional states of stress and strain, the assumptions made on the rate independence entail, through the plastic flow rule (3.28), the positive definiteness of the dissipation power:

$$P_{\mathrm{C}}^{\mathrm{D}} := \boldsymbol{T}_{\mathrm{C}} : \dot{\boldsymbol{E}}^{\mathrm{P}} = (T_{\mathrm{C}13} + T_{\mathrm{C}23})\, \dot{\gamma}^{\mathrm{P}} \geq 0\,. \tag{3.31}$$

These conditions guarantee thermodynamical consistency of the inelastic model for the inclusion phase. Such a condition can be verified for the one-dimensional problem here proposed by simply substituting the plastic flow rule (3.28) into the dissipation power definition (3.31).

As a consequence of condition (3.20) – which relates the stress description in the composite to that in the inclusion – it can be proved that the thermodynamical consistency of the inclusion material model implies the thermodynamical consistency of the composite material model. Indeed, due to the isotropic nature of the elastic tensors, we can integrate Eq. (3.20) over time and rewrite the result as

$$\boldsymbol{T} = \lambda_{\mathrm{M}}\,\mathrm{tr}(\boldsymbol{E})\,\boldsymbol{I} + 2\,\mu_{\mathrm{M}}\,\boldsymbol{E} + \phi_{\mathrm{C}}\,\left(c_\lambda\,\mathrm{tr}(\boldsymbol{T}_{\mathrm{C}})\,\boldsymbol{I} + 2\,c_\mu\,\boldsymbol{T}_{\mathrm{C}}\right) \tag{3.32}$$

where

$$c_\lambda := \frac{\lambda_{\mathrm{C}}\,\mu_{\mathrm{M}}/\mu_{\mathrm{C}} - \lambda_{\mathrm{M}}}{3\,\lambda_{\mathrm{C}} + 2\,\mu_{\mathrm{C}}}\,, \tag{3.33}$$

λ_{M} and λ_{C} are the first Lamé parameters of the matrix and CNTs, respectively.

Therefore, also the composite material is thermodynamically consistent because its dissipation power

$$P_{\mathrm{C}}^{\mathrm{D}} = 2[\mu_{\mathrm{M}}\,(E_{13} + E_{23}) + \phi_{\mathrm{C}}\,c_\mu\,(T_{\mathrm{C}13} + T_{\mathrm{C}23})]\,\dot{\gamma}^{\mathrm{P}} \tag{3.34}$$

turns out to be positive when the inclusion dissipation power (3.31) is positive, due to the stiffer properties of the inclusion material with respect to the matrix material (i.e, $c_\mu \geq 0$) and of the positive definiteness of the power exhibited by an elastic stress response of a purely matrix material. In particular, for the one-dimensional problem whereby $E_{13} = E_{23} = \gamma_{23}/2$ and $T_{\mathrm{C}13} = T_{\mathrm{C}23}$, the dissipation power becomes $P_{\mathrm{C}}^{\mathrm{D}} = 2(\mu_{\mathrm{M}}\,\gamma_{23} + 2\phi_{\mathrm{C}}\,c_\mu\,T_{\mathrm{C}23})\,\dot{\gamma}^{\mathrm{P}}$.

3.3 Numerical shear tests and measures of damping capacity

The numerical simulations are performed in Comsol with Matlab. The proposed model for unidirectional CNT nanocomposites is employed in the simplified context of uniform strain-driven tests. The interfacial slippage between CNTs and the surrounding matrix is emphasized considering a uniform state of equivalent shear deformation whereby the shear components between the CNT direction and the two orthogonal directions are the same.

Two types of linearly elastic polymers are chosen as hosting matrix, the thermosetting epoxy resin and the thermoplastic PEEK (poly-ether-ether-ketone). While the Poisson ratio ν for the two polymers is equal to 0.4, Young's modulus E for epoxy resin is chosen to be 5 GPa while it is 4.2 GPa for PEEK. Both polymers exhibit very good strength properties and chemical resistance, however the SWCNTs (E = 970 GPa and ν = 0.28) play a major role in defining the mechanical and damping properties of the nanocomposite [60, 74, 84, 99, 100]. It is convenient to collect all constitutive parameters of the two phases, including the parameters of the inelastic evolutive law, in the seven-dimensional vector $\mathbf{l} = (E_{\mathrm{M}},\, \nu_{\mathrm{M}},\, E_{\mathrm{C}},\, \nu_{\mathrm{C}},\, \phi_{\mathrm{C}},\, S_{\mathrm{o}}, m)$.

A set of monotonic shear tests is presented first to highlight the most significant characteristics and nonlinearities of the constitutive model. Subsequently, cyclic shear tests are carried out to investigate hysteresis and energy dissipation phenomena.

The nonlinearities of the model required a suitable numerical implementation of the constitutive law together with the plastic evolution law. The response curves for several loading

programs are computed to assess the influence of the constitutive parameters on the nonlinear material behavior. In particular, under cyclic loading conditions, the hysteretic energy dissipation is studied computing the damping capacity within physically meaningful ranges of the parameters. The numerical results, supported by a gradient-free optimization, reveal how the material parameters directly affect energy dissipation at the CNT-matrix interface and how to obtain optimal combinations of these parameters leading to maximum damping capacity.

3.3.1 Monotonic shear tests

The proposed monotonic test is a shear strain-driven test, where the assigned shear strain $E_{23} = \gamma_{23}/2$ is taken in the direction of the interfacial slippage between the two phases of the composite. Hence, by assigning the equivalent strain as a linear function of time t, $E_{23}(t) = k_{23}\,t$, the macroscopic response of the nanocomposite material is accordingly computed. The parameter k_{23} is the equivalent shear strain rate.

In accordance with the literature [68, 93], the parameters involved are set to the following reference values: $S_{\mathrm{o}} = 10\,\mathrm{MPa}$ for the ISS parameter; $m = 10$ for the evolution law's exponent; $\phi_{\mathrm{C}} = 10\%$ for the CNTs volume fraction; and $k_{23} = 10^{-5}/\mathrm{s}$ for the prescribed shear strain rate.

The nonlinear responses of the CNT nanocomposites shown in Fig. 3.3a exhibit a clear hardening elastoplastic behavior for both materials. Note that the shear stress at which the curves change their slopes is equal for both nanocomposites, thus implying that the nonlinear response of the material is independent of the chosen polymeric matrix. On the contrary, the Young modulus of the matrix affects the equivalent shear strain value at which CNT-matrix slippage occurs.

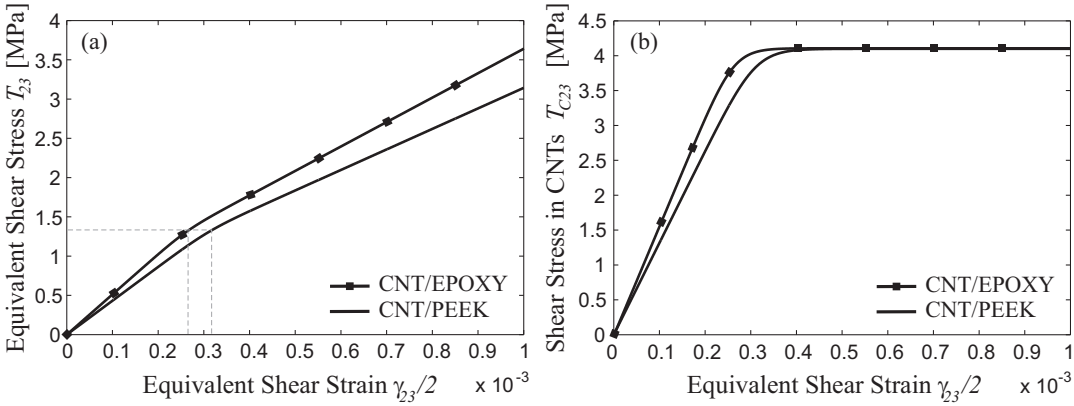

Figure 3.3: (a) Equivalent shear stress vs. strain and (b) shear stress in the CNTs vs. strain obtained by a shear strain-driven monotonic test for the CNT/Epoxy and CNT/PEEK nanocomposites.

On the other hand, the CNT stress T_{C23}, shown in Fig. 3.3b, computed as a function of the equivalent strain $\gamma_{23}/2$ exhibits an increasing trend by increasing the strain until reaching a plateau at 4.08 MPa, which is the CNT shear stress at which slippage occurs. The obtained value is comparable with the critical interfacial shear stress found by [68] in their experimental tests on CNT/PEEK composites. Past the onset of slippage, as prescribed by the power law (i.e., perfectly elastoplastic behavior), the stress $T_{\mathrm{C}23}$ remains constant. The sensitivity of the material model is assessed with respect to changes of the main constitutive

parameters ($\phi_{\rm C}, m, S_{\rm o}$). While m does not exhibit a significant influence on the nonlinear behavior of the nanocomposites, $\phi_{\rm C}$ and $S_{\rm o}$ represent the key constitutive parameters.

The monotonic shear test is performed for the CNT/PEEK composite, considering various CNT volume fractions and ISS values. In particular, variation of $\phi_{\rm C}$ between 5% and 20% yields the results shown in Fig. 3.4a, while variation of $S_{\rm o}$ in the range between 2.5 MPa and 20 MPa gives the stress-strain curves of Fig. 3.4b. As expected, the increase of $S_{\rm o}$ can significantly delay the onset of slippage; the case of perfect bonding is recovered in the limit for $S_{\rm o} \longrightarrow \infty$.

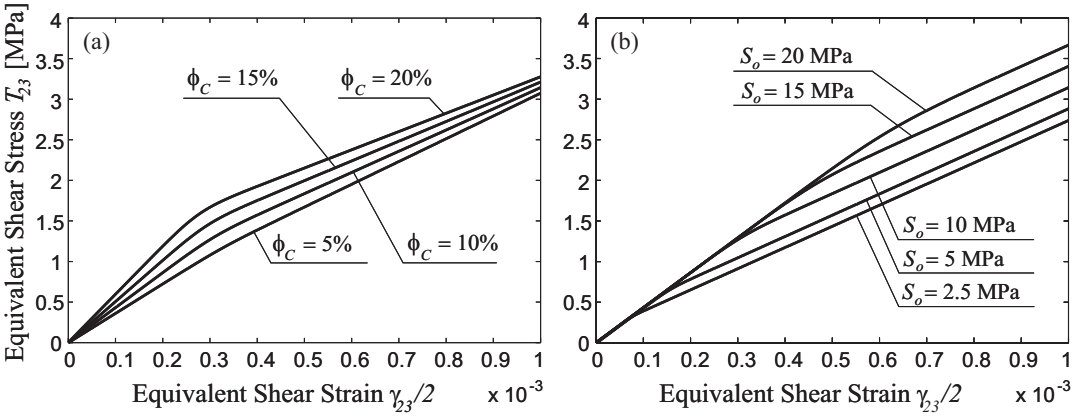

Figure 3.4: Equivalent shear stress-strain curves obtained varying (a) the CNT volume fraction $\phi_{\rm C}$ and (b) ISS parameter $S_{\rm o}$ for the CNT/PEEK composite.

3.3.2 Cyclic shear tests

Cyclic shear tests are performed by employing a finite element discretization of the unidirectional CNT nanocomposites. The cyclic shear strain-driven tests consist of loading/unloading cycles, under the prescribed sinusoidal shear strain law $E_{23}(t) = \gamma_0/2 \, \sin(2\pi t/t_0)$, where the shear strain amplitude is given by the constant value $\gamma_0/2 := k_{23}\, t_0$, with t_0 being the period.

The area enclosed by the hysteresis loops is a direct measure of the dissipated energy and, consequently, of damping capacity which can be estimated according to various measures, such as the logarithmic decrement Δ, the damping ratio ξ, the quality factor Q or the loss factor Λ. All these measures are expressed in terms of the *specific damping capacity* defined as the ratio between the energy $W^{\rm D}$ dissipated per cycle and the maximum elastic energy $W^{\rm E}$ stored during the first loading phase. The specific damping capacity per radiant represents the so-called *loss factor*, $\Lambda = W^{\rm D}/(2\pi\, W^{\rm E})$, which – for low levels of damping – is related to the logarithmic decrement and the damping ratio by

$$\Lambda = \Delta/\pi = 2\xi. \tag{3.35}$$

When the system is subject to a cyclic shear deformation, this gives rise to the stress response $T_{23}(t)$. By plotting the shear stress versus the prescribed shear strain over one cycle, the hysteresis cycles shown in Fig. 3.5 are obtained for the two nanocomposite materials; the top row is related to the CNT/PEEK nanocomposite and the bottom row to the CNT/Epoxy nanocomposite, respectively.

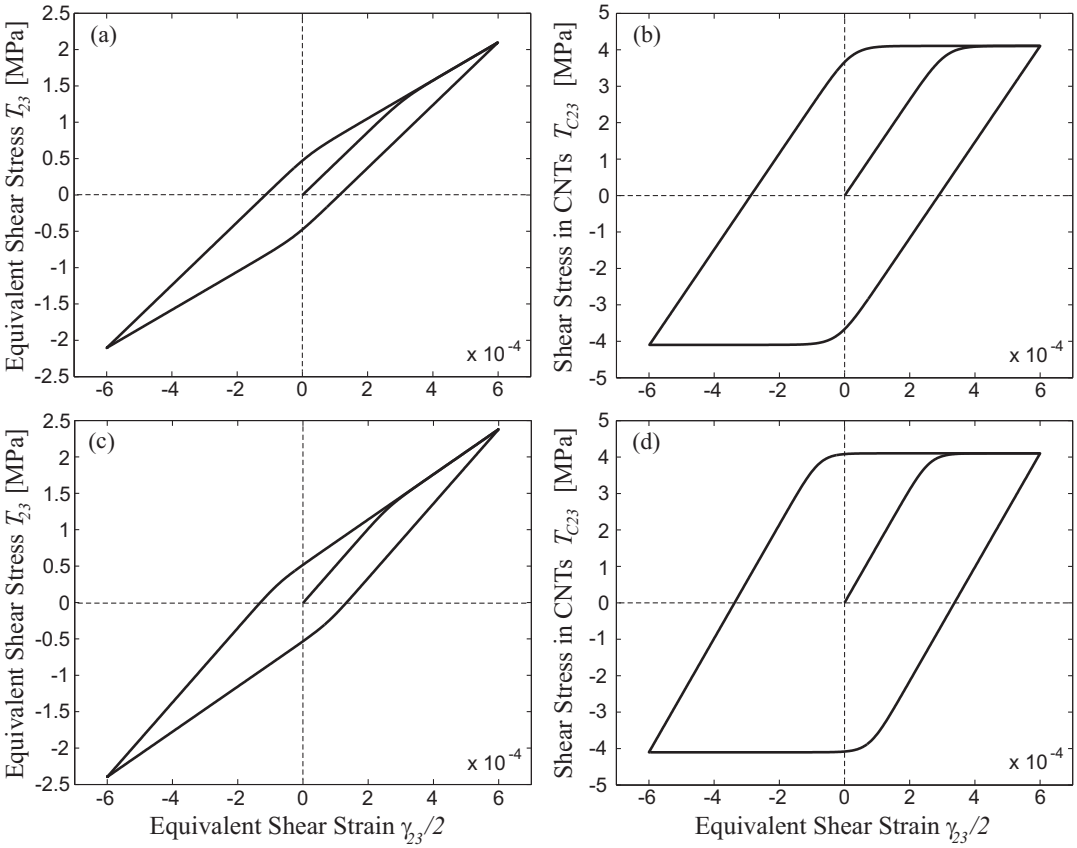

Figure 3.5: Stress-strain cycle for (top row) CNT/PEEK and (bottom row) CNT/Epoxy nanocomposite. Typical hysteresis loops are observed in the stress-strain curves obtained by a cyclic shear test driven by a sinusoidal equivalent shear strain. In parts (a) and (c), equivalent shear stress vs. shear strain, in (b) and (d) CNT shear stress vs. shear strain.

The area enclosed by a hysteresis loop is the energy dissipated per cycle W^{D}, which is taken in its ratio to the maximum energy W^{E} stored during loading (see Fig. 3.6).

By considering the generic loading/unloading cycle, a first direct estimate of the dissipated energy W^{D} in one cycle can be obtained as

$$W^{\mathrm{D}} = \int_{\mathcal{B}} \Big(\oint T_{23}\, dE_{23} \Big)\, dV \tag{3.36}$$

where dV is the volume element. The integral (3.36) is computed numerically using the Cavalieri-Simpson rule. The maximum elastic energy stored over one cycle W^{E} is determined as the total energy stored along the virgin loading branch

$$W^{\mathrm{E}} = \int_{\mathcal{B}} \Big(\int_{t_s}^{t_f} T_{23}\, dE_{23} \Big)\, dV. \tag{3.37}$$

The integral starts from the initial instant of time t_s until the maximum shear stress and strain are reached in the loading phase at time t_f. The computed damping ratio is found to be $\xi = 6.823\%$ for the CNT/PEEK nanocomposite, and $\xi = 6.983\%$ for the CNT/Epoxy nanocomposite.

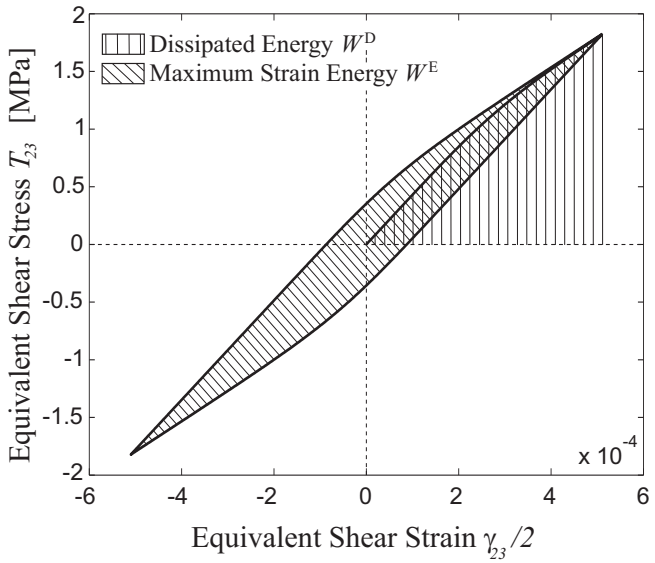

Figure 3.6: Evaluation of the dissipated energy per cycle W^{D} and the maximum elastic energy W^{E} stored during loading.

Alternative engineering computations of the damping ratio

The above described procedure for evaluating the damping capacity underestimates the damping ratio, since the computation of the maximum elastic stored energy in a cycle can be performed according to different choices for the reference elastic material. Alternative engineering approaches to estimate the maximum elastic stored energy W^{E} involve, for example, the computation of the secant or tangent stiffness associated to the virgin loading branch of the cycle and the evaluation of the area under the secant or tangent stiffness. Using the secant stiffness, the damping capacity may be overestimated while it is underestimated if computed using the tangent stiffness.
To appreciate the differences, computation of the maximum elastic stored energy W^{E} has been conducted using the secant stiffness method. Adopting the same reference values of the material parameters, the damping ratio has been found to be $\xi = 15.325\%$ for the CNT/PEEK nanocomposite, and $\xi = 15.735\%$ for the CNT/Epoxy nanocomposite. Therefore, in the following sections, the dissipative behavior of the nanocomposites is described by lower bound curves of the damping ratio, obtained by a conservative estimate.

3.4 Hysteretic dissipation in carbon nanotube polymeric composites: parametric studies and optimization

To the aim of maximizing the nanohysteretic energy dissipation by searching for optimal combinations of the constitutive parameters, a sensitivity analysis is carried out with respect to variations of γ_0, S_{o}, ϕ_{C}, and m. The analysis allows to identify the ranges of parameters and strain amplitudes for which the damping capacity can be maximized.

The cyclic tests are first carried out to determine the influence of the strain amplitude γ_0. Fig. 3.7a shows the damping ratio versus (half) the strain amplitude. It is clear that the (specific) dissipated energy is highly dependent on the applied strain amplitude. Values of

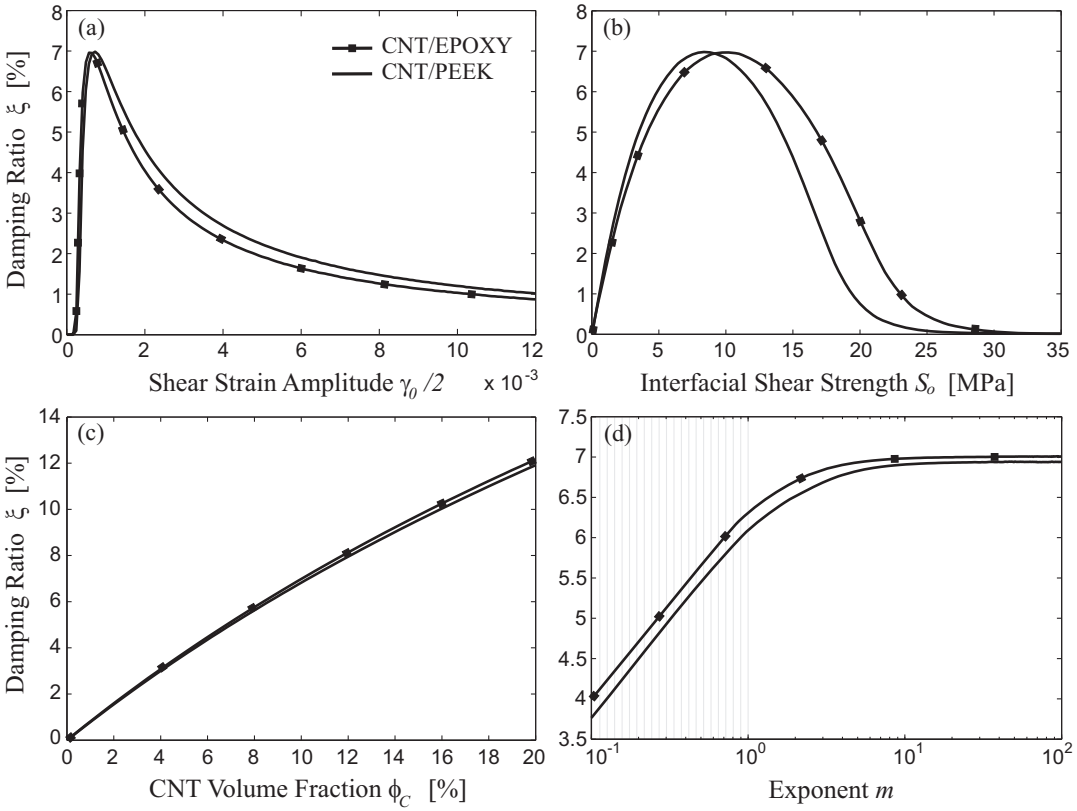

Figure 3.7: Damping ratio ξ of the CNT/PEEK and CNT/Epoxy nanocomposites versus (a) the amplitude of the shear strain $\gamma_0/2$, (b) the interfacial shear strength S_o, (c) the CNT volume fraction ϕ_C, (d) the exponent m of the evolution law.

the strain amplitude ranging between 10^{-5} and $3 \cdot 10^{-3}$ determine a great enhancement of damping capacity. This is assessed by observing the behavior of the damping ratios for the two nanocomposites which exhibit the peak value $\xi = 6.994\%$ when $\gamma_0/2 = 7.035 \cdot 10^{-4}$ for the CNT/PEEK and $\xi = 6.982\%$ when $\gamma_0/2 = 6.120 \cdot 10^{-4}$ for the CNT/Epoxy composite, respectively. This result is in agreement with the experimental and numerical results found in the literature (e.g., [57, 84]) for CNT composites and highlights some key dissipative features of these nanocomposites. The same trend in damping capacity quantified by the damping ratio is found in a rich variety of hysteretic systems and devices governed by rate-independent hysteresis models [52].

The cyclic shear tests are then carried out varying the ISS parameter S_o in the range [0.1, 35] MPa (see Fig. 3.7b). This parameter strongly affects the critical values of the shear strain and stress [76] and typical values reported in literature are ranged between 2 and 15 MPa for the CNT/PEEK composites and from 2 up to 500 MPa for CNT/Epoxy composites [93]. Thus, due to the fabrication processes and the chemical bonds between CNTs and matrix, the ISS turns out to be an extremely variable parameter which can be further modified by interfacial functionalization [59]. The results in Fig. 3.7b indicate that the optimal value of S_o, for the given CNT volume fraction and strain amplitude, is around 8.3 MPa for the CNT/PEEK and 10.2 MPa for the CNT/Epoxy nanocomposite, respectively. The limit shear stress of the composite material for which yielding (slippage) occurs increases with S_o; on the contrary, a stronger interface delays the sliding between CNTs and matrix to higher stress

and strain levels.

Another meaningful parametric study concerns the CNT volume fraction ϕ_{C} which is taken to vary between 1% and the limiting value of 20%. As expected, Fig. 3.7c shows that the concentration of CNTs in the hosting matrix strongly affects the dissipative capabilities of the nanocomposite. A high volume fraction ϕ_{C} increases the dissipated energy per cycle W^{D} more significantly than any other parameter, and the damping ratio ξ reaches values of the order of 13% for the CNT composites.

A sensitivity study is also carried out for the exponent m in the range $[10^{-1},\ 10^{2}]$. The interesting dependence of the damping behavior on the exponent m is shown in Fig. 3.7d which shows a monotonically increasing trend up to $m = 10$. Past this value the damping ratio peak becomes nearly constant, implying that the parameter m does not affect any more the damping capacity of the nanocomposites since the transition between the elastic and plastic phase is not smooth for $m \geq 10$ (i.e., there exists a neat knee in the response functions).

Subsequently, for a better understanding of the influence of the parameters on the damping ratio trend, damping ratio curves versus shear strain amplitude are obtained and shown in Fig. 3.8 which portrays the CNT/PEEK results in the left column and the CNT/Epoxy results in the right column, respectively.

In Figs. 3.8a and 3.8b the damping ratio is shown for different values of S_{o}, while m and ϕ_{C} are set to the reference values: $m = 10$ and $\phi_{\mathrm{C}} = 10\%$. Each curve has the same trend and the peak of the damping ratio translates along the strain amplitude axis as the strength S_{o} increases. Interestingly, for given higher values of S_{o}, past the peak of ξ, the damping ratio curve shows that a better damping response of the material can be obtained with respect to those with a lower ISS. Thus, the choice of a high ISS could be reasonable in some cases.

The same kind of parametric study is conducted considering variations of the exponent m while the values of S_{o} and ϕ_{C} are set to the reference values. Figs. 3.8c and 3.8d confirm the trend shown in Fig. 3.7d. All damping ratio curves achieve their maximum values at nearly the same strain amplitudes while the values of the peaks, affected by the exponent m, reach the maximum as m approaches 10.

The sensitivity of the damping capacity is also studied varying the CNT volume fraction ϕ_{C} in the range [5, 20]% while S_{o} and m are set to the reference values. Figs. 3.8e and 3.8f show results that are in perfect agreement with the parametric studies conducted in the previous section on the CNT volume fraction (see Fig. 3.7c). The increase of the CNT concentration considerably enhances the dissipative characteristics of the material, provided that a good CNTs dispersion is ensured. The peak damping ratio is $\xi_{\max} = 12.180\%$ for CNT/PEEK and $\xi_{\max} = 12.163\%$ for CNT/Epoxy, respectively, when $\phi_{\mathrm{C}} = 20\%$.

The various parametric studies suggest interesting conclusions about the determination of suitable sets of parameters which can maximize damping in nanocomposite materials.

3.4.1 Optimization of the damping capacity: differential evolution approach

The sensitivity studies show that a suitable optimization of the nanocomposite damping capacity can be achieved by seeking global maxima in the space of allowable constitutive parameters of the model. In engineering vibration and noise control problems, the material has to be designed to undergo specific strain amplitude ranges within given frequency ranges so as to exhibit the most effective response.

A first attempt to perform such a damping optimization is carried out in the restricted space of the constitutive parameters $(\phi_{\mathrm{C}}, S_{\mathrm{o}}, m)$ within the physically reasonable range of

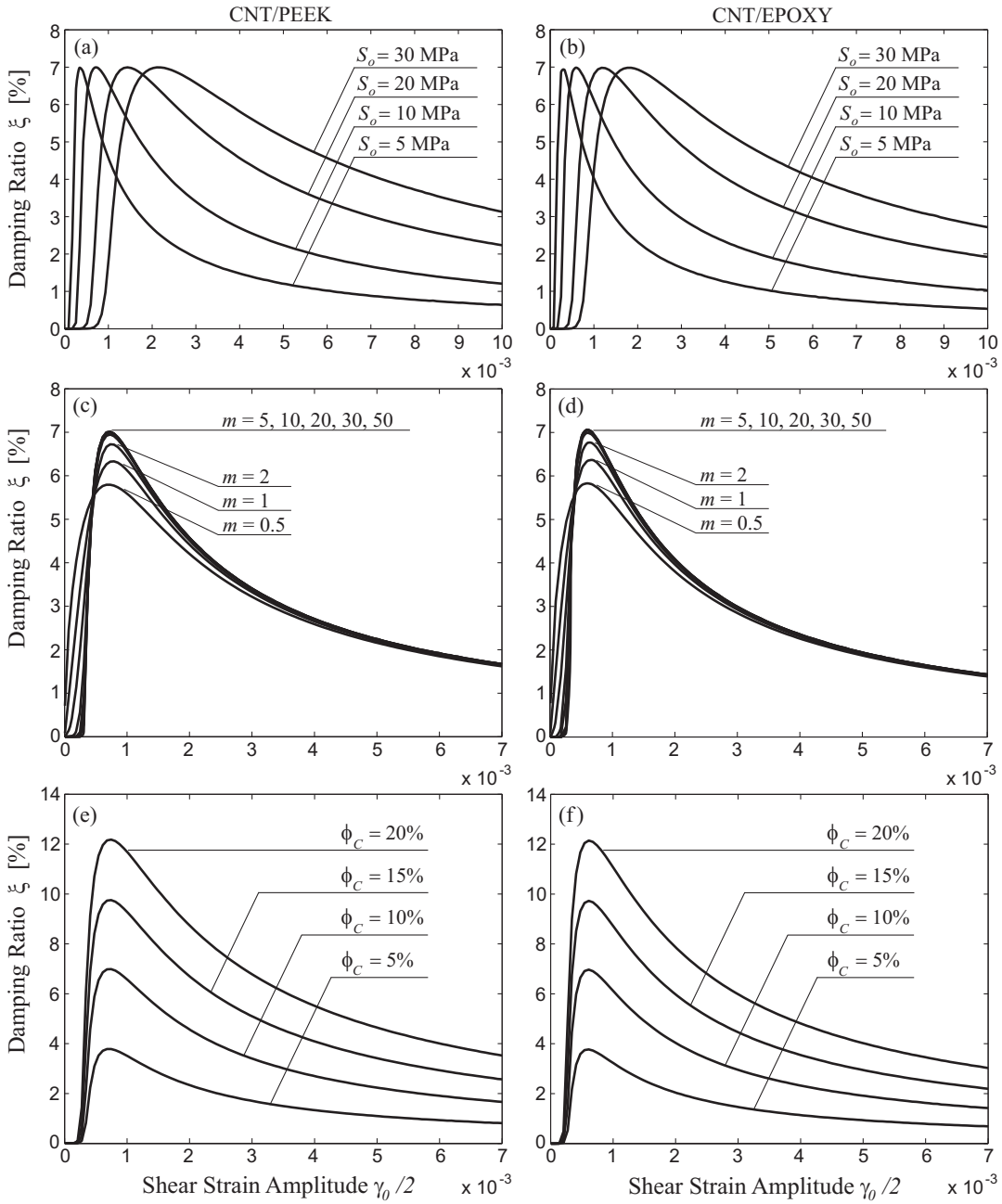

Figure 3.8: The high sensitivity of damping capacity with respect to the constitutive parameters of (left column) CNT/PEEK and (right column) CNT/Epoxy nanocomposite is illustrated. Damping ratio ξ versus the strain amplitude (a)-(b) varying S_o, (c)-(d) varying m and (e)-(f) varying the CNT volume fraction ϕ_C with the reference values of the main parameters taken to be: $S_o = 10$ MPa and $m = 10$ and $\phi_C = 10\%$.

strain amplitude $\gamma_0/2 \in [10^{-5}, 10^{-2}]$. The optimization is performed by applying the differential evolution algorithm [81], so that the optimal combination of the constitutive parameters can be determined letting the parameters vary in properly chosen ranges. The differential evolution (DE) algorithm turns out to be an efficient stochastic direct search method which

provides the optimum combinations of the material parameters that maximize the damping ratio, which is assumed as the objective function.
Furthermore, the DE requires low computational costs as well as represents it overcomes the need to differentiate an often discontinuous objective function since it is not based on the computation of the objective function gradients.
For each parameter to identify, an initial guess is give by choosing an arbitrary value within a selected reasonable range. A range is set for the n parameters p_i to identify, with $i = 1, ..., n$ and, for each of them, a number of m values are picked from a uniform probability distribution within the given ranges. Thus, first, an initial population of parameters is given as a number m of n-dimensional vectors listing a combination of values assigned to the parameters. The first algorithm step consists in the computation of the objective function for each parameters combination give in the initial population. The parameters combination that better satisfy the objective function are selected to generate a new population. The algorithm is iterative and at each iteration a new population is formed by considering a restricted range of values for each parameter. The number of iteration is generally assigned after a first numerical investigation. Each iteration consists in a number of computational cycles equal to the number m of vectors in the population.
Considering the jth cycle of the kth iteration, with $j = 1, ..., m$ and $k = 1, ..., l$, the steps performed by the DE algorithm are the following: (a) a target vector $\mathbf{p}_t$ is selected from the current population; (b) three vectors $\mathbf{p}_p$, $\mathbf{p}_a$, $\mathbf{p}_b$ are randomly selected from the population with the condition that they must be all different; (c) a mutated vector $\mathbf{p}_m$ is generated by adding to the vector $\mathbf{p}_p$ the perturbation F($\mathbf{p}_b$-$\mathbf{p}_a$), with F = 0.9 (differential perturbation procedure); (d) a trial vector $\mathbf{p}_{tr}$ is generated by taking the components from both $\mathbf{p}_t$ and $\mathbf{p}_m$; this procedure, called cross over, is performed by randomly extracting a number from a uniform probability distribution on the range [0,1]. If the number is greater than 0.5 the parameter is taken from $\mathbf{p}_m$, otherwise it is taken from $\mathbf{p}_t$; (e) the objective function is computed for both trial vector $\mathbf{p}_{tr}$ and target vector $\mathbf{p}_t$, the vector providing the higher vale of the objective function survives and is introduced in the new generation.
Finally, the last generation obtained is given by the parameters vector that maximizes the damping ratio objective function. The following suitable ranges are chosen for the main parameters: $5 \leq S_0 \leq 50$ MPa, $1 \leq m \leq 50$ and $10^{-6} \leq \gamma_0/2 \leq 10^{-2}$. The optimization analysis have been conducted for the subsequent values of the CNT volume fractions $\phi_{\mathrm{C}} = [5, 10, 15, 20]\%$. A summary of the results are given in Tables 3.1 and 3.2 for the CNT/PEEK and CNT/Epoxy composites, respectively, while Fig. 3.9 shows the corresponding damping ratio versus strain amplitude curves

Table 3.1: Optimal damping ratio ξ for a CNT/PEEK composite. ϕ_{C} is the CNT volume fraction, S_{o} the interfacial shear strength, m the plastic evolution law exponent and, $\gamma_0/2$ the equivalent shear strain velocity.

ϕ_{C} [%]	S_{o} [MPa]	m [−]	$\gamma_0/2 \times 10^{-3}$	ξ [%]
5	50	27.06	3.52	3.81
10	33.38	39.54	2.40	7.02
15	50	43.97	3.52	9.78
20	40	50	2.94	12.20

Both CNT/PEEK and CNT/Epoxy nanocomposites can reach a damping ratio equal to $\xi = 7\%$ for the chosen reasonable CNT volume fraction equal to 10%. Comparing the damping ratio of the CNT/Epoxy composite ($\xi = 7\%$) with that of the pristine epoxy

Table 3.2: Optimal damping ratio ξ for a CNT/Epoxy composite. ϕ_{C} is the CNT volume fraction, S_{o} the interfacial shear strength, m the plastic evolution law exponent and, $\gamma_0/2$ the equivalent shear strain rate.

ϕ_{C} [%]	S_{o} [MPa]	m [−]	$\gamma_0/2 \times 10^{-3}$	ξ [%]
5	50	46.41	5.40	3.78
10	37.89	50	2.29	7.01
15	49.23	45.10	2.96	9.77
20	38.94	35.66	2.41	12.18

($\xi = 0.1 \div 0.2\%$), an outstanding increment of the order of $350 \div 700\%$ is found.

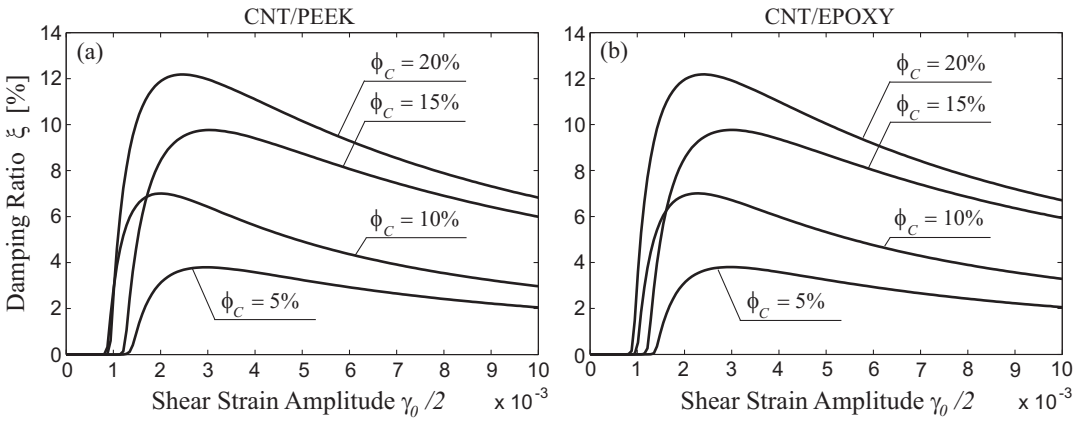

Figure 3.9: Optimized damping ratio curves are reported for the CNT/PEEK (a) and CNT/Epoxy (b) nanocomposites. The optimization procedure, performed by using the differential evolution algorithm, is carried out for different values of the CNT volume fraction.

Therefore, the gradient-free optimization based on a differential evolution algorithm has been successfully exploited to find global maxima for the damping capacity of two nanocomposites (i.e., CNT/Expoxy, CNT/PEEK) with selected volume fractions of CNTs by changing the shear strength, the exponent of the power law while the shear strains are varied in a given range.

The proposed meso-scale constitutive theory can be generalized to the case of randomly oriented CNTs or can be improved by introducing refinements such as, for example, the aspect ratio of the carbon nanotubes, as well as deterioration factors for the elastic moduli of the equivalent material which account for the evolution of full irreversible debonding between nanofibers and matrix.

In order to make this theoretical model and efficient and effective reliable tool for the design of the CNT nanocomposite properties, it is necessary to verify and validate the theory through an accurate campaign of experimental tests.

Chapter 4

Fabrication of CNT Nanocomposites

4.1 Introduction

In this chapter the first phase of the conducted experimental campaign is presented.
CNT/thermosetting and CNT/thermoplastic nanocomposite samples were prepared using different weight fractions of high- and low-aspect ratio CNTs. The prepared nanocomposite samples were characterized and tested to the purpose of (i) exploring the constituent materials features, and (ii) collecting extensive experimental data for the validation and optimization of the theoretical model presented in the previous chapter.
A major highlight, arising from experimental studies conducted in the last decades, is the challenging choice of methods and techniques to be adopted for the nanocomposites fabrication. Indeed, the manufacturing processes are crucial for the definition of the final nanocomposite product features. The manufacturing methods and their parameters must be properly selected and set in order to release the full potential of CNT nanocomposites. The processing techniques determine the filler dispersion, orientation, and filler-matrix interfacial interactions. Great attention must also be payed to the morphological characteristics of the row materials employed, namely the selected carbon nanotubes and polymers, in order to improve the nanocomposite performance.
There are several issues in nanocomposite fabrication processes to be addressed, such as controlling CNT orientation, achieving good interfacial bonding of CNTs with the matrix, but the main challenge is represented by the difficulty in achieving appropriate levels of nanofiller dispersion. This particular problem arises because CNTs are nanoparticles with very high surface to volume ratio and the van der Waals forces between the CNTs make it difficult to separate them and achieve homogenous dispersion within a polymer matrix. Thus, CNTs have a tendency to entangle and agglomerate. These agglomerates generally act as stress concentrators and reduce the mechanical properties of the nanocomposites.
There is a wide range of processing methods which can be employed for the CNT/polymer composites fabrication. The choice strictly depends on the kind of polymer in which the CNTs have to be embedded, but there is no single processing technique recommended for all types of polymers and nanofillers. This is attributed to the interdependence of many factors, such as polymer chemistry, and durability of the nanofillers in the processing environment.

The first issue here addressed in the design and preparation of CNT composites is the selection of the polymer matrices in which the CNTs will be embedded and the dispersibility of CNTs in those polymers.

4.2 Exploring the material properties

The CNT/polymer composites, here considered, are mostly thought for structural applications. Therefore, the polymer matrices, in which the strong CNT nanofillers are embedded, must be high-performance matrices.
In order to attain unconventional macroscopic behavior in the nanostructured material, some specific features have to be exhibited by the polymeric hosting matrices of the nanocomposite. The most relevant material properties to consider are: (i) strength, stiffness and toughness, which imply the selection of high-performance polymers, (ii) the glass transition temperature of the polymers, that should ensure stable mechanical properties of the matrix in the operating range of temperatures of the composite material, (iii) the crystallinity of the polymer structure, which generally affects the thermal and mechanical properties of the material, such as the ductility of the polymer. For instance, in crystalline polymers the polymeric molecular chains fold together in ordered structures, which means that the chains show a partial alignment. This may result in an improvement of the overall behavior of the material, or may represent a drawback when the introduced CNT fillers interfere with the latter structure of the surrounding polymer matrix.
Among all the polymers which are eligible for their employment in structural applications, it is possible to classify the polymer matrices according to the specific kind of interactions that occur between their molecular chains and the outer sidewalls of CNTs. The linkage mechanisms that may arise between the CNTs and polymer chains, in fact, strictly depend on the molecular structure and the reactivity of the latter.
For the purpose of this work, four different polymers have been selected.

4.2.1 Thermosetting and thermoplastic polymer matrices

Four polymers were chosen as hosting matrices: a well-known thermosetting polymer, namely an epoxy resin, and three thermoplastic polymers, i.e., Polypropylene (PP), Polybutylene Terephthalate (PBT) and Polycarbonate (PC).
Thermosetting composites have been preferred in the last decades for structural applications because, after curing, they do not change their features at high temperatures. But, thermoplastic polymers have been recently assessed in the evolving aerospace and automotive industry since they show significant savings in process costs and energy. Typically, thermoplastics are heated, formed and cooled rapidly, while thermoset polymers must be held at elevated temperatures for hours to crosslink. Moreover, thermoplastic materials can exhibit a high impact resistance, high damage tolerance in addition to be flame-retardant and resistant to chemical attack.

Epoxy resin. The first chosen polymer is the *epoxy resin* L20 from R&G, which is a bisphenol-A-(epichlorhydrin) mixed with a low percentage of two other epoxy resins and combined with a suitable curing agent, also known as *hardener*, which is the EPH161 of the same Company (R&G Faserverbundwerkstoffe GmbH), made with a combination of amino functional groups.

Indeed, thermosetting epoxy resins are two-component system polymers which need the presence of suitable curing agents with specific functional groups in order to crosslink and dispose their chains in ordered cell structures. The selection of the curing agent is as crucial as the choice of the polymer, because it changes the reactivity of the whole polymer and affects the resulting mechanical and thermal properties.
The selected thermosetting polymer is characterized by high heat-resistance and ideal mechanical strength properties for applications in the aerospace and automotive fields. Furthermore, the low viscosity of this resin makes it suitable for all processing methods and allows for a good dispersion of CNTs.

Polypropylene. The first adopted thermoplastic is the *polypropylene* (PP) Finalloy EPB-18 (Total Petrochemicals, Belgium), a commodity widely used thermoplastic, which is a mineral-filled and impact modified polypropylene-based compound. This light thermoplastic is characterized by a semi-crystalline structure and a very low density. Since PP is non-polar, it absorbs very little water. It is generally tough and very flexible, with a Young modulus of 1.4 GPa and takes significant damage prior to breaking, thus exhibiting good resistance to fatigue. In specific cases, this allows polypropylene to be used as an engineering plastic, also because is a reasonably economic material.

Polycarbonate. The second thermoplastic is an amorphous engineering polymer, namely, the *polycarbonate* (PC) Makrolon 2600 (Bayer MaterialScience AG, Germany) with medium-viscosity grade. Polycarbonate is well known for its toughness and optical transparency. The carbonate group provides two ether linkages in the backbone, thus, resulting in good molecular flexibility well below PC glass transition temperature. The bisphenol A group in polycarbonate, which is present in many epoxies and vinyl esters, imparts both rigidity and toughness. It has a Young modulus of 2.3 GPa and, thanks to its good mechanical properties and heat-resistance, is commonly used for a variety of engineering applications.

Polybutylene terephthalate. The third polymer is the high-viscosity grade *polybutylene terephthalate* (PBT) VESTODUR 3000 (Evonik Industries, Germany), which is a semi-crystalline, high-performance engineering polymer. Polybutylene terephthalate is used frequently for injection molding applications and belongs to the polyester polymers family. Due to the two extra methylene groups in its repeated structure, it absorbs less water and has better impact strength compared to polyester terephthalate (PET). In addition the very good heat and solvent resistance, PBT is an ideal candidate polymer for reinforcement composites and shows very good mechanical properties with a Young modulus of 2.6 GPa.

4.2.2 Carbon nanotubes

The nanofiller morphology is probably the most relevant material feature to consider when high mechanical properties are required in nanocomposites. The ratio between the length and the diameter of the carbon nanotubes, known as aspect ratio, is indeed a significant parameter of which depends the interfacial surface area between the CNT and the polymer matrix. If CNTs with small diameter are employed, a large augmentation of the surface CNT/matrix interface area is generally achieved, which implies a larger available area for the stress transfer between the two constituents of the nanocomposites. On the other hand, a higher length of the CNTs may improve the mechanical strength of the nanocomposite. Furthermore, since during processing the CNTs are usually damaged and shortened, a higher CNT initial length may limit the decrease of the CNTs aspect ratio after the sample prepa-

ration.
In this work, nanocomposite samples were prepared by employing two types of commercially available carbon nanotubes, the multi-walled nanotubes (MWNTs) NC7000 (Nanocyl S.A., Belgium), and the single-walled nanotubes (SWNTs) Tuball (OCSiAl, USA).

Multi-walled carbon nanotubes. The NC7000 MWNTs are characterized by a carbon purity of 90% and a surface area of $250 - 300$ m^2/g, while the outer nanotube diameter is 10 ± 3 nm, and the average nanotube length is 1.5 μm. The aspect ratio, α, of the selected MWNTs is around 155, which is a low value. The short length of the NC7000 make them not the best choice for enhancing the mechanical properties of the polymer matrix, but it represent an advantage during the dispersion process in the matrix, because the low aspect ratio CNTs have less tendency to entangle and do not significantly increase the viscosity of the mixture during fabrication steps. The effects of this short nanotubes will be compared with the ones of longer SWNTs.

Single-walled carbon nanotubes. The Tuball SWNTs are characterized by a carbon purity higher than 85% and a surface area of $500 - 700$ m^2/g. The mean diameter of Tuball SWNTs is 1.8 ± 0.4 nm, while the mean length is higher than 5 μm. They are characterized by a high aspect ratio around 2777, which is beneficial for an efficient load transfer and hence improved mechanical properties at low percolation thresholds.

4.3 Processing of CNT Nanocomposites

4.3.1 CNT/Epoxy nanocomposites fabrication

As first process, CNT/epoy nanocomposites were produced with a low weight fraction of NC7000 MWNTs, equal to 0.5 wt%. The samples were prepared implementing several processes, especially with the objective of improving the CNTs dispersibility. To enhance the CNT dispersion and the nanocomposites mechanical properties the amino-functionalization of the nanotubes was employed as chemical treatment for some of the prepared samples.

CNT amino-functionalization. Chemical functionalization, also called covalent functionalization, can take place by adding various functional groups on the CNTs surface. The best functional-group candidates for this chemical treatment are the carboxyl groups (-COOH) and the amino groups (-NHR). The choice between these two molecules is regulated by the quality and efficiency of the final interactions between the CNTs and the polymer chains, and by the need to simplify the process for the production of the nanocomposite. From this perspective, it is possible to note that, in order to create some bonds with epoxy, (i) carboxyl groups require a higher temperature than amino groups, and (ii) carboxyl groups are generally less reactive with epoxy than amino groups.
This leads to the choice of the amino-functionalization process, which is a three-step process. It consists of oxidation, acyl-chlorination, and amidation (see Fig.4.1).
The chemical oxidation is a well-established, efficient method to purify the pristine CNTs, promoting dispersion and surface activation at the same time. It is commonly carried out via harsh acid treatments which cause fragmentation and defect sites on the surfaces of the CNTs. Oxygen-containing functional groups (mainly carboxyl and hydroxyl groups) are then introduced on the graphitic surface, localizing on the generated defect sites. This treatment may lead up to directly use the carboxylated-CNTs for composite fabrication, or serve as

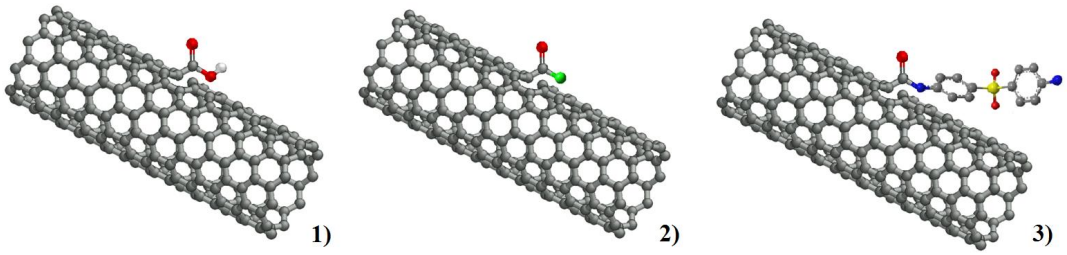

Figure 4.1: The three steps of the amino-functionalization: 1) oxidation, 2) acyl-chlorination 3) amidation

first step for further modification/functionalization, depending on the required application of the CNTs. The most typical performed oxidation is a liquid-phase oxidation treatment carried out with nitric acid HNO3. This is a very aggressive acid and is commonly used by exposing the CNTs to the acid from 4 up to 48 hours. Although this procedure is effective, the combination of the sonication used to disperse the CNTs in the acid solution and the harshness of the acid are responsible for high damage and degradation of the graphitic network of nanotubes, thus seriously affecting and limiting their mechanical properties. For this reason, in our specific case, we explored different possibilities in order to successfully fulfill the functionalization without causing severe damage to the CNTs structure. Following the results of Avilés et al. [6], we selected a gentler procedure, using nitric acid HNO_3 and hydrogen peroxide H_2O_2. Some relevant oxidation parameters, such as acid concentration in the solution, treatment exposure time and sonication power have been properly balanced to achieve the best possible results. The pristine multi-walled CNTs were treated with a HNO_3 acid solution at 3.0 M concentration by mechanically stirring the mixed solution for 15 minutes at a controlled temperature of 60°C. Then, the mixture was ultrasonicated at low power for 2 hrs, in order to promote disentanglement and dispersion of the MWCNTs. This exposure time was particularly low compared to traditional processes in order to reduce the nanotubes shortening and fragmentation effects. Subsequently, the MWCNTs have been filtered and washed with distilled water, until pH was close to 7 (see Fig.4.2). Subsequently, the same procedure was repeated substituting the HNO_3 acid solution with hydrogen peroxide H_2O_2 (30% v/v) solution with the aim of completing the oxidation in a milder way. Finally, CNTs are dried in a vacuum oven for 4 hrs at 150°C to eliminate residual water and make them ready for the next step.

The acyl-chlorination represents the intermediate step of the functionalization. It consists in the substitution of the hydroxyl (-OH) groups with the chlorine to increase the reactivity of the functional groups on the CNTs surface, which would otherwise require a very high temperature to react with the amino groups. Thus, the nanotubes are treated with thionyl chloride $SOCl_2$, and dimethylformamide DMF (20:1 concentration solution), stirred at 70°C for 24 hrs, and afterwards, filtered and dried in a vacuum oven. This procedure facilitates the following attachment of the amino group on the CNT surface, by replacing the chlorine with the 4,4'-Diaminodiphenyl sulfone (DDS) group, according to the amidation third step. Thus, the acyl-chlorinated CNTs reacted with DDS in DMF solution at 130°C under nitrogen for 6 days. The excess of the DDS was then removed by washing the amino-functionalized CNTs with ethanol and finally, drying them in vacuum oven overnight at room temperature [40].
An experimental campaign was conducted to test the resulting functionalization effects of the CNTs, via thermogravimetric analysis (TGA) and X-ray photo-electron spectroscopy (XPS), that will be shown in the next chapter. In any case, a first evidence of the occurred

Figure 4.2: Liquid-phase oxidation treatment of the MWNTs consisting of a) the magnetic stirring, b) ultrasonic bath, c) filtering, washing and d) drying.

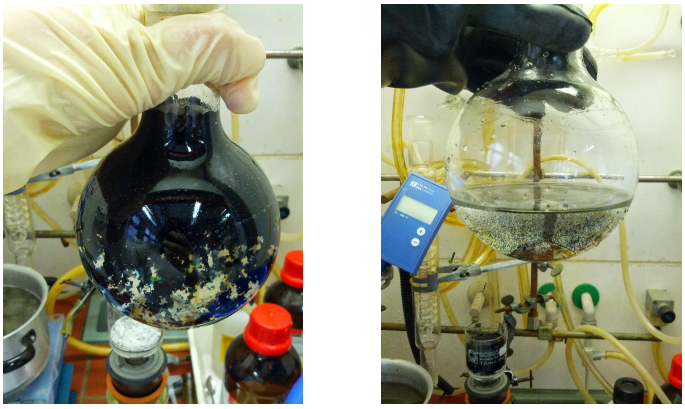

(a) *CNTs dispersed in acid at the end of the oxidation treatment.*

(b) *CNTs dispersed in water, showing their hydrophilic nature after functionalization.*

Figure 4.3: CNT solution dispersions during the functionalization process.

functionalization is already given by dispersing the CNTs in a polar solvent, like ethanol or even water. The hydrophobic pristine nanotubes do not generally disperse in water but they deposit in water and, in particular, they show the tendency to aggregate due to van der Waals interaction forces. On the contrary, after the treatment, the CNTs become hydrophilic, since the functional groups make the CNTs more reactive with the polar solvents and they reject one each other. Therefore, due to the functional groups on CNTs outer sidewalls, the CNTs appear well dispersed in the resulting solution (see Fig.4.3).

NC7000/epoxy nanocomposite preparation. Both pristine and chemically functionalized CNTs were embedded in the epoxy resin in order to compare the mechanical and dissipative behavior of nanocomposites with different CNT/matrix interfaces. In the first case, pristine CNTs, as received, were directly integrated in the epoxy, while, in the second case, a functionalization process was required to obtain some reactive sites on the CNTs outer sidewalls.
The first phase of the fabrication process is the integration of the designated MWNTs NC7000 in the epoxy resin L20.
In order to disperse the CNTs in the low viscous epoxy, different mechanical methods were

used. Initially the ultrasonication bath technique was adopted, but – since the ultrasonic bath is generally a mild treatment – some large CNT agglomerations were found in the composite. Then, a more effective horn ultrasonication method has been employed, varying the amplitude and time of ultrasonication, to optimize the result.
After the mechanical dispersion of the nanotubes in the epoxy resin, the mixture was degassed for 2 hours in a vacuum oven to remove air bubbles. Subsequently, a speed mixer was used to well mix the epoxy resin with the hardener EPH161, by setting the proper time and rotating speed of the process. A vacuum pump is finally employed for the filling of the metal mold with the CNT/epoxy mixture to be cured. The curing temperature was set at 60°C and the post-curing temperature at 100°C in order to get a nanocomposite glass transition temperature around 90 °C.

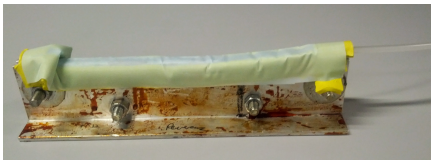

(a) *Metal mold.*

(b) *Vacuum bag.*

Figure 4.4: Preparation of the metal mold for the filling under vacuum. A specific membrane is predisposed on the metal mold to avoid the leak of the epoxy/CNT mixture when the vacuum is applied.

The obtained samples shown in Fig.4.5, were characterized via light microscopy to estimate the CNT agglomeration degree followed by a campaign of mechanical tests to investigate their mechanical properties. The nanocomposites with CNT dispersed (i) via ultrasonic bath, (ii) via ultrasonic horn, (iii) via a previous functionalization treatment and ultrasonic horn, were compared.

4.3.2 CNT/thermoplastic nanocomposites fabrication

In order to collect a wide spectrum of experimental data, nanocomposites with three different thermoplastic polymers and two types of CNTs were prepared. The main features of the prepared CNT nanocomposites, in terms of CNT type, polymer and CNT weight fraction, are summarized in the following table (Table 4.1).

The nanocomposites were produced by twin-screw extrusion. For the CNT/PP nanocomposites an intermeshing corotating twin-screw ZE 25 Berstorff extruder was used. A temperature programme increasing from 180°C to 200°C, a screw speed of 500 min, and a throughput of 10 kg/h were adopted as mixing conditions.

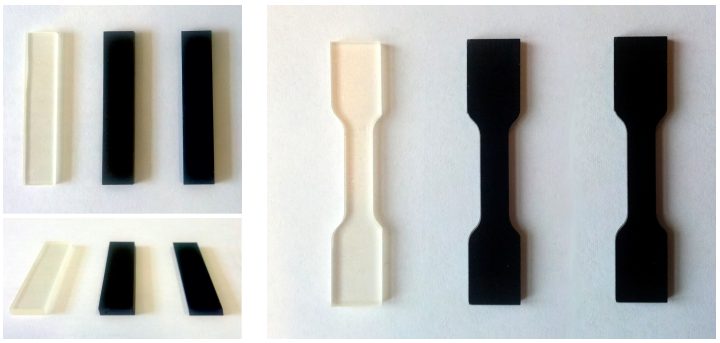

(a) *Epoxy and 0.5 wt% MWNT/Epoxy nanocomposites bars.*

(b) *Epoxy and 0.5 wt% MWNT/Epoxy nanocomposites dog-bone specimens.*

Figure 4.5: MWNT/Epoxy nanocomposite samples prepared for tensile tests.

Table 4.1: List of CNT/thermoplastic nanocomposite prepared.

CNT	Polymer	CNT weight fraction ϕ_C [%]
MWNTs	PP	(0.5, 1, 2, 5)
MWNTs	PC	(0.5, 2)
MWNTs	PBT	(0.5, 2)
SWNTs	PC	(0.5, 2)
SWNTs	PBT	(0.5, 2)

The nanocomposites with the two engineering polymers, namely PC and PBT, were prepared by using a DSM15 Xplore twin-screw microcompounder with a chamber volume of 15 cm^3. The microcompunder is equipped with two rotating screws located in a chamber that is heated up to the melting temperature of the polymer. The device is fed with specific amounts of polymer pellets and the desired CNT weight fraction. Adjusting the temperature adopted for the process, the rotational speed of the twin screws, the force applied for the material mixing and the mixing time, it is possible to obtain a well-dispersed CNT nanocomposite, without incurring polymer degradation. The parameters for the mixing of CNTs in the melted thermoplastics - including melting temperature, mixing rotational speed time and force, were optimized according to the work of Schoer et al. [80]. Different mixing conditions were applied for each polymer: (i) 280°C melt temperature, 250 rpm mixing speed, and 5 minutes mixing time for PC nanocomposites; (ii) 265°C melt temperature, 200 rpm mixing speed, and 5 minutes mixing time for PBT nanocomposites.
Extruded strands were pelletized and injection molded, for CNT/PP composites, while compression molded for both CNT/PC and CNT/PBT composites.
Typical PP injection molding conditions were adopted for the PP nanocomposites [63], using the Ergotech 100/420-310 injection molding machine with a two-cavity mold. The machine was fed by a flash gate at a melt temperature of 240°C. Plates of 80 mm× 80 mm× 2 mm were obtained and cut in dog-bone specimens parallel to the flow direction.
On the other hand, a compression molding procedure was optimized for PC [45] and PBT [50] nanocomposites in order to get uniform and bubble-free plates by means of a PW 40EH Weber hot press. The optimization required the adjustments of parameters, such as the melting temperature - to re-melt the pellets and forge the material into its final shape -, the

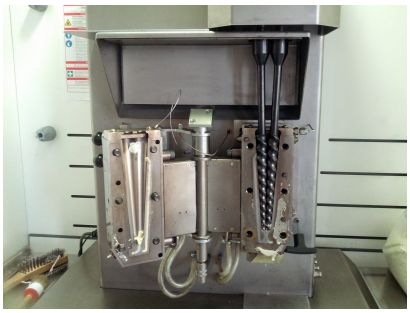

(a) *Twin-screw extruder DSM Xplore.*

(b) *Feeding of the extruder with polymer pellets.*

(c) *Polymer strands after the melt mixing.*

Figure 4.6: Microcompounder DSM Xplore: some intermediate steps during the melt mixing procedure.

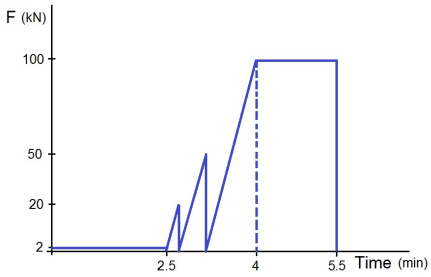

(a) *Pressing conditions.*

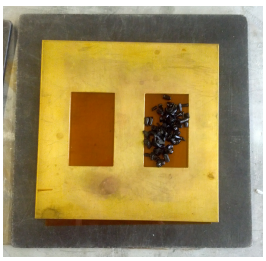

(b) *Metal mold feeded with nanocomposite pellets.*

(c) *Paul Otto Weber press.*

Figure 4.7: Compression molding procedure.

press force, the force speed, and the duration of the pressing process. During this process, air bubbles might also be formed, if the force speed is too high, and degradation of the material might be observed - with a subsequent re-agglomeration of CNTs -, if the set temperature and time are not well calibrated. For these reasons, an improved procedure with a gradual stepwise increase of the compression force and pressing time was adopted (see Fig.4.7).
Nanocomposites granules, placed inside a rectangular frame between the hot plates, were pre-heated at 280°C and 265°C for PC and PBT, respectively, for 2.5 minutes. A pressing speed of 6 mm/min was applied with a load program featuring a sequence of ramps with increasing amplitude and load release until a maximum load magnitude of 100 kN was reached and kept constant for 1.5 minutes. The obtained plates 60 mm× 60 mm× 2 mm were cut in dog-bone specimens and beam-like bars (see Fig.4.8).

The characterization of such a rich number of samples, prepared with several CNT weight fractions and two types of CNTs (NC7000 MWNTs and Tuball SWNTs), will be presented in the next chapters. The samples dimensions and geometry were suitably set for the scheduled mechanical tensile and DMA tests, for which the results will be provided.

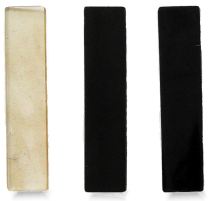

(a) *PC and CNT/PC nanocomposite bars.*

(b) *PBT and CNT/PBT nanocomposite bars.*

(c) *PP and CNT/PP nanocomposite dog-bone specimens.*

(d) *PC and CNT/PC nanocomposite dog-bone specimens.*

(e) *PBT and CNT/PBT nanocomposite dog-bone specimens.*

Figure 4.8: CNT/thermoplastic nanocomposite samples prepared for DMA and tensile tests.

Chapter 5

Nanocomposites Morphology Characterization

5.1 Introduction

In this chapter the main morphological and micro/nanostructural features of the nanocomposites are analyzed and discussed. The CNT agglomeration and macrodispersion states of the prepared CNT/polymer composites are characterized via light microscopy (LM) and digital image analysis; the qualitative evaluation of CNT nanodispersion is conducted via SEM analysis, while the CNTs morphology is investigated through TEM analysis.
The morphological analysis of the CNT nanocomposites consists of (i) the quantification of the CNT agglomerates at the micro-level, (ii) the definition of the CNT dispersion and distribution that concerns the uniformity of the individualized nanotubes presence in the hosting matrix, and (iii) the identification of the main features of the nanofiller itself, such as shape and aspect ratio variability. The characterization of the CNT dispersion and distribution in the matrix allows to better understand the relationship between the material structure and the mechanical behavior of the nanocomposite. Indeed, the mechanical and damping properties of the nanocomposites are strongly affected by several microstructural parameters. The design of a high-performance nanocomposites requires a deep knowledge of the material features at both micro- and nano-scale in order to optimize the nanocomposites processing conditions.

5.2 Optical light microscopy for the CNT macrodispersion

The CNT macrodispersion refers to the dispersion of CNT agglomerates or bundles and their uniform distribution in the nanocomposite. The CNT macrodispersion of nanofiller/polymer systems is generally investigated via optical light microscopy (LM) [45, 70], which is a widely used method – also in industry contexts – due to the ease and speed of the method compared to other microscopy techniques. LM can provide an estimate of the volume fraction of the

dispersed CNTs, as the CNT agglomerates can be easily distinguished from the matrix using visible light. The advantages of using LM rather than SEM and TEM include the short times for specimen preparation and the relative simplicity of the test procedure. In addition, the information provided by LM can represent the bulk material with significantly less number of images compared to electron microscopy. The drawback of LM is that it is a 2D analysis and cannot describe the absolute dispersion of CNTs which is a feature of the 3D structure. However, LM is carried out in this work to evaluate the relative change of CNT dispersion for the different nancomposites and the quantification of the CNT macrodispersion revealed to be sufficient.
Micrographs can be analyzed using image processing algorithms that are extensively used by other scientific communities, for instance in the biological and medical fields. Digital image processing have been adapted to analyze CNT materials, as shown by Pegel and co-workers [70]. Such algorithms allow rapid processing of a large number of micrographs to obtain a statistically confident description of the level of filler dispersion in a CNT nanocomposite. Among the quantitative methods adopted in LM analysis, the threshold method is one of the most effective. The method uses the feature-based approach that correlates a threshold value with the number of objects that has a roundness of ¡0.5 μm . A selected threshold value is then used to quantify the agglomerate area fraction, defined as the ratio between the cumulative area of the CNT agglomerates and the total area of the micrographs in thin sections.

5.2.1 LM samples preparation

The preparation of good specimens is a crucial step in LM. The samples must be cut in thin slices, also called sections, in order to observe the CNT nanocomposites specimen in transmission mode, letting the light pass through the specimen surface.
Microtoming is the preparation technique of these sections between 5 and 15 μm in thickness that must be thin, undeformed, and flat. In order to obtain very thin sections, the specimen is mounted on the microtome by either the embedding in a mould or by self-support using a chuck. Securing the specimen in the chuck is crucial to prevent any movement during microtomy and facilitates consistent section thickness. If embedding is required, an epoxy can be used for this purpose. The cutting knife is typically selected according with the desired thickness of the section and the ductility of the sample material. Polymers may be sectioned with tungsten carbide or diamond. There are some issues limiting microtoming that can affect the structure of the polymer section. Common artifacts on the sections includes striations, non-uniform thickness, wrinkling and chatter marks. Generally, these artifacts are caused by knife-related factors (i.e. damaged, incorrect angle, blunt) and procedure-related factors (i.e. sectioning speed, section thickness, cutting surface size, specimen temperature, presence of contaminants). These defects are undesirable as they will interfere with the image analysis of the micrographs. There are remedies for some defects such as knife related factors that can be avoided by using sharp knives or selecting an appropriate knife material based on the application. However, the process of minimizing defects are also dependent on the skill of the operator preparing the specimens and on the material under investigation.

5.2.2 Method

In LM, the light transmitted or reflected by the specimen is channeled through a system of lenses to produce an image at suitable magnifications. The resolution of the image is

limited by the wavelength of visible light (400 - 700 nm), the objective lens and features of the specimen itself. For CNT-filled polymer systems, LM can provide information on filler agglomerates such as shape, size, and distribution. A digital camera attached to the microscope is used to record the images for processing and analysis.
Thin sections of 10 μm thickness were prepared and cut in the direction perpendicular to the pressed plates plane by using an RM 2055 microtome (Leica) at room temperature. The thin sections were imaged with a BH2 microscope in transmission mode combined with a camera DP71 (Olympus Deutschland GmbH) considering the entire cross-sectional area. In the obtained micrographs, the CNT agglomerates appear black and clearly in contrast with the polymer surrounding matrix.
The optical micrographs were analyzed with image processing software, ImageJ (Rasband, 1997). The image processing procedure to estimate the CNT agglomeration areas from LM micrographs consists of the following steps: background correction, binarizing the image, identifying an appropriate threshold to quantify the CNT agglomerates, computing the CNT agglomeration areas.
The agglomerate area ratio A_{CNT}/A_0 was determined by calculating the ratio of the area A_{CNT} of remaining agglomerates to the total area of the micrograph A_0 ($\sim$0.6 mm^2). Agglomerates larger then 5 μm were taken into account for this calculation, according to ISO 18553 standards. For the quantification, fifteen cuts were investigated for each sample, taking images from different positions along the plate dimensions. The standard deviation of the agglomerate area ratio was also computed together with the agglomerate area ratio value.
Another interesting measurement of the CNT macrodispersion degree can be provided by the macrodispersion index D, evaluated as the ratio of the dispersed volume fraction of CNTs to the whole CNT volume fraction. The following expression is adopted:

$$D := 1 - \frac{f\left(\frac{A_{CNT}}{A_0}\right)}{V_{CNT}}, \tag{5.1}$$

where f is the packing density of CNTs and represents the effective volume of the filler ($f = 0.25$ is considered by referring to Kasaliwal et al.[45]), while V_{CNT} is the CNT volume fraction in percentage.
When D is closed to zero, it indicates poor CNT dispersion, while a macrodispersion index of 100% means that no agglomerates of size larger than 1 μm^2 can be found, indicating the best state of dispersion.

5.2.3 Images investigation and results

Some of the micrographs of the CNT/polymer nanocomposites are here reported together with an estimate of the CNT agglomerate area fraction.

CNT/Epoxy nanocomposites micrographs. A comparison of the not well-dispersed CNT composite (Fig.5.1a), the composite with CNT improved dispersion (Fig.5.1b), and the functionalized CNT composite (Fig.5.1c), was carried out with the light microscopy to identify the agglomerate area fractions. The ratio between the CNT agglomeration area and the total area A_{CNT}/A_0 in the light microscopy images was found to be 3.78% for the composite of Fig.5.1a, 1.25% for the one of Fig.5.1b and 0.37% for the best functionalized CNT composite of Fig.5.1c. It is well accepted that when the value of the agglomerate area fraction is equal or lower than 1%, the nanocomposite is assumed to have a good dispersion of CNTs.
As shown, the covalent amino-functionalization is extremely effective for the CNTs integrated in the epoxy resin, as shown in Fig.5.1c. The diamino groups (DDS), attached on

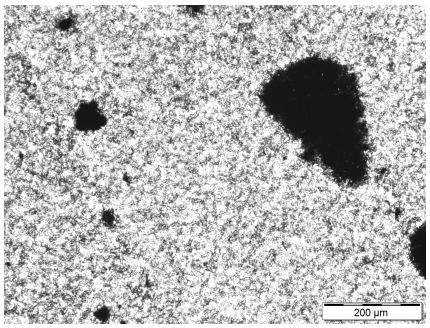

(a) *Pristine CNT/epoxy composite prepared by adopting ultrasonic bath.*

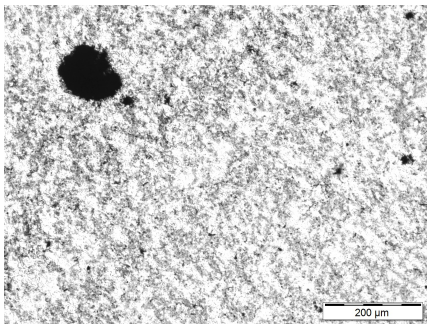

(b) *Pristine CNT/epoxy composite prepared via ultrasonic horn.*

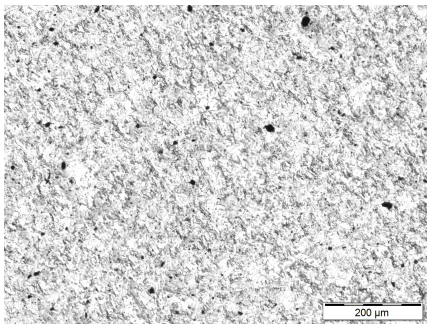

(c) *Amino-functionalized CNT/epoxy composite prepared using ultrasonic horn.*

Figure 5.1: Micrographs of the three 0.5 wt% CNT/Epoxy nanocomposite samples prepared with different techniques.

the surface of the NC7000 MWNTs, are highly reactive with the oxirane rings in the epoxy resin and allow the CNTs disentanglement due to the steric repulsion among the functional groups.Thus, a very good dispersion and uniform distribution of the CNTs in the composite sample is achieved.

Carbon nanotubes XPS and TGA analysis. In order to characterize the functionalized CNTs, X-ray photo-electron spectroscopy (XPS) and a thermo-gravimetric analysis (TGA) were carried out, thus determining the degree of functionalization and the concentration of amino groups on the CNTs (see Table 5.1 and Table 5.2). The comparison between the wide-scan spectra of the pristine NC7000 CNTs (see Fig.5.2) and the amino functionalized CNTs (see Fig.5.3), clearly shows the binding energy peaks associated with Carbon and Oxygen, which are present in both the spectra, and the peaks for Nitrogen and Sulphur, which appear only in the spectrum of the functionalized CNTs, since they are the chemical species introduced by the covalent treatment with the DDS groups.

Table 5.1: Content of the elements on the surface of the CNTs obtained by the XPS analysis for the pristine MWNTs NC7000.

Element	Atomic Concentration [%]
C	97.49
O	2.51
Al	traces

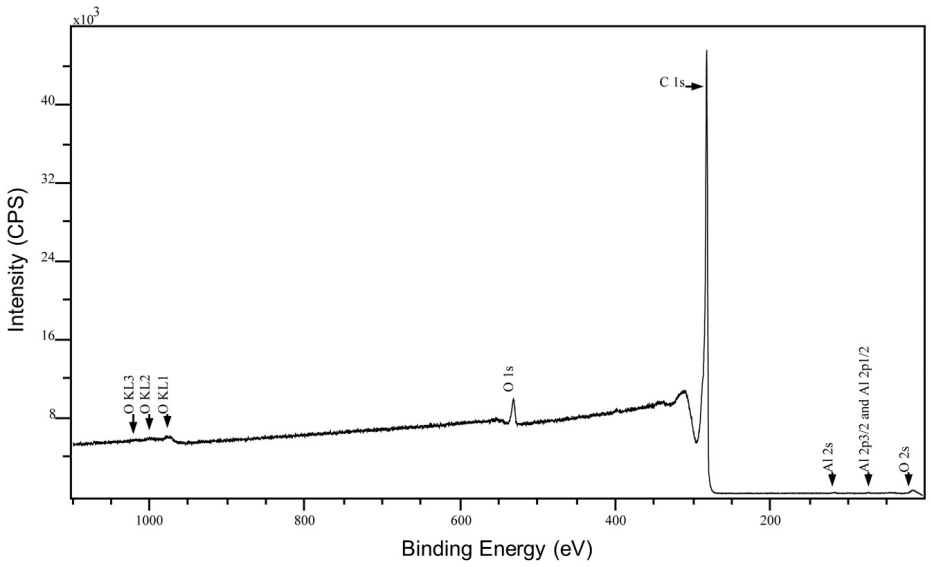

Figure 5.2: XPS analysis of pristine multi-walled carbon nanotubes NC7000.

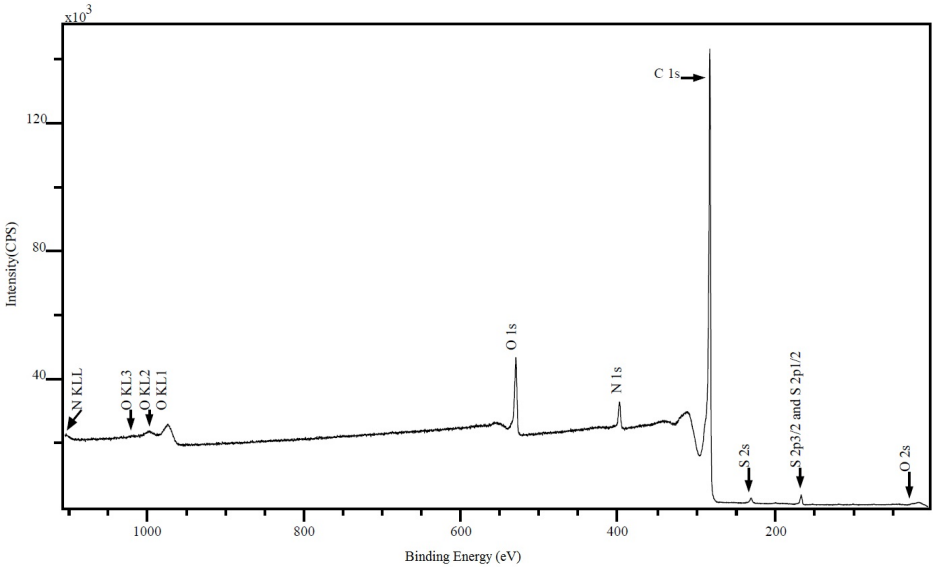

Figure 5.3: XPS analysis of amino-functionalized multi-walled carbon nanotubes NC7000, where the presence of Nitrogen and Sulfur indicates that functional groups are on the MWNTs surface.

Table 5.2: Content of the elements on the surface of the CNTs obtained by the XPS analysis for the amino-functionalized MWCNTs NC7000.

Element	Atomic Concentration [%]
C	90.24
N	6.06
O	3.03
S	0.67

The thermal stability of the functionalized CNTs is also investigated through thermogravimetric analysis, reported in Fig.5.4. The raw MWNT curve shows a little uniform weight loss in all the temperature range, which is equal to 2.73%. This is in accordance with literature results and it indicates the presence of impurities from the catalysts employed in the CNT growth process.

On the other hand, the initial weight loss in the amino-functionalized CNT curve could

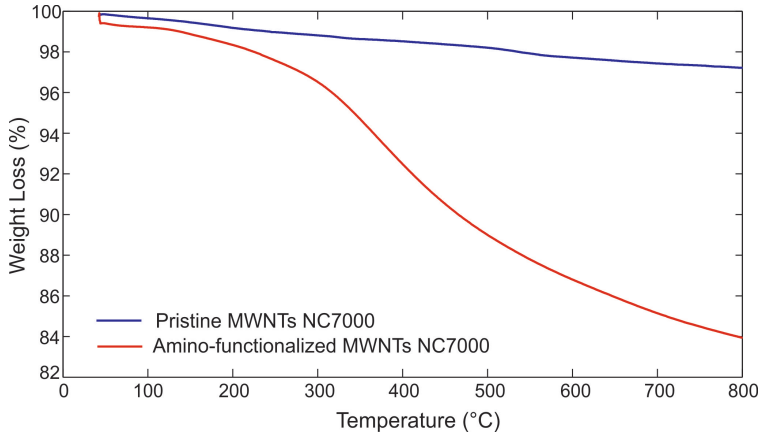

Figure 5.4: TGA analysis of pristine and amino-functionalized multi-walled carbon nanotubes NC7000 performed with the TGA Q5000 (TA Instruments) under nitrogen atmosphere, with a heating rate of 10°C/min, from RT to 800°C.

be due to the evaporation of adsorbed water, while the loss between 150°C and 350°C is usually ascribed to the decomposition of oxygen groups (carboxyl or anhydride groups). The final weight loss among 350°C and 600°C is instead caused by the decomposition of the more stable amido bonds between the DDS groups and the carbon nanotubes. This results in a total weight loss of 15.43%.

CNT/thermoplastic nanocomposites micrographs. The state of macrodispersion of the NC7000 MWNTs and Tuball SWNTs nanocomposites was investigated for all samples via optical light microscopy. Fig.5.5 and 5.6 show LM micrographs and the related agglomerate area fractions for PC and PBT nanocomposites with different contents of the two types of CNTs.

Both PC and PBT nanocomposites exhibit a low agglomerate area ratio A/A_0 especially when MWNTs are employed ($A/A_0 < 1\%$). In contrast, significant differences are observed when SWNTs are dispersed in both matrices, where larger agglomerates appeared with an elongated shape, typical for Tuball SWNTs nanotubes. The worst state of dispersion is reported for 2 wt% SWNT/PBT nanocomposites with 3.13%.

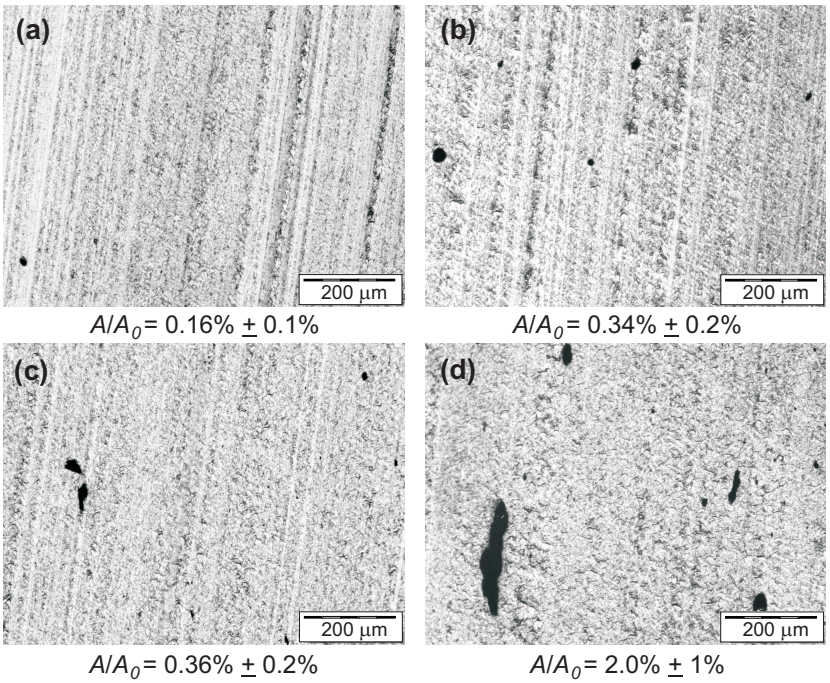

Figure 5.5: Light microscopy images and corresponding area fraction for CNT/PC nanocomposites with (a) 0.5 wt% MWNTs NC7000, (b) 2 wt% MWNTs NC7000, (c) 0.5 wt% SWNTs Tuball, (d) 2 wt% SWNTs Tuball.

The better dispersion of MWNTs is likely due to their shorter length, whereas the longer SWNTs require higher energy input and shear mixing force to achieve dispersion.
It was also found that the intrinsic molecular structure of the matrix plays an important role on the degree of dispersion. A better dispersion of the nanofillers was in fact observed in the PC matrix, that exhibits an amorphous structure, thus a relatively low viscosity. On the other hand, the higher viscosity ensuing from the semi-crystalline structure of the PBT matrix decreases the dispersibility of the CNTs.
These observations emphasize the limitations represented by the CNTs dispersion and their compatibility with the hosting matrices. Indeed, the CNT agglomerates turn out not to be well-impregnated with the polymer matrix, but they are just surrounded by the polymer; no CNT/matrix interfaces are available for the load transfer. In conclusion, the CNT agglomerates act more as defect points/holes other than reinforcement.

5.3 SEM Analysis

In addition, scanning electron microscopy (SEM) analyses were conducted on cryo-fractured surfaces of nanocomposites cross-sections through the Ultra Plus Field Emission Gun Scanning Electron Microscope (FEG-SEM, Carl-Zeiss AG) in order to investigate the dispersion of the individual CNTs in the hosting matrices.

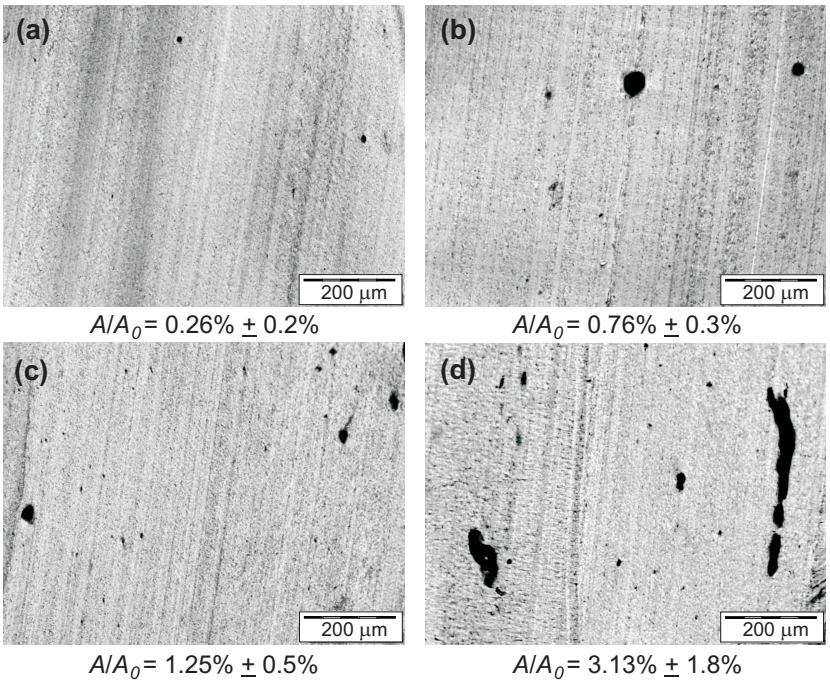

Figure 5.6: Light microscopy images and corresponding area fraction for CNT/PBT nanocomposites with (a) 0.5 wt% MWNTs NC7000, (b) 2 wt% MWNTs NC7000, (c) 0.5 wt% SWNTs Tuball, (d) 2 wt% SWNTs Tuball.

5.3.1 Samples preparation and method

SEM analysis can be conducted on cryo-fractured surfaces to provide information on individual CNTs dispersion and orientation. It should be noted that SEM analysis is dependent on the compositional and topographical contrast of the materials investigated. Although SEM micrographs are able to confirm the presence of a CNT network structure, the topological contrast of a fracture surface makes quantification of CNT dispersion via image processing unfeasible. The qualitative interpretation of SEM images is therefore subjective and a reasonable number of images is required to deduce the CNT dispersion of the bulk material.
SEM specimen requires a conductive surface and a path to ground. Specimen preparation for polymers typically involves fracturing a larger specimen to attain the suitable dimensions to fit into the vacuum chamber of a SEM. This is followed by the application of a conductive coating to allow electron transmission, to minimize radiation damage and to avoid charging of the specimen. Coatings can be applied with gold, platinum or carbon. The coating thickness should be minimal as a thick coating layer results in a granular and cracked appearance.
In the present work the composite strands were cryo-fractured in liquid nitrogen and the surfaces were covered with 3 nm Platinum. For Epoxy, PBT and PC composites the pressed strips were broken transversely to the longest side. PP composites were broken along the longest side of the strip.

5.3.2 Images investigation

In the SEM images, the conductive CNT are usually visible as light grey lines against the dark grey background/polymer matrix. A qualitative interpretation of the dispersion and distribution of the CNTs in the surrounding matrix can be given.
Fig.5.7 shows a set of representative SEM images of the MWNT/epoxy composite cross sections. SEM analysis confirm a better individual CNT dispersion in epoxy when the functionalization treatment is performed (see Fig.5.7b), while an area with a higher concentration of CNTs (agglomerates) is visible in Fig.5.7a for the nanocomposite with non-well dispersed CNTs.
For the MWNT/PP nanocomposites, it is possible to observe the CNTs only in some areas, due to the presence of the expected large talc particles. The PP polymer is indeed an impact-filled polymer modified with talc nanoparticles, which are clearly visible in the SEM images (Fig.5.8 and Fig.5.9).
In Fig.5.10 and 5.11 some of the SEM images for the PC and PBT nanocomposites are shown, respectively. The longer SWNTs are clearly visible in both the matrices with respect to the shorter MWNTs. The high density of the nanotubes in the nanocomposites with a CNT weight fraction of 2% is also remarkable.
Although light microscopy showed CNT agglomerates in all samples, a good nanodispersion and distribution of the remaining individual CNTs can be qualitatively observed in all matrices, ensuring a beneficial effect on the mechanical properties of the nanocomposites.

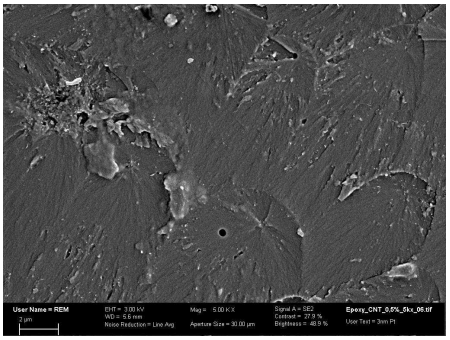

(a) *Pristine CNT/epoxy composite prepared via ultrasonic horn.*

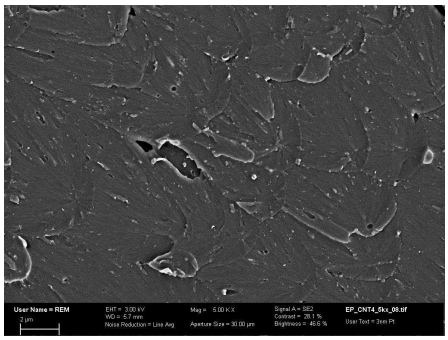

(b) *Amino-functionalized CNT/epoxy composite prepared using ultrasonic horn.*

Figure 5.7: SEM images of the cryofractured 0.5 wt% CNT/Epoxy nanocomposite samples prepared with different techniques.

5.4 TEM analysis on the CNT length distribution

Finally, the morphology of the nanotubes in the fabricated nanocomposites with SWNTs and MWNTs was acquired via transmission electron microscopy (TEM).
CNTs may generally show some damage or shortening effects due to the fabrication process that can significantly affect the resulting mechanical properties of the nanocomposite. A reduction in the aspect ratio of the CNTs often causes a decrease of the elastic modulus and tensile strength of the final materials. Experimental data collected on the CNTs length can also be used for the modeling of the nanocomposite introducing the actual length distribution

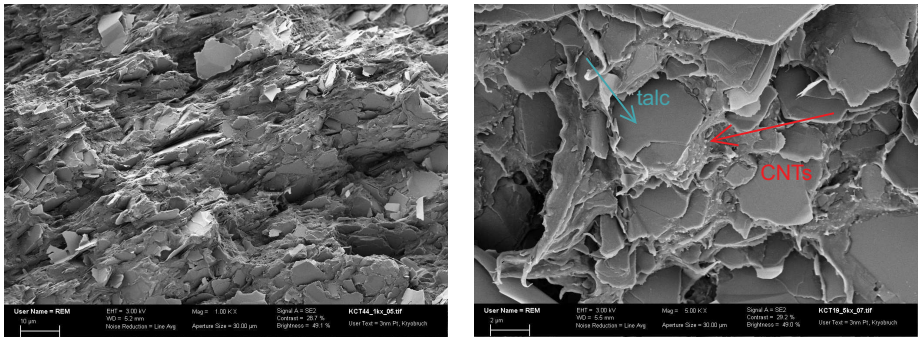

(a) (b)

Figure 5.8: SEM images of the cryofractured 0.5 wt% MWNT/PP nanocomposite samples at different magnitudes.

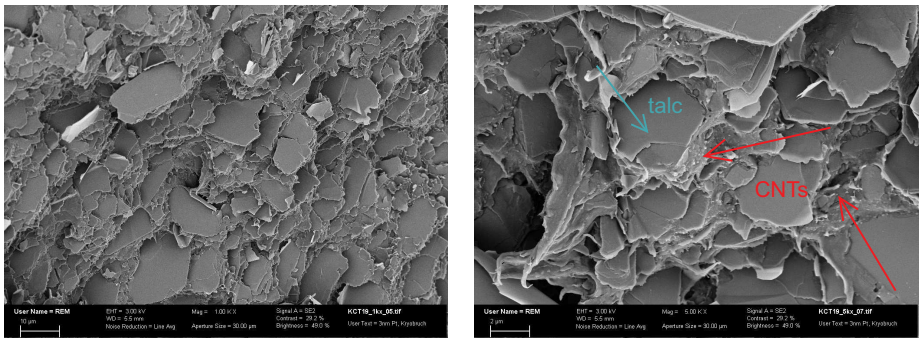

(a) (b)

Figure 5.9: SEM images of the cryofractured 5 wt% MWNT/PP nanocomposite samples at different magnitudes.

of the nanofiller as a model parameter.

5.4.1 Samples preparation and method

To estimate the CNT length distribution, small pieces of 0.07g of the melt mixed polycarbonate (PC) nanocomposite samples were dissolved in 10 ml chloroform overnight at room temperature [49]. The dispersions were afterwards treated for 3 min in an ultrasonic bath.
For the TEM investigations a drop of the freshly prepared dispersion with 0.1 g CNT/l, was placed on a TEM grid with a carbon coating and dried at air. In the TEM images collected with a Libra120 (Carl Zeiss GmbH) the nanotube lengths were measured on approximately 200 particles applying the software SCANDIUM 5.1 (Olympus Soft Imaging Solutions GmbH) using the full visible length of each separated nanotube not touching the edge of the image by applying the polyline function.
To quantify the nanotubes length distribution, the data were collected in histograms in which the characteristic parameters x_{10}, x_{50}, and x_{90} – that indicate the CNT lengths whose frequency is not greater than 10%, 50%, and 90% – were estimated.
A probability density function was adopted to fit the data, namely, the Generalized Extreme

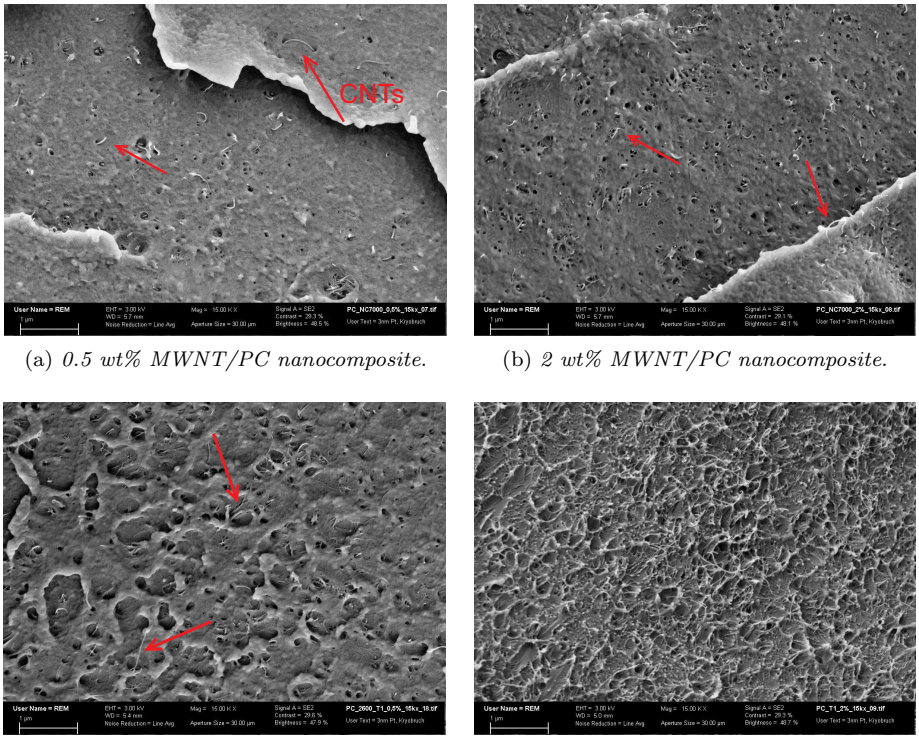

(a) *0.5 wt% MWNT/PC nanocomposite.* (b) *2 wt% MWNT/PC nanocomposite.*

(c) *0.5 wt% SWNT/PC nanocomposite.* (d) *2 wt% SWNT/PC nanocomposite.*

Figure 5.10: SEM images of the cryofractured PC nanocomposite samples.

Value (GEV) density function:

$$f(x;\mu,\sigma,\xi) = \frac{1}{\sigma}\left[1+\xi\left(\frac{x-\mu}{\sigma}\right)\right]^{(-1/\xi)-1} \exp\left\{-\left[1+\xi\left(\frac{x-\mu}{\sigma}\right)\right]^{-1/\xi}\right\} \tag{5.2}$$

where μ is the mean value of the CNT length data, σ is the standard deviation and ξ id the shape parameter.

5.4.2 CNT length distribution and results

In the TEM images (see Figures 5.12 and 5.13), a good individualization into single nanotubes is visible indicating that the chosen chloroform is a good solvent for PC.
From a qualitative analysis of the TEM images it appears that: (i) SWNTs Tuball are indeed longer than MWNTs NC7000, (ii) the shape of the SWNTs is more elongated and straight whereas the MWNTs are more curled and wavy.
In Fig. 5.14 the actual CNTs length distributions are reported for both the two types of CNTs. This morphological analysis led to a key consideration. Indeed, the histograms reveal an important CNT shortening effect due to the fabrication treatments that results in a large range of variability of the CNT length within the obtained composites. The aspect ratio of the CNTs cannot be considered to be constant within the nanocomposites. Hence, the GEV distribution law was employed to fit the data, via identification of three parameters, namely, the mean value of the CNT length data μ, the standard deviation σ, and the shape parameter ξ.

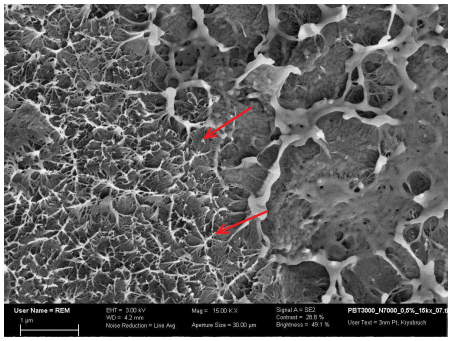

(a) *0.5 wt% MWNT/PBT nanocomposite.*

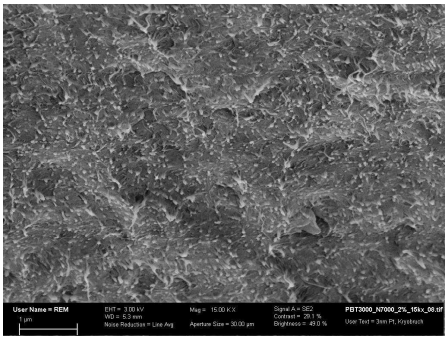

(b) *2 wt% MWNT/PBT nanocomposite.*

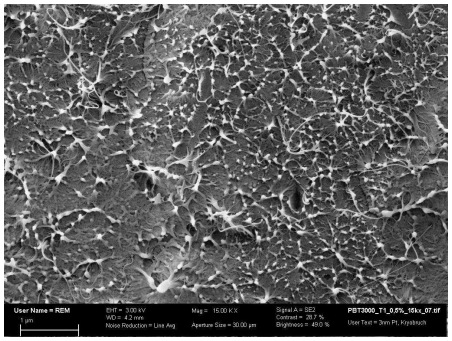

(c) *0.5 wt% SWNT/PBT nanocomposite.*

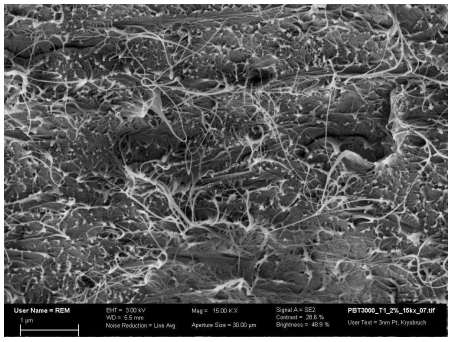

(d) *2 wt% SWNT/PBT nanocomposite.*

Figure 5.11: SEM images of the cryofractured PBT nanocomposite samples.

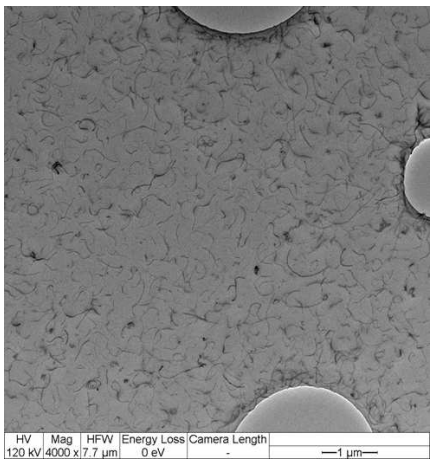

(a)

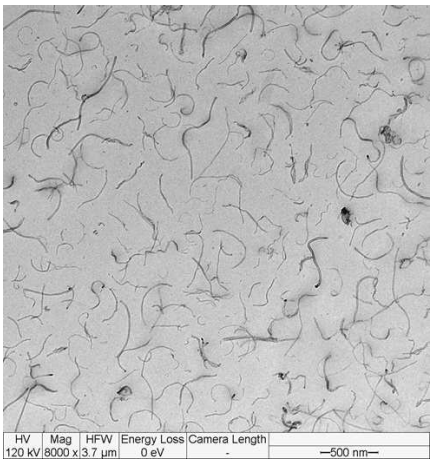

(b)

Figure 5.12: TEM images of the MWNTs (NC7000) after having dissolved the CNT/PC nanocomposite in chloroform.

By fitting the data, the best MWNTs length distribution was found for the parameters $\mu = 338.16$, $\sigma = 156.56$, and $\xi = 0.044$; while for the SWNTs the obtained parameters were $\mu = 407.17$, $\sigma = 202.59$, and $\xi = 0.107$.
The MWNTs average length was found to be 404 nm, which is half of the initial length, according by the producer (initial length: 1 μm). The most drastic shortening is the one of

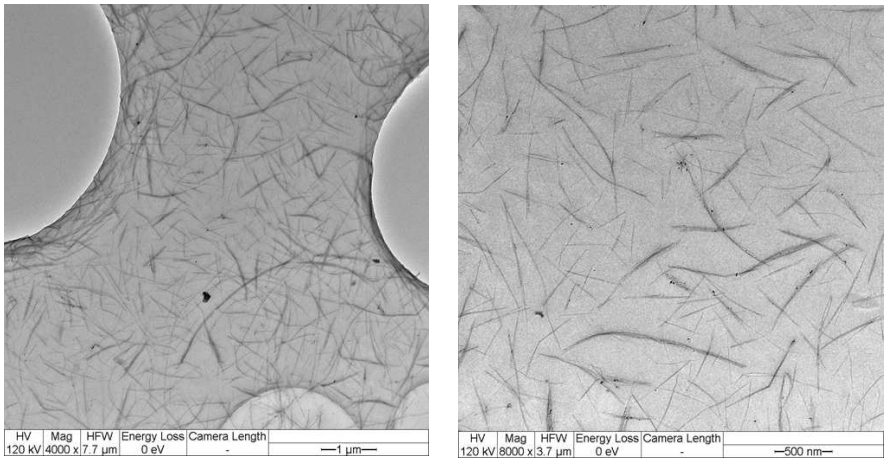

(a) (b)

Figure 5.13: TEM images of the SWNTs (Tuball) after having dissolved the CNT/PC nanocomposite in chloroform.

the SWNTs, that have an initial length higher than 5 μm, but their average length after the processing is reported to be 499 nm.

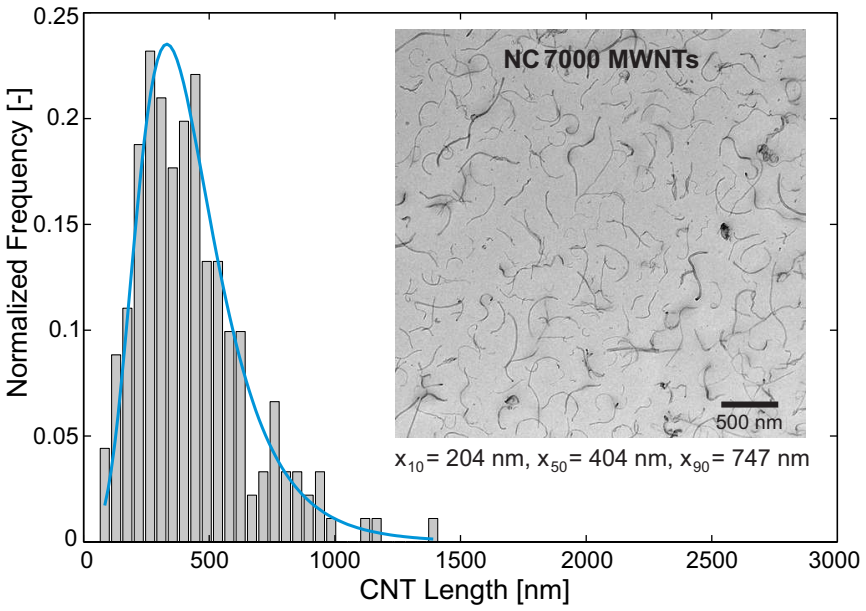

(a) MWNTs length distribution

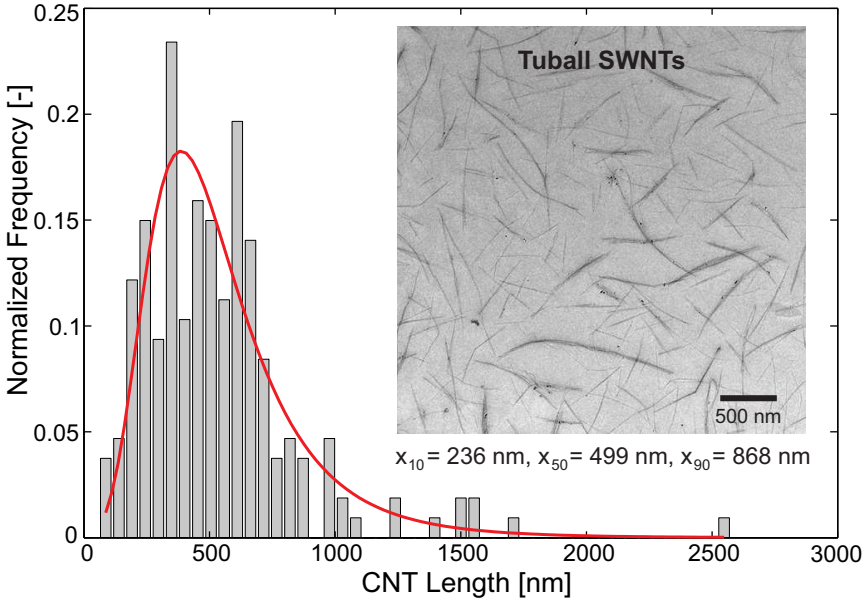

(b) SWNTs length distribution

Figure 5.14: CNTs length distributions within the hosting matrix after the fabrication process together with the TEM images of the CNT dispersions. The solid curves in the histograms represent the GEV distribution law matching the experimental data, where the frequency of every CNT length is normalized with respect to the area below the GEV density function.

Chapter 6

Mechanical Characterization of CNT Nanocomposites

6.1 Introduction

Several CNT nanocomposite samples were prepared using different polymers, CNT aspect ratios and weight fractions.
In this chapter the mechanical properties of the nanocomposites are explored and discussed. This part of the experimental work is mainly focused on the investigation of the mechanical characteristics of the nanocomposites – such as the Young modulus, tensile strength and ultimate strain at break – obtained through a campaign of monotonic tensile tests. Some of the most common micromechanical models for composites materials are also employed to compare elastic moduli predictions with the experimental data. Some ideal assumptions of the theoretical models on the nanocomposite microstructure are discussed, aiming at finding a relationship between the macroscopic response and the actual morphological features of the materials.
The acquired experimental data also provide information on the nonlinear visco-elasto-plastic response, as shown in different nanocomposites stress-strain curves. A further study is also carried out on the hysteretic behavior observed through cyclic tensile tests, by estimating the nanocomposites damping capacity.

6.1.1 Tensile tests: specimens and method

To compare the mechanical properties of the nanocomposites, monotonic tensile tests and cyclic tensile tests were carried out by a Zwick/Roell Universal Testing Machine (Zwick GmbH & Co. KG, Germany). Specimen shapes, test speeds and method of results determination for the tensile characteristic values (tensile Young modulus, ultimate tensile strength and ultimate strain at break) were selected and measured according to ISO 527-1 and -2. The dog-bone nanocomposite specimens were shaped as the specimen type 5B given in ISO 527-2 and showed in Fig.6.1. The overall length of the specimens was measured to be 50 mm in length with gage length of 12 mm, and cross section in the narrow portion of 2×4 mm^2.
A pre-load of 0.25 N was initially applied in every test and all the specimens were initially

tested at a test speed of 0.2 mm/min in the deformation range going from 0% up to 0.5% in order to estimate the elastic moduli of the materials.
The monotonic tensile tests to failure were carried out at different displacement rates by considering the ductility of the polymer matrices of each different nanocomposite. In fact, some polymers adopted in this study can withstand large deformation before undergoing failure, such as the polypropylene (PP) thermoplastic polymer that can reach an elongation larger than 100% before the break, while others show a faster degradation and can break at an elongation of 10%.
The displacement rate selected for CNT/PP nanocomposites was 20 mm/min, while for the two engineering thermoplastics, PC and PBT respectively, and for epoxy nanocomposites, the displacement rate was set to 2 mm/min, till the break of the samples.
The cyclic tensile tests for the PP nanocomposites were performed at a displacement rate of 5 mm/min by increasing the deformation of 1% at each loading process, up to a maximum deformation o 6% in the last cycle, which is before the occurring of the material yielding. For the PC and PBT nanocomposites the selected test speed was 2 mm/min by increasing the deformation of 0.5% at each loading process. For the engineering thermoplastic nanocomposites (PC and PBT) the maximum deformation reached in the cyclic test was of 1.5% after three loading/unloading cycles. Finally, for the epoxy nanocomposites the displacement rate was set at 0.2 mm/min by increasing the deformation of 0.5% at each loading cycle till a maximum strain of 5%, when the nanocomposite was not undergoing failure before that strain value.
All the tests were repeated at least 5 times for each nanocomposite type and the resulting curves are obtained by an average procedure.

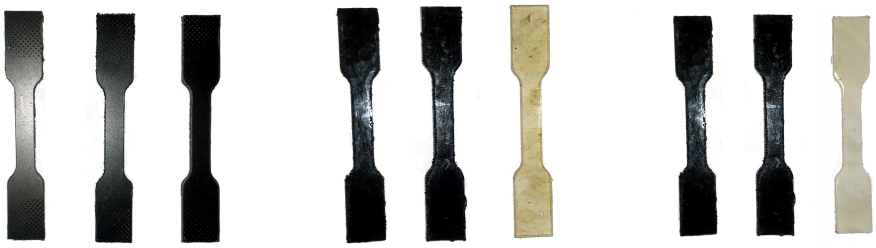

(a) *Pure PP and CNT/PP nanocomposite dog-bone specimens.*

(b) *Pure PC and CNT/PC nanocomposite dog-bone specimens.*

(c) *Pure PBT and CNT/PBT nanocomposite dog-bone specimens.*

Figure 6.1: Some of the CNT/polymer nanocomposite samples prepared for tensile tests.

6.1.2 Monotonic tensile test results

Monotonic tensile tests were carried out for nanocomposites with three different thermoplastic polymer matrices, namely polypropylene (PP), polycarbonate (PC), and polybutylene terephthalate (PBT).
Figures 6.3, 6.4 and 6.5 show stress-strain curves obtained for the nanocomposites with different nanotube weight percentages. As expected, the macroscopic mechanical properties are strongly affected by the CNTs aspect ratio, dispersion and weight fraction.
In Fig. 6.3, the PP soft polymer can withstand high strains before reaching its relatively low ultimate tensile strength (16.5 MPa)as PP does not belong to the engineering polymers class

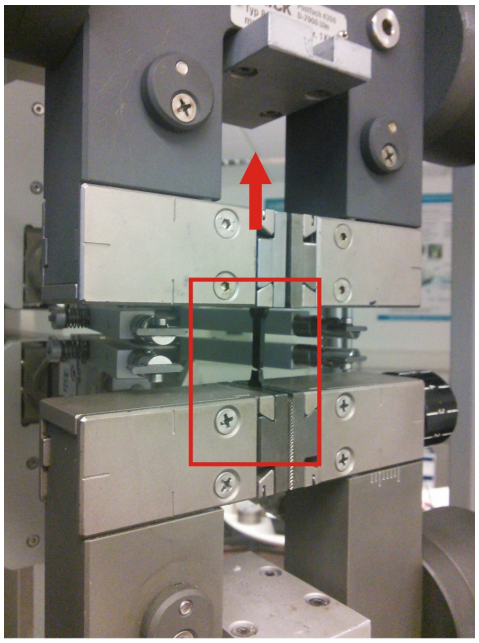

Figure 6.2: Zwick/Roell testing machine for tensile tests of dog-bone specimens.

for structural applications. The increase in the CNT weight fractions (from 0.5% up to 5%) leads to appreciable improvements of the Young modulus and ultimate tensile strength. For instance, a 25% modulus increase was recorded for 5 wt% of MWNTs in PP matrix (see Table 6.1). A ductility loss is also observed due to the restriction of the polymer chains mobility in the nanocomposites. Consequently, the ultimate strain at break for PP nanocomposites reduces by increasing the CNT weight fraction.

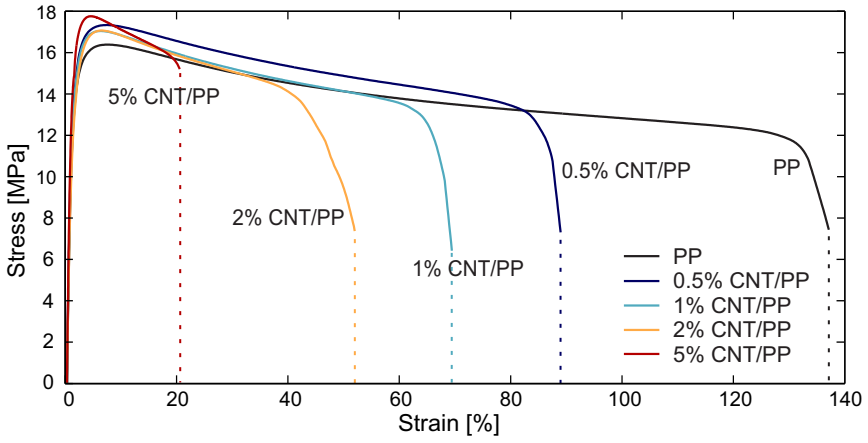

Figure 6.3: Monotonic tensile tests for PP and PP nanocomposites with several weight fractions of NC7000 MWNTs.

The same trend is also observed for the PC and PBT nanocomposites in Figs. 6.4 and 6.5. The neat PC and PBT thermoplastic polymers can reach a maximum elongation at break of almost 42% and 11%, respectively, with an ultimate tensile strength close to 58 MPa for both

Table 6.1: Experimentally obtained PP nanocomposites elastic moduli.

CNT Type	CNT weight fract. [%]	CNT volume fract. [%]	Young Modulus [GPa]
-	0	0	1.453
MWNT	0.5	0.3	1.535
MWNT	1	0.6	1.534
MWNT	2	1.3	1.585
MWNT	5	3.3	1.808

matrices. The neat PC material reveals a neck in the tensile stress-strain curve at a strain of 7%, after which the polymer keeps elongating till break. This behavior is typical for the polycarbonate polymer [23]. On the other hand, all PC nanocomposites undergo failure at strains lower than 7%, where the neck of the neat polymer occurs. This large reduction in the elongation at break is justified by a significant increase in the stiffness of the nanocomposites compared to the neat polymer.
In Fig. 6.5, PBT nanocomposites show a clearer transition from the elastic to inelastic phase, with a relevant increase in the elastic moduli of all the CNT/PBT nanocomposites compared to the pure PBT polymer.
Moreover, the nanocomposites prepared with the two engineering thermoplastic polymers are different not only for the nanotubes content, but also for the type of nanotubes employed. High aspect ratio SWNTs nanocomposites and low aspect ratio MWNTs nanocomposites are tested under the same loading conditions in order to investigate the effects of the CNTs length and diameter on the macroscopic mechanical behavior of the polymer composites.
The high-aspect ratio SWNTs lead to a larger contact surface area between the nanotubes and polymer chains and yield higher elastic moduli. In Tables 6.2 and 6.3, a 32% increase of the Young modulus for the 2 wt% SWNT/PC nanocomposite and a 24% for the 2 wt% SWNT/PBT nanocomposite are reported with respect to the neat polymers. For the MWNT nanocomposites, a maximum increase is reported for a CNT weight fraction of 0.5%, and the Young modulus augmentation is the order of 14% and 12% for the PC and PBT composites, respectively.

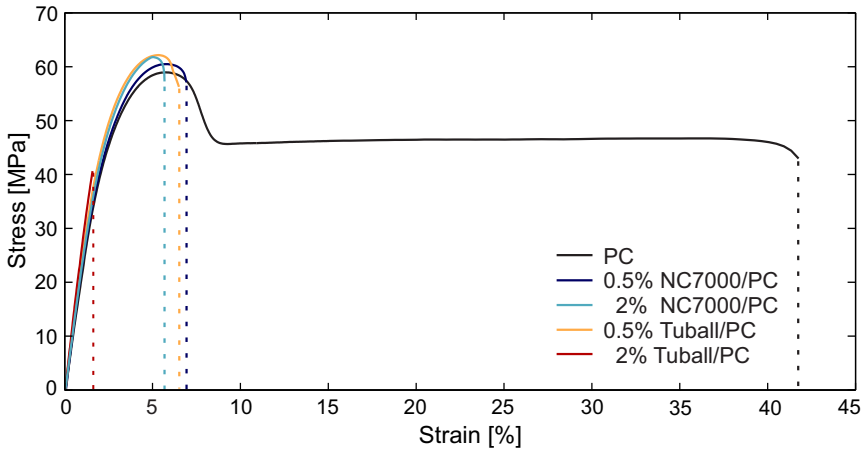

Figure 6.4: Monotonic tensile tests for PC and PC nanocomposites with 0.5% and 2% weight fractions of MWNTs NC7000 and SWNTs Tuball, respectively.

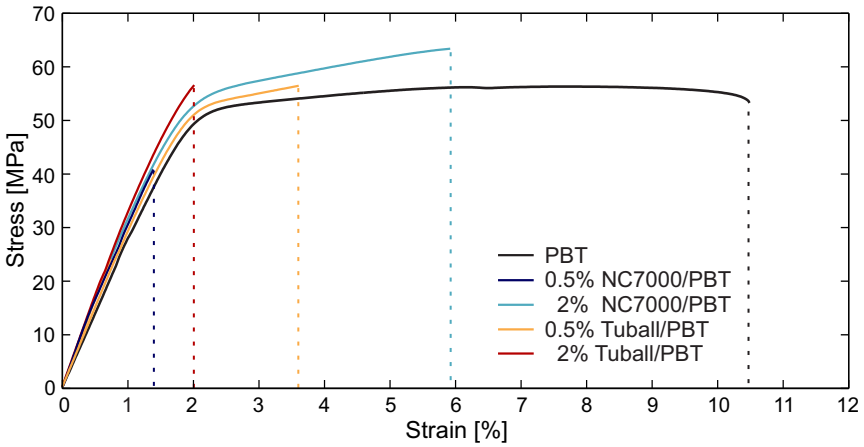

Figure 6.5: Monotonic tensile tests for PBT and PBT nanocomposites with 0.5% and 2% weight fractions of MWNTs NC7000 and SWNTs Tuball, respectively.

Table 6.2: Experimentally obtained PC nanocomposites elastic moduli.

CNT Type	CNT weight fract. [%]	CNT volume fract. [%]	Young Modulus [GPa]
-	0	0	2.354
MWNT	0.5	0.34	2.729
MWNT	2	1.38	2.683
SWNT	0.5	0.33	2.670
SWNT	2	1.34	3.144

It is worth noting that in all three polymer nanocomposites, the improvement in the mechanical properties is not proportional to the nanotube fractions embedded in the matrices (Fig.6.6). After a first increase of the elastic modulus with a small nanotube content of 0.5 wt% , the positive effect of the MWNTs on the elastic modulus is hindered by the degree of CNT dispersion in the matrices combined with the curviness of the MWNTs. Due to the low aspect ratio of the MWNTs and their curled shape, their effective length is drastically reduced and the CNT agglomerates act more as holes and defect points.
On the other hand, although SWNTs nanocomposites show through the micrographs a worse agglomeration state, they perfectly act as reinforcement nanofillers due to their high aspect ratio and their lengthened shape, thus providing more interfacial area for the load transfer. This confirms that not all CNTs represent a proper reinforcement nanofiller for polymer matrices. Several factors contribute differently to the resulting mechanical behavior of the

Table 6.3: Experimentally obtained PBT nanocomposites elastic moduli.

CNT Type	CNT weight fract. [%]	CNT volume fract. [%]	Young Modulus [GPa]
-	0	0	2.661
MWNT	0.5	0.37	3.049
MWNT	2	1.5	3.020
SWNT	0.5	0.36	2.927
SWNT	2	1.46	3.313

nanocomposites, namely, the CNT dispersion and agglomeration state, CNT/matrix interactions at the available interfacial surface area, CNT weight fraction, aspect ratio and curviness.

6.2 Theoretical predictions of the nanocomposites Young moduli

In conjunction with experimental studies, a prediction of the nanocomposites elastic properties is provided by some well-known micromechanical theories. Indeed, the most common approaches employed to estimate the elastic moduli of nanocomposites rely on the use of micromechanical models, finite element analysis (FEA) and molecular dynamic (MD) simulation. Although the FEA and MD approaches lead to a detailed modeling of the nanocomposite material, theoretical models can still provide a reliable constitutive response with the advantage of achieving a closed-form solution with less computational effort.
Among the models, already extensively employed for traditional fiber composite systems and adjusted for nanocomposite materials, it is worth to mention (i) the rule of mixture, from the Voigt model, (ii) the Halpin-Tsai model derived from the self-consistent method, and (iii) the already introduced Eshelby and Mori-Tanaka theory.
The rule of mixture represents an easy approach to estimate Young modulus of unidirectional composite materials. It provides a parallel coupling formula which gives the average elastic longitudinal modulus E_L of the composite as:

$$E_L = (1 - \phi_C)E_M + \phi_C E_C \,, \tag{6.1}$$

where ϕ_C is the volume fraction of the nanofiller, and E_M and E_C represent the elastic moduli of the matrix and the nanofiller, respectively.
Reuss applied the series coupling formula to get a similar expression for the average transverse modulus E_T of the composite material, thus providing the inverse rule of mixture:

$$\frac{1}{E_T} = \frac{(1 - \phi_C)}{E_M} + \frac{\phi_C}{E_C}. \tag{6.2}$$

A more effective theory is the one leading to the Halpin-Tsai model [37], based on the generalized self-consistent method which was initially developed by Hill [38] for traditional fiber composites. Later, successful efforts were undertaken to apply the Halpin-Tsai model to both aligned or randomly oriented CNT nanocomposites, by introducing orientation and shape factors that account for the geometry of the filler phase, as done in the work of Thostenson and Chou [90].
This two-phase model takes into account the volume fraction of the filler phase as well as the nanotube structure and geometry, by assuming that the outer nanotube wall alone acts as a solid fiber, supporting the loads applied. The aspect ratio of the nanofiller is also included as a model parameter. A drawback of the Halpin-Tsai model is that strong interfacial bonding between the filler and matrix is assumed, as well as a homogenous distribution of the filler in the matrix.
For randomly oriented CNT nanocomposites the following equation can be used [90]:

$$E = E_M \left[\frac{3}{8} \left(\frac{1 + 2\alpha h_L \phi_C}{1 - h_L \phi_C} \right) + \frac{5}{8} \left(\frac{1 + 2 h_T \phi_C}{1 - h_T \phi_C} \right) \right] \tag{6.3}$$

where

$$h_L = \frac{E_C/E_M - 1}{E_C/E_M + 2\alpha}, \qquad h_T = \frac{E_C/E_M - 1}{E_C/E_M + 2}, \tag{6.4}$$

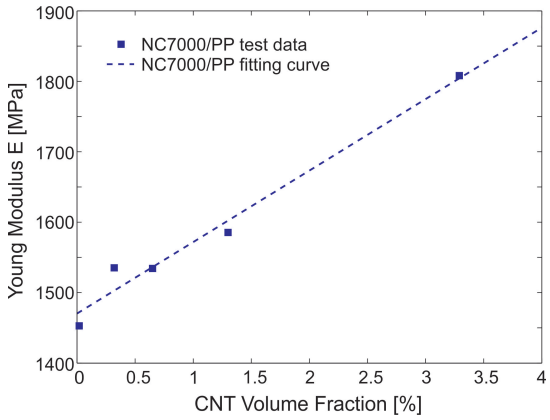

(a) *Pure PP and CNT/PP nanocomposite elastic moduli.*

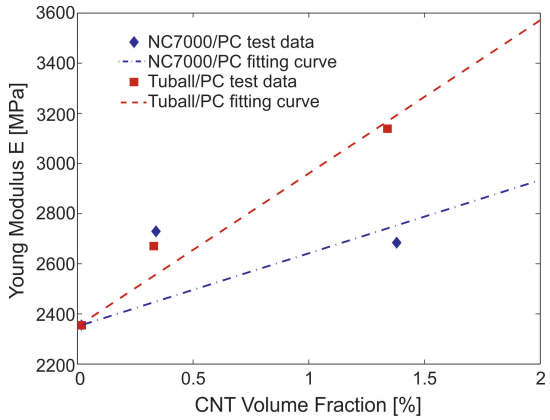

(b) *Pure PC and CNT/PC nanocomposite elastic moduli.*

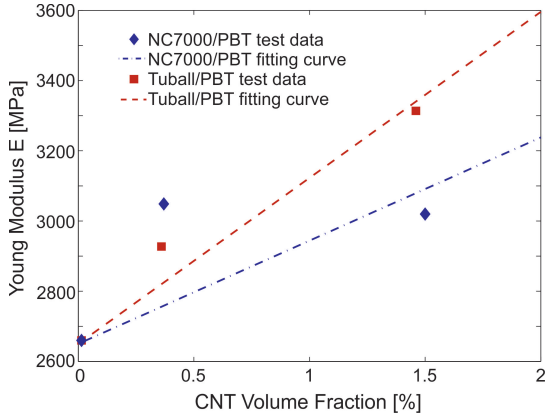

(c) *Pure PBT and CNT/PBT nanocomposite elastic moduli.*

Figure 6.6: Experimental averaged values for the Young Moduli of the nanocomposites varying with CNT volume fraction. The experimental data are obtained as he average of 5 repeated tensile tests for each kind of nanocomposites. The linear regressions of the data is also reported for each nanocomposite.

and the parameter α represents the aspect ratio of the CNTs L/D.
On the other hand, the Eshelby theory [21, 22] combined with the Mori-Tanaka approach [62] leads to a more accurate prediction of the nanocomposite mechanical properties, as documented in the literature [67]. The Mori-Tanaka model is based on the Eshelby equivalent inclusion method and the rule of mixture for the average stress and strain. Nanofillers are modeled as ellipsoidal inclusions, whose geometry is taken into account through the Eshelby tensor $\boldsymbol{S}$ [64]. A direct formulation of the Eshelby-Mori-Tanaka model for a two-phase material is provided by Benveniste [12]:

$$\boldsymbol{L} = \boldsymbol{L}_M + \phi_C \langle [\![\boldsymbol{L}]\!] : \boldsymbol{A} \rangle : (\phi_M \boldsymbol{I} + \phi_M \langle \boldsymbol{A} \rangle)^{-1} \tag{6.5}$$

where ϕ_C and ϕ_M are the inclusion and matrix volume fractions, respectively, $\boldsymbol{I}$ is the identity tensor, $\boldsymbol{L}_C$ and $\boldsymbol{L}_M$ are the stiffness tensor for the inclusions and the matrix, and $[\![\boldsymbol{L}]\!] = \boldsymbol{L}_C - \boldsymbol{L}_M$. The tensor $\boldsymbol{A}$ represents the dilute mechanical strain concentration tensor for the inclusions and is given as:

$$\boldsymbol{A} = \left[\boldsymbol{I} + \boldsymbol{S} : (\boldsymbol{L}_M)^{-1} : [\![\boldsymbol{L}]\!]\right]^{-1}. \tag{6.6}$$

The expression of the Eshelby tensor $\boldsymbol{S}$ is given by Eshleby and Mura [64], and all the terms enclosed with angle brackets represent average value of the terms over all the orientation defined by the transformation from the local inclusion coordinates to the global coordinates of the nanocomposite material domain.
According to the theory presented in Chap. 2, a more efficient and compact expression is provided for the effective elastic tensor $\boldsymbol{L}$:

$$\boldsymbol{L} = \boldsymbol{L}_M + \phi_C \langle \bar{\boldsymbol{N}} \rangle \tag{6.7}$$

where

$$\boldsymbol{N} = [\![\boldsymbol{L}]\!] : \left(\boldsymbol{I} + \phi_M \boldsymbol{S} : \boldsymbol{L}_M^{-1} : [\![\boldsymbol{L}]\!]\right)^{-1}. \tag{6.8}$$

The advantage of Eq. 6.7 is the less computational effort necessary to determine the equivalent elastic tensor, since only the $\bar{\boldsymbol{N}}$ tensor has to be averaged out over all the possible orientations of the inclusions.
For randomly oriented nanocomposites, the $\boldsymbol{N}$ tensor must first be transformed in order to be expressed in the global coordinates

$$\bar{\boldsymbol{N}}_{ijkl} = c_{ip} c_{jq} c_{kr} c_{ls} \boldsymbol{N}_{pqrs} \tag{6.9}$$

and subsequently it can be averaged out over all the directions given by the Euler angles:

$$\langle \bar{\boldsymbol{N}} \rangle = \frac{1}{8\pi^2} \int_0^{2\pi} \int_0^{\pi} \int_0^{2\pi} \bar{\boldsymbol{N}} \sin\theta \, d\varphi \, d\theta \, d\beta. \tag{6.10}$$

In the present work, the Halpin-Tsai model and the Eshelby-Mori-Tanaka model are employed and compared to predict the elastic constants for the randomly oriented CNT nanocomposites. The results are reported in Fig.6.7 and a comparison with the experimental data is provided.
For the computation, Eq. 6.3 and Eq. 6.7 were adopted by considering for the aspect ratios of MWNTs and SWNTs the nominal values provided by the producers. Both the methods deliver a not negligible error in the prediction of the elastic moduli, especially for increasing values of the CNT contents in nanocomposites. In fact, notwithstanding the extensive efforts spent on constitutive models, these theories generally tend to overestimate the effective

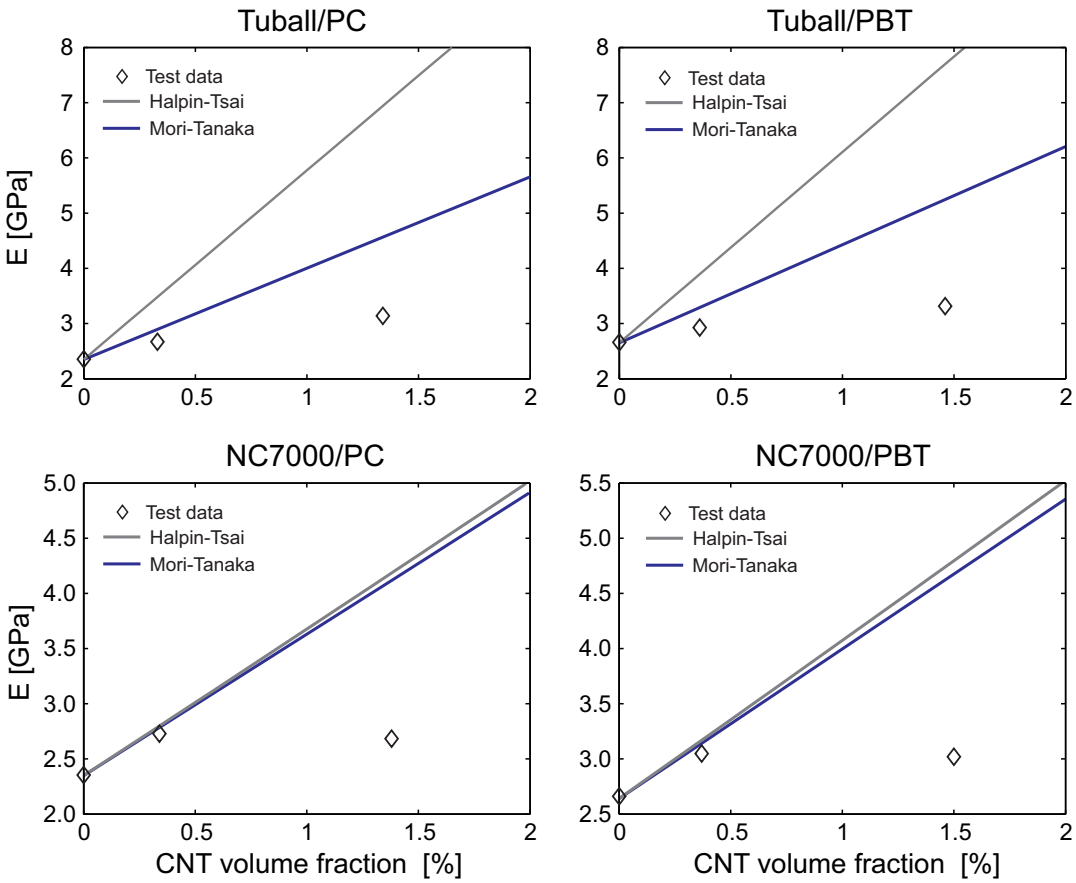

Figure 6.7: Predictions of the effective elastic moluli of the PC and PBT nanocomposites compared with the experimental data.

elastic properties of the nanocomposites when they are modeled by introducing substantial simplifications of the nanocomposite morphological structure.

Up to date, classical micromechanical approaches still lack to account for important microstructural aspects, while they ideally assume perfectly dispersed CNTs, perfect CNT/matrix interfaces and do not account for the CNT agglomeration states, CNT curviness or the non-uniform distribution of the CNT aspect ratios inside the nanocomposites. In particular, the CNT dispersion is a key factor affecting the final resulting mechanical properties of the nanocomposite. When the CNT content is lower and a better CNT dispersion is achieved in the material, a better agreement between the theoretical predictions and the experimental data is found.

To sum up, the results highlight the complexity of the CNT/polymer materials, which are often non-uniform and anisotropous materials. All the factors acting together in the composites, such as CNT aspect ratio, weight fraction, dispersion, random distribution and polymer structure, are all responsible of the resulting macroscopic response. In Chapter 8, some modeling enhancements are proposed to overcome these limitations.

6.3 Cyclic tensile test results

A campaign of cyclic tensile tests was also conducted to observe hysteresis and determine the damping capacity of the nanocomposites. The cyclic tensile tests were carried out at increasing cycle strain amplitudes by adopting the test conditions described in section 6.1.2. In addition to the three thermoplastic nanocomposites, some MWNT/epoxy composites samples were also tested in a preliminary study. The results are here reported since they pointed out some of the most critical issues about the manufacturing processes that influence the morphological and mechanical properties of nanocomposites.

6.3.1 Hysteretic behavior of CNT/epoxy nanocomposites: a preliminary study

Cyclic tensile tests were performed for the three epoxy nanocomposites with a low MWNTs content equal to 0.5 wt%.
First, the cyclic stress-strain curves of the three nanocomposite materials are shown in Fig.6.8 comparing the agglomeration state in each specimen (see Fig6.9). As shown in Fig. 6.9c, the covalent amino-functionalization adopted for the MWNTs was effective to achieve good dispersion and uniform distribution of the CNTs in the nanocomposite sample due to the steric repulsions among the functional groups. The CNT disentaglement has a significant impact on the mechanical properties of the material, which is stiffer compared to the other nanocomposites. However, this increase in stiffness reflects also into an earlier fracture of the sample which becomes less ductile and dissipates less energy at low strain values. Indeed, the diamino functional groups, attached onto the surface of the MWNTs, are highly reactive with the oxirane rings in the epoxy resin. This results in stronger interfaces with a more difficult activation of the CNT/matrix interfacial slippage.
On the other hand, the effect of a stronger ultrasonication via the ultrasonic horn leads to a better mechanical response of the nanocomposites, without any loss in the damping capacity of the nanostructured materials. Indeed the arising of the stick-slip interfacial sliding, in the non-functionalized nanocomposites, is still dictated by the overcome of the interfacial van der Waals forces. On the contrary, the mild ultrasonication of the first nanocomposite (see Fig. 6.9a) is not effective to provide a good CNT dispersion, thus, affecting the mechanical properties of the sample that is characterized by the lowest elastic modulus among the three samples (see Table 6.4).
However, the neat epoxy resin exhibit a better mechanical response than all the nanocomposites. This finding highlighted many crucial issues related to the manufacturing process and the microstructural materials features. Indeed, not all types of carbon nanotubes can provide an improvement in the mechanical properties of the polymers. Furthermore, matrices with different stiffness interact differently with CNTs. If the stiffness of the epoxy polymer is very high, the interface interactions between carbon nanotubes and the surrounding epoxy is generally poor due to an alteration in the curing rate and in the cross-linking process, as discussed in some literature works [17, 58].
An epoxy resin characterized by a high stiffness has a high cross-linking degree, as it is in this specific case. If the CNTs are introduced in the molecular structure of the polymer the orderly arrangement of the polymer chains is modified and the material lose stiffness. The molecules of the polymer dispose around the CNTs, by creating a hole that embed the nanotube. This well explains why there is not enhancement in the elastic moduli of the prepared CNT/epoxy nanocomposites. The CNT functionalization generally represents a solution to this problem.

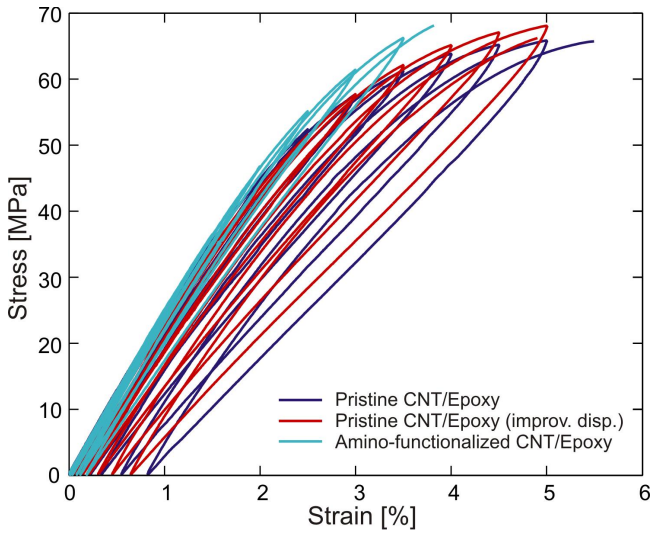

Figure 6.8: Comparison of hysteresis cycles for the three prepared CNT/epoxy nanocomposites

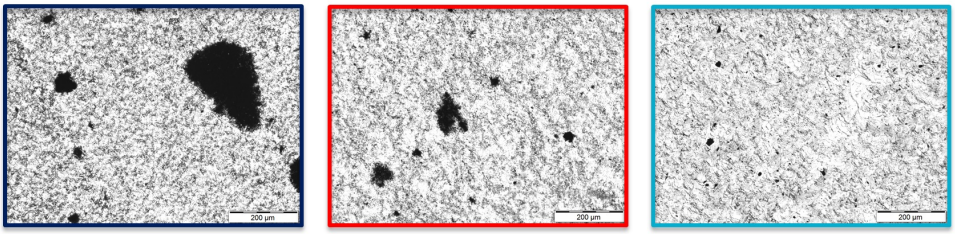

Figure 6.9: Micrographs of: (blu) pristine MWNT/epoxy composite prepared by adopting ultrasonic bath; (red) pristine MWNT/epoxy composite prepared via ultrasonic horn; (light blu) amino-functionalized MWNT/epoxy composite prepared using ultrasonic horn.

In Fig.6.10, the hysteresis loops of two CNT/epoxy nanocomposites are compared with those of the neat epoxy polymer. The nanocomposites do not show improvements in the mechanical properties with respect to the neat epoxy resin. However, it is interesting to notice that the damping capacity of the nanocomposites is significantly changed by the type of CNTs. In the case of the pristine CNT/epoxy samples the damping capacity is higher than the one observed in amino-functionalized CNT/epoxy samples. Indeed, due to weak van der Waals interaction forces at the raw CNT/matrix interfaces, the dissipative interfacial slippage can easily take place even at low strains (0.03%) in the pristine CNT/epoxy sample. On the contrary, the strengthened covalently-bonded interfaces in the functionalized CNT/epoxy composite do not allow for any sliding frictional motion, since larger strains and/or higher forces are required to overcome the interfacial shear strength (ISS) value. The amino-functionalized CNT/epoxy sample results in a stiffer material with narrow hysteresis loops.

6.3.2 Hysteretic behavior of CNT/thermoplastic nanocomposites

Cyclic tensile tests were conducted in the strain range from 0 to 6% for the soft PP nanocomposites, while the strain range explored for the stiffer PC and PBT nanocomposites was

Table 6.4: Experimentally obtained epoxy nanocomposites elastic moduli.

Material	Young Modulus [GPa]
Neat Epoxy	2.60
0.5 wt% MWNT/Epoxy	2.39
0.5 wt% MWNT/Epoxy (improv. disp.)	2.44
0.5 wt% Amino-MWNT/Epoxy	2.51

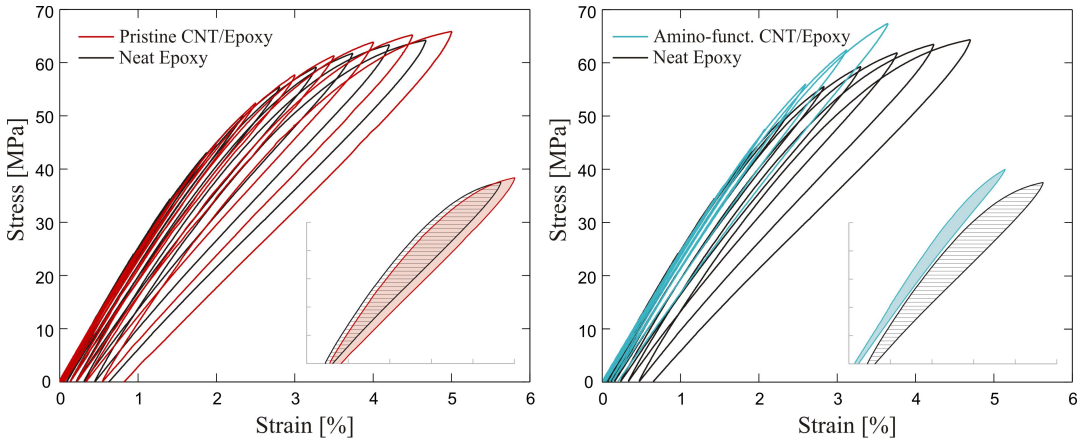

Figure 6.10: Cyclic tensile tests for (a) pristine MWNT/epoxy nanocomposite (b) amino-functionalized MWNT/epoxy nanocomposite.The hysteresis loops of the two CNT nanocomposites are compared with those of the neat epoxy sample.

spanned from 0 to 2% with three cycles, due to the low strain value at which the materials reach the ultimate tensile strength.
The specific damping capacity of the nanocomposites was estimated at each cycle as the ratio of the dissipated energy ΔW_D with respect to the elastic stored energy per cycle W_E.

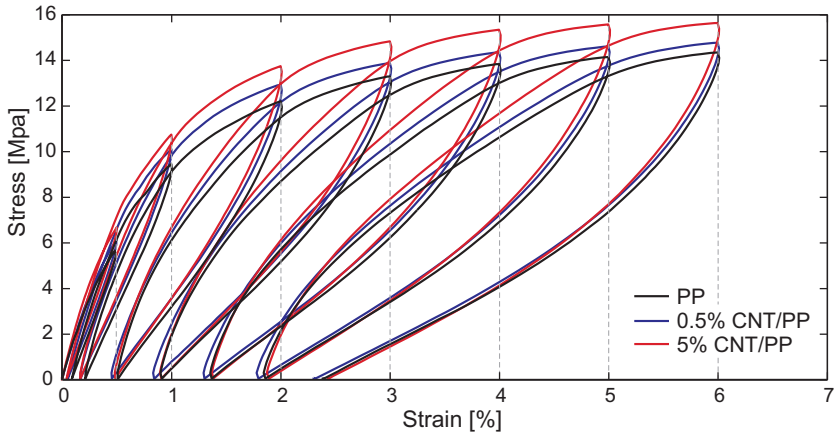

Figure 6.11: Cyclic tensile tests on PP and CNT/PP nanocomposites with maximum strain amplitude of 6% in the last cycle.

The PP polymer is a viscoelastic thermoplastic with pronounced viscous damping proper-

ties. Although the cycles shown in Fig.6.11 have a large enclosed area, the damping capacity of the PP nanocomposites is not higher than the one exhibited by the two engineering thermoplastic nanocomposites, because of he very low stress values that the propylene can withstand. Moreover, there is no significant increase in the damping properties when the CNTs are integrated into the polymer. In fact, the dissipated energy per cycle in MWNT/PP nanocomposites, with respect to that of the pure PP, increases because of the augmentation in stiffness of the composites, as it is possible to see in the loading branches. But, the unloading branches of both the neat polymer and nanocomposites are instead overlapped with the same slope. This trend indicates that the hysteresis observed in the nanocomposites is meanly affected by the viscous behavior of the polymer, which is predominant with respect to stick-slip dissipation phenomenon due to the CNTs.
An explanation of the phenomenon can be given by considering the PP polymer chains mobility. In soft matrices the polymer chains can slide each other much easier than the CNTs with the polymer chains. The shear stresses, needed to activate the stick-slip at the CNT/matrix interfaces, are probably higher than those necessary to activate the sliding motion in the polymer itself.
This behavior results in an augmentation of the dissipated energy per cycle, only because the elastic energy stored in the cycle is also increasing. As consequence, the ratio between the dissipated energy and the stored elastic energy yields to slight improvements of the damping capacity in the PP-nanocomposites.

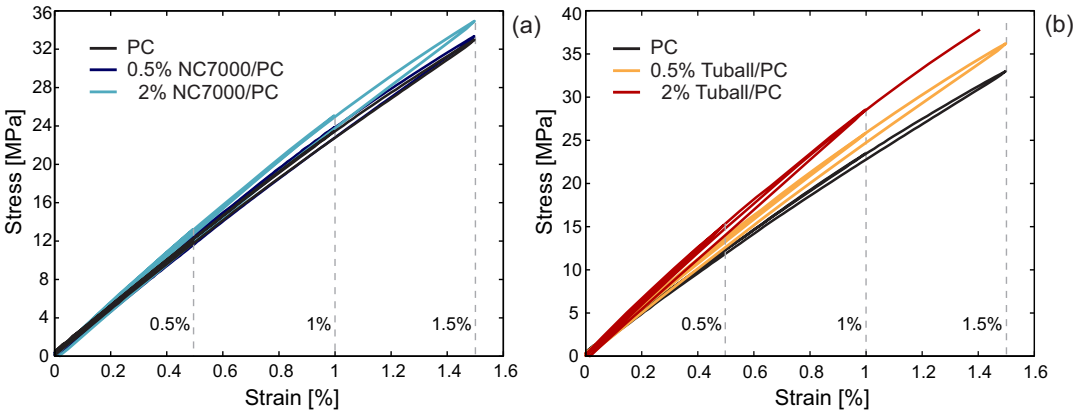

Figure 6.12: Cyclic tensile tests of for PC and PC nanocomposites with 0.5% and 2% weight fractions of MWNTs NC7000 (a) and SWNTs Tuball (b).

As expected, the two high-performance engineering polymers, PC and PBT, exhibit a higher stiffness compared to that of the PP. The very narrow cycles obtained for those materials in Fig.6.12 and 6.13 indicate the predominance of the elastic energy component, since the cycles mostly close itself and report only a very small irreversible deformation after the unloading phase. In this case, the damping capacity observed for PC and PBT nanocomposites can be ascribed to the internal hysteresis caused by the interfacial sliding motion between CNTs and polymer matrices. The interfacial shear stress needed to activate the stick-slip dissipation phenomenon is, then, lower than the stress necessary to make the polymer chains sliding one respect to the other. At the same time, the fatigue induced in the materials, combined with the stiffer behavior of the composites, arouses a premature failure at the last cycle in the nanocomposites that show higher Young modulus and brittleness, i.e., the SWNT nanocomposites.
In all cases with the exception of the 0.5 wt% MWNT/PC nanocomposite, there is an increase

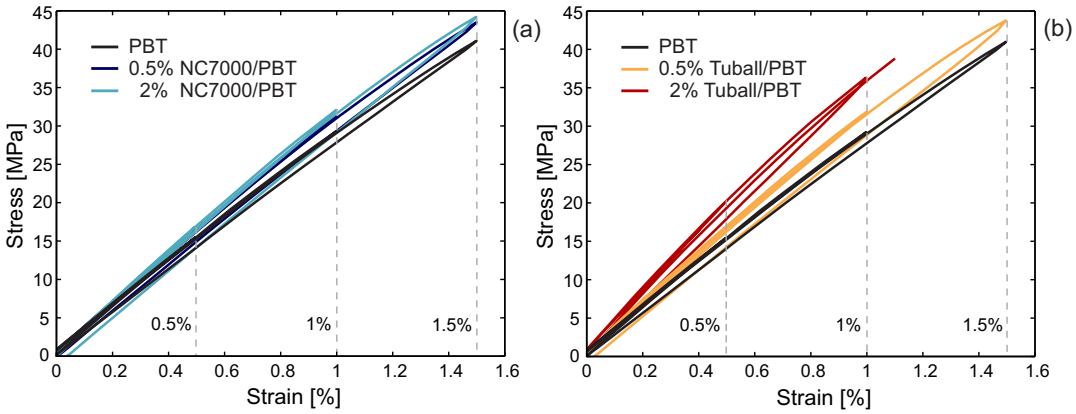

Figure 6.13: Cyclic tensile tests of for PBT and PBT nanocomposites with 0.5% and 2% weight fractions of MWNTs NC7000 (a) and SWNTs Tuball (b).

of the specific damping capacity for both MWNT and SWNT nanocomposites with respect to the neat polymers. The damping capacity increases with the strain amplitude of the cycles, which is a typical trend found for several materials with nonlinear response indicating the dependency of the damping properties on the strain amplitude which the material is subject to.

The specific damping capacity at the intermediate cycle - corresponding to a strain amplitude of 1% - is found to be 0.097 for the pure PC sample and 0.201 for the 2 wt% MWNT/PC composite, while it is 0.227 for the 0.5 wt% SWNT/PC composite. This corresponds to an increase in damping capacity of 106% by adding 2 wt% of MWNTs, and of 134% by adding 0.5 wt% of SWNTs to the neat PC matrix. Similarly, for the neat PBT thermoplastic polymer, the specific damping capacity is reported to be equal to 0.145, while it is 0.222 for 0.5 wt% MWNTs/PBT nanocomposite, and 0.223 for 0.5 wt% MWNT/PBT nanocomposite. Thus, the corresponding increase of the damping capacity, with respect to that of the neat PBT, is 53% with the addition of 0.5 wt% of MWNTs, and 54% with the addition of 0.5 wt% SWNTs.

Finally, it is possible to assess that also the dissipative properties, as well as the mechanical properties, of the nanocomposites are generally strongly influenced by the aspect ratio of the nanotubes, since also in this case nanocomposites with the high aspect ratio SWNTs are characterized by a better damping capacity than the composites with the low aspect ratio MWNTs. The drawback of the employed SWNTs is that a good degree of the CNT dispersion in the matrix is a challenge achievement. The formation of large CNT agglomerates causes stress concentration areas in the sample materials, hence, if higher contents of CNTs are employed, the nanocomposites undergo premature brittle failures.

Chapter 7

DMA Analysis: Nanocomposites Damping Capacity

7.1 Introduction

In order to achieve desired levels of damping capacity in innovative structures, a potential alternative to the use of auxiliary dampers is the exploitation of structural materials with inherent damping capability, such as the polymer nanocomposites. By embedding carbon nanotubes into polymers, the energy dissipation in the resulting nanocomposite can improve without compromising the lightness, and even enhanicing the effective stiffness and strength. After having observed hysteresis loops via cyclic tensile tests, a campaign of experimental DMA tests is envisioned in order to perform a more extended study on the damping capacity of CNT/polymer nanocomposites. The main mechanism that provides damping enhancement in these nanostructured materials is the interfacial stick-slip that occurs along the CNT/polymer interfaces when the a threshold value of the interfacial shear stress is reached. The strain amplitude associated to the interfacial shear strength can be estimated via the acquired DMA curves.
Since years, the Dynamic Mechanical Analysis (DMA) is a widely used technique in industry and it consists in applying small deformations or stresses to a sample in a cyclic manner. This allows to measure the materials response at variations of the stress, strain, temperature and frequency amplitudes. Significant information about the materials properties and structure can be provided, especially for polymers and composite materials. Indeed, DMA gives information about the rheology of the material, by measuring the viscoelastic properties. The rheology provides a relationship between the inner structure and the macroscopic properties of the nanocomposites, which is the key to the development for these new materials.
DMA tests are carried out by applying a periodic force or deformation in different modes and configurations of the samples (single cantilever, dual cantilever, three-point bending, tension, compression, shear and torsion). The data collected from the tests may be expressed in terms of a dynamic modulus, a dynamic loss modulus, and a mechanical damping term.
For an applied stress varying sinusoidally with time, a viscoelastic material will also respond with a sinusoidal strain for low amplitudes of stress. The strain response will have same frequency of the input stress but lagging behind by a phase angle, δ. The phase lag is due to the excess time necessary for molecular motions and relaxations to occur. Dynamic stress

and strain are given as

$$\sigma = \sigma_o \sin(\omega t + \delta), \qquad \varepsilon = \varepsilon_o \sin(\omega t) \tag{7.1}$$

where ω is the angular frequency. Therefore, stress can be divided into an in-phase component ($\sigma_o \cos\delta$) and an out-of-phase component ($\sigma_o \sin\delta$) and rewritten as

$$\sigma = \sigma_o \sin\omega t \cos\delta + \sigma_o \cos\omega t \sin\delta \tag{7.2}$$

Dividing stress by strain, two moduli are derived and defined as E' and E'' for the in-phase (real) and out-of-phase (imaginary) parts, respectively

$$E' = \frac{\sigma_o}{\varepsilon_o}\cos\delta, \qquad E'' = \frac{\sigma_o}{\varepsilon_o}\sin\delta \tag{7.3}$$

The two moduli, E' and E'', corresponds to the real and imaginary parts of the complex modulus:

$$E^* = E' + iE''. \tag{7.4}$$

The storage modulus E' describes the ability of the material to store potential energy and release it upon deformation, it is frequently associated with "stiffness" of a material and is related to the Young modulus. The loss modulus E'' is associated with energy dissipation in the form of heat upon deformation and it is related to "internal friction". The loss modulus is sensitive to different kinds of molecular motions, relaxation processes, transitions, morphology and other structural heterogeneities. Thus, the dynamic properties provide information at the molecular level to understanding the nanofiller/polymer mechanical behavior. The ratio between the loss modulus and the storage modulus represent a measure of the intrinsic damping of materials, named *loss factor* η:

$$\eta = \tan\delta = \frac{E''}{E'}. \tag{7.5}$$

Alternatively, a definition in terms of energy concepts can be used. With respect to steady state oscillation, η can be described as

$$\eta = \frac{D}{2\pi W} = \frac{\pi E'' x_o^2}{2\pi(\frac{1}{2}E' x_o^2)} = \frac{E''}{E'}, \tag{7.6}$$

where x_o is the amplitude of the steady state response; D stands for the energy dissipated by a system in a full cycle of steady state deformation (at any frequency), thus, D is a measure of the energy loss per radian; whereas W represents the energy stored on the purely elastic component of the system at the maximum deformation.
The loss factor is undoubtedly the most general of the measurement indexes. The equivalent damping ratio ξ is simply related to the other damping measures: $\eta = \tan\delta = 2\xi$ when damping levels are within $0 < \tan\delta < 0.14$.

7.2 Method

The mechanical and damping properties of the prepared nanocomposites were assessed via a campaign of DMA analysis. DMA tests were carried out using the ARES-G2 (TA Instruments), which is a rheometer but also a dynamic thermo-mechanical analyzer, here used to evaluate the variation of the storage modulus, loss modulus and loss factor within selected

ranges of strain and frequency. The storage modulus and damping ratio of the nanocomposites were measured during frequency and strain sweep tests, i.e, by varying the frequency and strain amplitude of the assigned displacement history in torsional mode. The torsional tests provided significant information about the damping capacity of the nanocomposites, also thanks to the shear stress state that initiated the CNT/matrix stick-slip phenomenon in the randomly oriented CNT nanocomposites with a significant localization around the contour of the samples cross sections.
The frequency sweep tests were conducted on a frequency range from 0.1 Hz to 80 Hz, at constant strain (0.0005) and temperature (25°C). The strain sweep tests were performed in the strain range from 0.0001 to 0.035 keeping constant the frequency at 1Hz and the temperature (25°C). The specimen prepared for the tests were rectangular bars with a length of 40 mm and a cross section of 1×9.5 mm^2. All tests were repeated for 5 specimens per each material to have more statistically meaningful data.

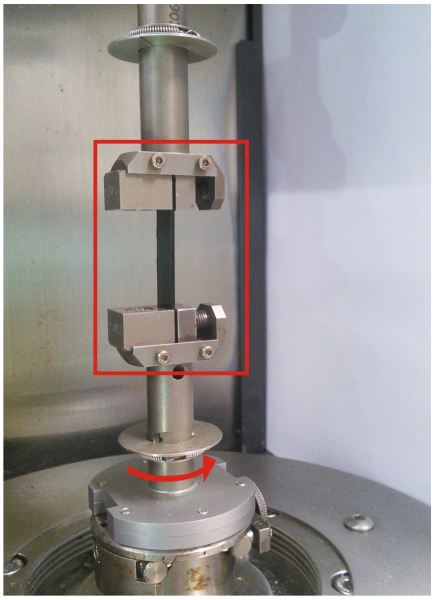

Figure 7.1: ARES-G2 DMA-rheometer (TA Instrument) for testing rectangular specimens in torsional mode.

7.3 DMA tests for CNT/thermoplastic nanocomposites

DMA strain and frequency sweep tests were carried out for PC and PBT nanocomposites with the two different types of CNTs, the MWNTs (NC7000) and the SWNTs (Tuball), respectively.

7.3.1 Frequency sweep tests

Frequency tests were carried out at a very low value of the shear strain, 0.0005, ensuring to be in the linear range. Figs. 7.2, 7.3, 7.4 and 7.5 show the trends for the shear storage modulus and the damping ratio at increasing values of the frequency for all PC and PBT nanocomposites samples.

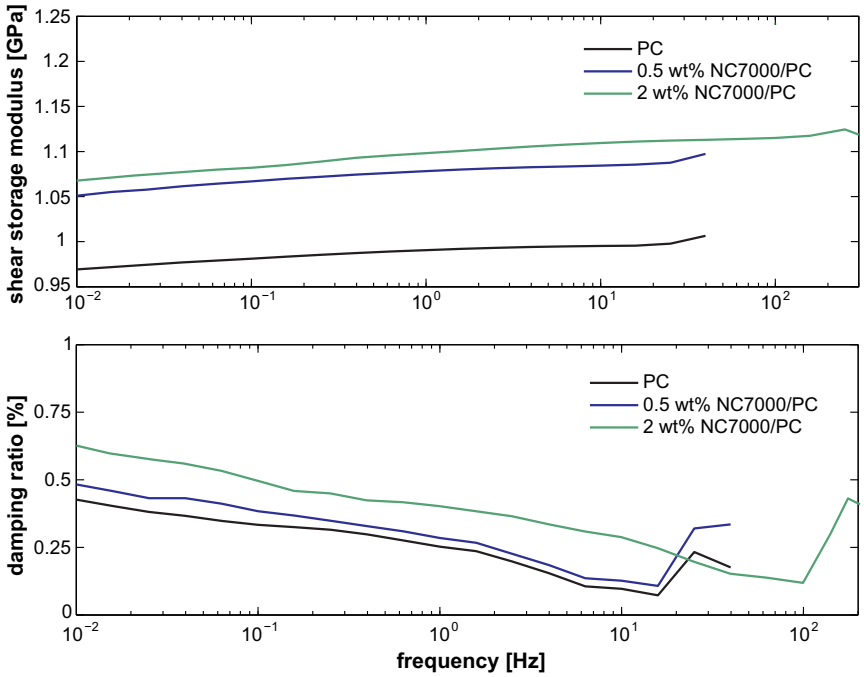

Figure 7.2: Frequency curves obtained from the frequency sweep tests for the NC7000/PC nanocomposites.

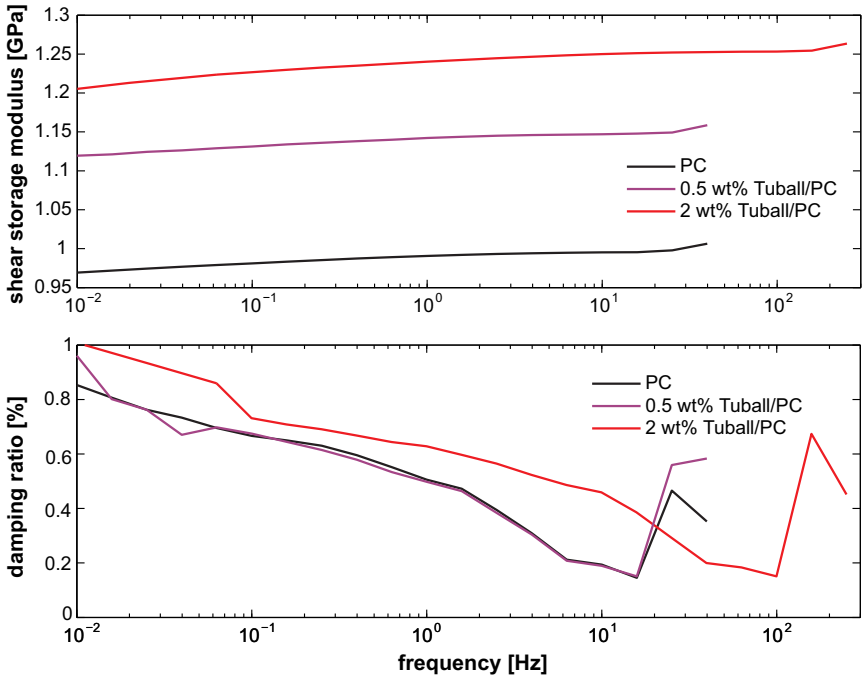

Figure 7.3: Frequency curves obtained from the frequency sweep tests for the Tuball/PC nanocomposites.

The low strain at which the tests were performed justifies the obtained low values of the damping ratio, although it is clearly observable that the damping capacity of the nanocom-

posites is slightly higher than that of the pure polymers even at such a low deformation. Furthermore, the augmentations of the storage modulus of the nanocomposites with respect to the polymers are significantly high. These enhancement in damping capacity and storage modulus reported for the nanocomposites are also independent of the frequency.

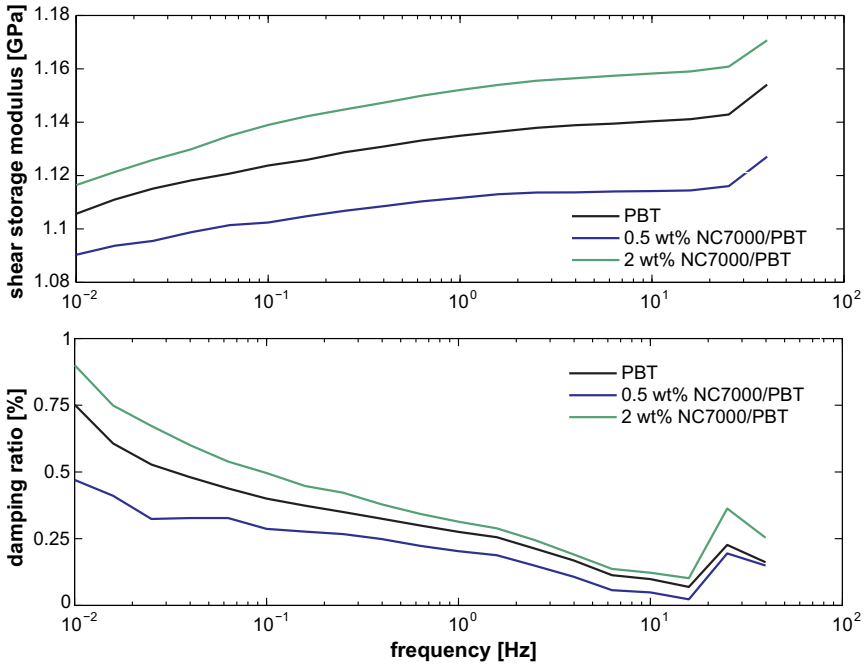

Figure 7.4: Frequency curves obtained from the frequency sweep tests for the NC7000/PBT nanocomposites.

7.3.2 Strain sweep tests

The dependence of the shear storage modulus on the dynamic shear strain of CNT thermoplastic nanocomposites and neat polymers is shown in Fig.7.6, for the polycarbonate nanocomposites, and in Fig.7.7, for polybutylene terephthalate nanocomposites, respectively.

At low values of the dynamic shear strain, the storage modulus in all the nanocomposites is significantly higher than the values for neat PC and PBT polymers. This is consistent with the theoretical expectations. Moreover, the storage modulus remains nearly independent of dynamic strain amplitude until a critical value, which represents the value at which permanent deformations starts to occur because of material degradation. The loss in storage modulus is likely due to a loss in the interfacial load transfer in the nanocomposites. In other words, the decrease in storage modulus with dynamic strain suggests that slippage initiates at this critical strain. Once the interfacial sliding between CNTs and polymers takes place, the reinforcing effect of CNTs started to be suppressed.
Indeed, assessment of the contribution of CNTs to composite stiffness at sufficiently low strains (below the critical sliding) is found in the frequency sweep tests, which are carried out at a strain value of 0.0005. In the elastic range the nanocomposites exhibit higher elastic moduli (storage moduli) than the pure polymers, since no interfacial damage occurred yet. At higher strain levels, the storage moduli of CNT composites drop to lower values due to

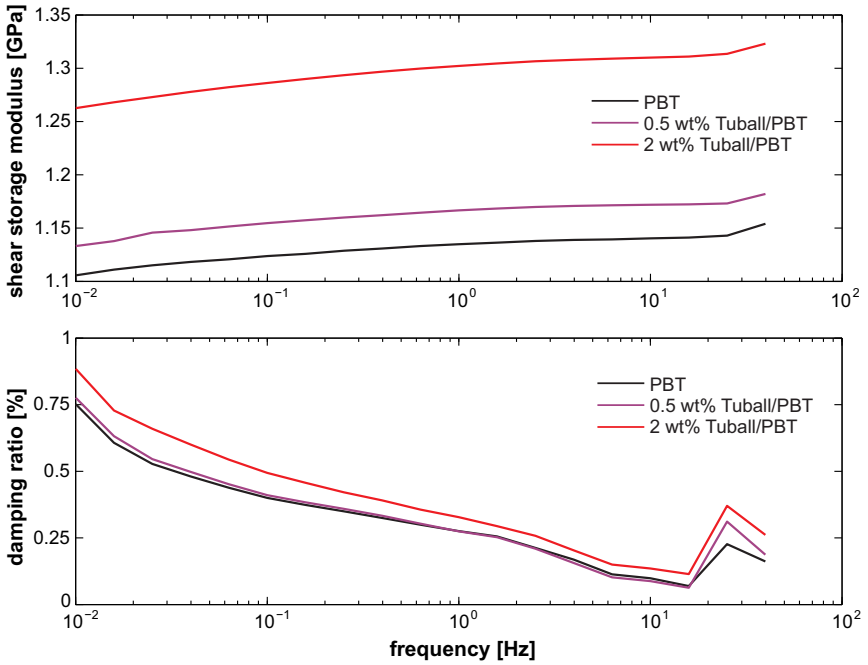

Figure 7.5: Frequency curves obtained from the frequency sweep tests for the Tuball/PBT nanocomposites.

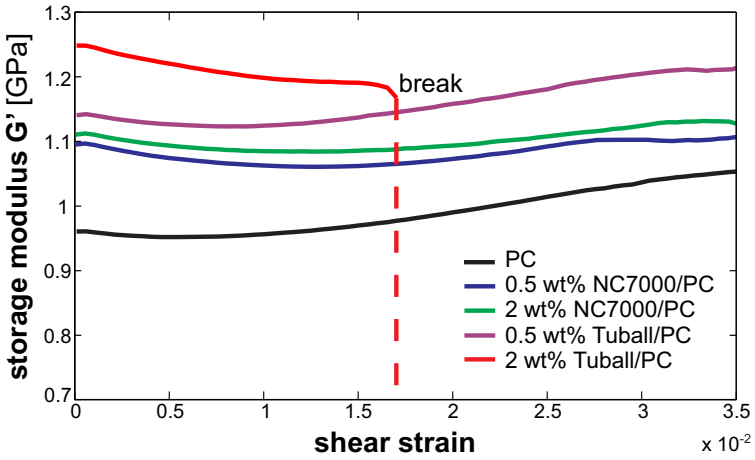

Figure 7.6: Storage modulus vs shear strain plots obtained from the strain sweep tests for the CNT/PC nanocomposites.

the interfacial slip, promoted by weak interfaces, together with other microstructural defects, such as CNT agglomeration.

Further evidence in support of the initiation of interfacial sliding at critical strain values is obtained by considering the variations of the damping capabilities of CNT/PC and CNT/PBT nanocomposites. As shown in Fig.7.8 and 7.9 for the PC nanocomposites, and in Fig.7.10 and 7.11 for the PBT nanocomposites, the damping ratios vary in a nonlinear fashion with dynamic strain amplitude in contrast to the nearly linear variations of the neat polymer. More specifically, at low strains, below the critical strain value, the measured damping ratios

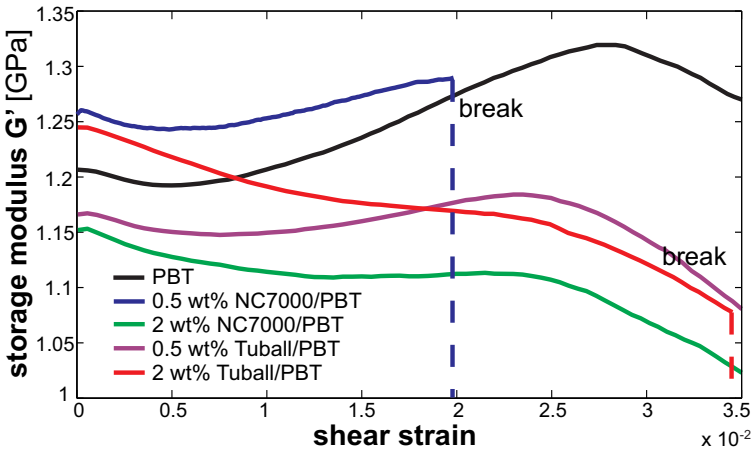

Figure 7.7: Storage modulus vs shear strain plots obtained from the strain sweep tests for the CNT/PC nanocomposites.

of nanocomposites are close to the values obtained in the matrices and, in some cases, damping is even lower than that reported in the polymers. This is because the CNT composites are stiffer that the neat matrices, in which the polymer chains show some mobility and readjustments, even at low strains. However, when the critical dynamic strain is reached, the energy dissipation in CNT composites is markedly enhanced and they rapidly increase with the dynamic strain.
By analyzing the trend of damping ratio versus shear strain amplitude a threshold strain of 0.0005 was found for NC7000/PC nanocomposite and a threshold strain of 0.001 for Tuball/PC nanocomposites, whereas in the CNT/PBT nanocomposites the critical strain value was 0.003 for both the NC7000 and Tuball CNT nanocomposites.

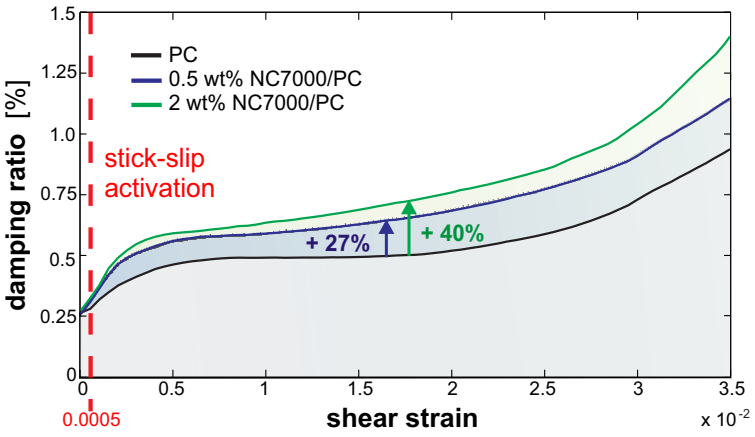

Figure 7.8: Damping ratio vs shear strain curves obtained from the strain sweep tests for the NC7000/PC nanocomposites.

Besides the dissipation at the interface through the stick-slip, the additional source of energy dissipation, reported as the increase in damping ratios for nanocomposites, could be stemmed from the dissipation phenomenon due to the matrix. Since it is assumed that the CNTs remain elastic even at large strains, the polymer chains start to slide one respect to the others, expecilly at the CNTs ends.

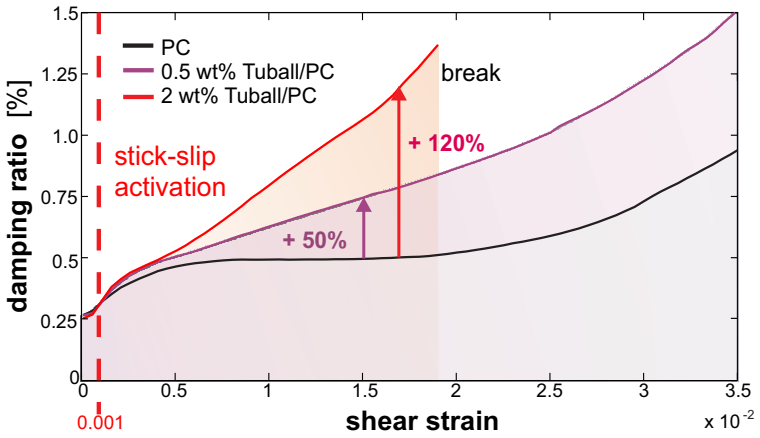

Figure 7.9: Damping ratio vs shear strain curves obtained from the strain sweep tests for the Tuball/PC nanocomposites.

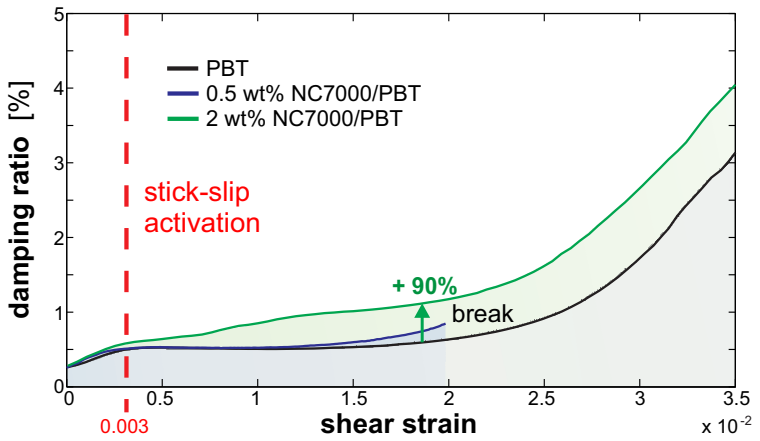

Figure 7.10: Damping ratio vs shear strain curves obtained from the strain sweep tests for the NC7000/PBT nanocomposites.

Furthermore, the way in which the two different CNTs affect the damping capacity of the nanocomposites is here highlighted. The NC7000 MWNTs are characterized by a low aspect ratio of L/D=155 while the Tuball SWNTs have a higher aspect ratio equal to L/D=2780. It is worth noting that CNTs with lower diameters and higher lengths lead to a better mechanical and dissipative response of the nanocomposite. By computing the available CNT/matrix interfacial surface area in the NC7000 CNT nanocomposites and in the Tuball CNT nanocomposites, it turns out that the interfacial surface area S_L in a reference volume of material with a specific amount of CNTs V_{rif}, is inversely proportional to the CNT radius:

$$S_L = \frac{2}{r_{CNT}} V_{rif}. \tag{7.7}$$

Hence, by adopting the SWNTs Tuball, a larger interfacial area will be available for the activation of the stick-slip, providing higher dissipation in the nanocomposites. When the same volume fraction of CNTs is considered, for two nanocomposites with same matrix and different type of CNTs, the ratio between the available CNT/matrix interfacial areas is computed to be $S_{Tuball}/S_{NC7000} = 5.55$. This means that S_L is 5.55 times higher in the Tuball

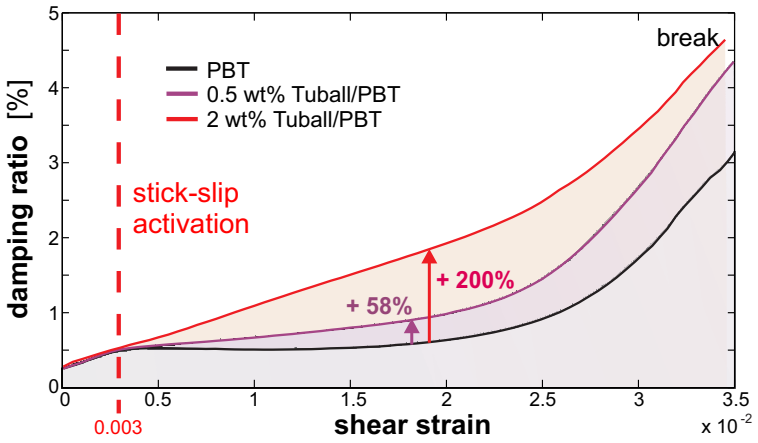

Figure 7.11: Damping ratio vs shear strain curves obtained from the strain sweep tests for the Tuball/PBT nanocomposites.

nanocomposites with respect to the NC7000 nanocomposites, thus explaining the significantly higher enhancement of damping capacity in all Tuball SWNTs nanocomposites.
To sum up, for low strain amplitudes, the damping capacity is nearly constant and is originated by viscosity. Above the critical strain, damping increases with the strain level as a result of the stick-slip between CNTs and polymer chains. Moreover, the experimental results show a significant improvement of the damping capacity by increasing the CNT weight fraction, although the CNT dispersion degree degrades. The highest increase in damping capacity was reported for the 2 wt% Tuball/PBT nanocomposite with an increase of 200% in damping compared to the neat PBT matrix.

Chapter 8

Micromechanical model update driven by experimental results

8.1 Introduction

The macroscopic mechanical and damping behavior of several CNT/polymer nanocomposites was extensively investigated through a campaign of monotonic and cyclic tensile tests and DMA strain and frequency sweep tests. On the other hand, the nanocomposites microstructural features were characterized via light microscopy, SEM and TEM analysis, estimating the actual CNT dispersion state and the actual CNTs morphology (aspect ratio, shape and curviness).
The most well-know micromechanical models, currently employed to describe the nanocomposite mechanical response, have shown some limitations due to ideal assumptions on microstructural material aspects, such as the assumptions of perfectly dispersed CNTs, perfect CNT/matrix interfaces, and do not account for the CNT agglomeration states, CNT curviness or the non-uniform distribution of the CNT aspect ratios inside the nanocomposites .
In particular, the CNT agglomeration state represents an important aspect arising out of the nanocomposite manufacturing process, as was addressed in several studies [70, 2]. Although enhancements have been experimentally achieved, an optimal CNT dispersion in the hosting matrices is still a challenge for the nanocomposites manufacturing.
In order to predict the effective elastic moduli of the CNT nanocomposites, some improvements and adjustments of the Eshelby-Mori-Tanaka model were proposed to account for the CNT agglomeration degree, the CNT curviness and length [78, 92, 69] in the light of the experimental observation.
However, the estimation and influence of the effective CNTs length, usually subject to shortening during the nanocomposite processing, is a crucial issue that has been highlighted only in a few works [49, 80, 50].
In this Chapter, an experiment-driven update of the already introduced Eshelby-Mori-Tanaka model is presented. The aim is to incorporate into this equivalent continuum model some key information extracted from the experimental data to optimize the accuracy of the mechanical properties estimation.

8.1.1 Some considerations on the experimental results

The mechanical and morphological characterizations dealing with three thermoplastic polymer nanocomposites with different CNTs aspect ratios and contents, highlighted the fact that the actual CNT aspect ratio distribution and the degree of dispersion within the hosting matrix are key factors to be incorporated at the modeling stage.
The three selected thermoplastic polymers – integrated with high aspect ratio SWNTs and low aspect ratio MWNTs – covered the large class of polymers, going from a commodity polymer (Polypropylene), to an amorphous engineering polymer with good mechanical properties (Polycarbonate), to the semi-crystalline high-performance engineering thermoplastic (Polybutylene Terephthalate).
Light microscopy analysis showed good macro-dispersion of the MWNTs with a low agglomerate area fraction A/A0, while the SWNTs tendency to agglomerate was more significant for increasingly higher weight fractions. Although this is a drawback for the SWNT nanocomposites, the substantially straight shape of the SWNTs versus the curved shape of the MWNTs is responsible for the better performance of SWNTs as reinforcement nanofiller. Moreover, TEM analyses provided information not only on the curviness of the CNTs, but also on the actual variability of the CNTs lengths in the nanocomposites. It was found that the effect of the reinforcement is more significant for high aspect ratio and straight CNTs that can offer a larger interfacial surface area for the load transfer. At the same time, as observed through DMA analysis, nanocomposites with SWNTs exhibit a significantly higher damping capacity thanks to the larger interfacial surface area that they provide. The straight, elongated high aspect ratio Tuball SWNTs have, in fact, a surface area which is 5.55 times larger than that of the curled, low aspect ratio NC7000 MWNTs, therefore the stick-slip dissipation phenomenon results to be more significant and diffused in the SWNT nanocomposites.
Thus, it can be stated that among all the factors influencing the behavior of the nanocomposites, the CNT aspect ratio, and in particular, its diameter is the dominant factor affecting the mechanical and dissipative response of the nanostructured materials. CNTs with small diameter, not only provide a large interface area available for the transmission of the stresses between the two composite constituents, but also provide large interfacial area for the stick-slip dissipation mechanism between CNTs and polymer chains.
In addition, the degree of the CNT dispersion has the highest impact on the maximum strain that the nanocomposite can withstand. Both mechanical tensile tests and DMA tests showed that nanocomposites with higher CNT agglomeration index break at lower strain values than those with good CNT dispersion.
The structure and the stiffness of the hosting matrix represent another relevant feature for the damping capacity of the nanocomposites. The polymer chain mobility may interfere with the activation of the interfacial stick-slip phenomenon; for example, when polymers are too flexible, they may absorb more energy and do not allow the concentrations of the stresses at the CNT/matrix interfaces, that will be not activated. On the contrary, if the polymer is too stiff, it may break before the stick-slip mechanism takes place.

8.2 Experiment-driven update of the equivalent constitutive model

To describe the nonlinear macroscopic response of nanocomposites materials, the equivalent constitutive equation proposed in Chapter 3 can be adopted:

$$\dot{\boldsymbol{T}} = \boldsymbol{L}_1 : \dot{\boldsymbol{E}} - \boldsymbol{L}_2 : \dot{\boldsymbol{E}}^{\mathrm{P}} \tag{8.1}$$

where

$$\boldsymbol{L}_1 := \boldsymbol{L}_{\mathrm{M}} : (\boldsymbol{I} + \phi_{\mathrm{C}}\, \boldsymbol{B} : [\![\boldsymbol{L}]\!]) \,, \qquad \boldsymbol{L}_2 := \phi_{\mathrm{C}}\, \boldsymbol{L}_{\mathrm{M}} : \boldsymbol{B} : \boldsymbol{L}_{\mathrm{C}} \,. \tag{8.2}$$

and

$$\boldsymbol{B} := (\boldsymbol{L}_{\mathrm{M}} + \phi_{\mathrm{M}}\, [\![\boldsymbol{L}]\!] : \boldsymbol{S})^{-1} \,. \tag{8.3}$$

while ϕ_C and ϕ_M are the CNT and matrix volume fractions, $\boldsymbol{I}$ is the identity tensor, $\boldsymbol{L}_C$ and $\boldsymbol{L}_M$ are the elastic tensors for the inclusions and the matrix respectively, $[\![\boldsymbol{L}]\!] = \boldsymbol{L}_C - \boldsymbol{L}_M$ is the elastic mismatch and $\boldsymbol{S}$ is the Eshelby tensor. This is a well-established approach to obtain the constitutive equations within the framework of Eshelby-Mori-Tanaka method, since the resulting equivalent elastic tensor $\boldsymbol{L}_1$ represents the equivalent elastic tensor obtained for a purely elastic two-phase composite [62, 12].
On the basis of the experimental results, some significant adjustments are envisioned for this equivalent constitutive theory, focusing the attention on the elastic properties of the nanocomposite materials, for which important experimental data were found.
In particular, in the work presented in Chap. 3, the Eshelby tensor was introduced through the simplified expression for cylindrical inclusions aligned along a principal direction. In order to account for the actual shape, geometry and orientation of the nanofiller, the Eshelby tensor is redefined and updated through the results of the morphological analysis. Moreover the CNT agglomeration degree is taken into account by scaling the effective value of the CNT volume fraction.

8.2.1 CNT aspect ratio and length distribution in the Eshelby tensor

The CNT morphology analysis via TEM characterization highlighted that the nanotubes length in the nanocomposites cannot be assumed to be constant, nor identified with the nominal length provided by the CNT manufacturers. Indeed, the shear mixing force applied during the melt compounding fabrication process has a shortening effect for the CNTs. This would lead to an overestimation of the nanocomposites effective elastic moduli. Therefore, both the SWNTs and MWNTs lengths are modeled as a probability density function, namely the GEV distribution law, introduced in Chap. 5.
The GEV density function is given as:

$$f(x;\mu,\sigma,\xi) = \frac{1}{\sigma}\left[1+\xi\left(\frac{x-\mu}{\sigma}\right)\right]^{(-1/\xi)-1} \exp\left\{-\left[1+\xi\left(\frac{x-\mu}{\sigma}\right)\right]^{-1/\xi}\right\} \tag{8.4}$$

where μ is the mean value of the CNT length data, σ is the standard deviation and ξ id the shape parameter.
Thus, the CNT length input parameter L is redefined according to the density functions obtained from TEM analysis (see Fig.8.1) and introduced in the expression the Eshelby tensor $\boldsymbol{S}$, that takes into account the shape and the geometry of the nanofiller.

Assuming the CNTs as ellipsoidal inclusions, their aspect ratios are denoted as:

$$e = \frac{a_3}{a_2}, \qquad g = \frac{a_2}{a_1}, \tag{8.5}$$

where a_1, a_2 and a_3 represent the principal axes of the ellipsoidal CNT, aligned along the local principal directions x_1, x_2 and x_3, respectively. The principal axis a_3 represents the

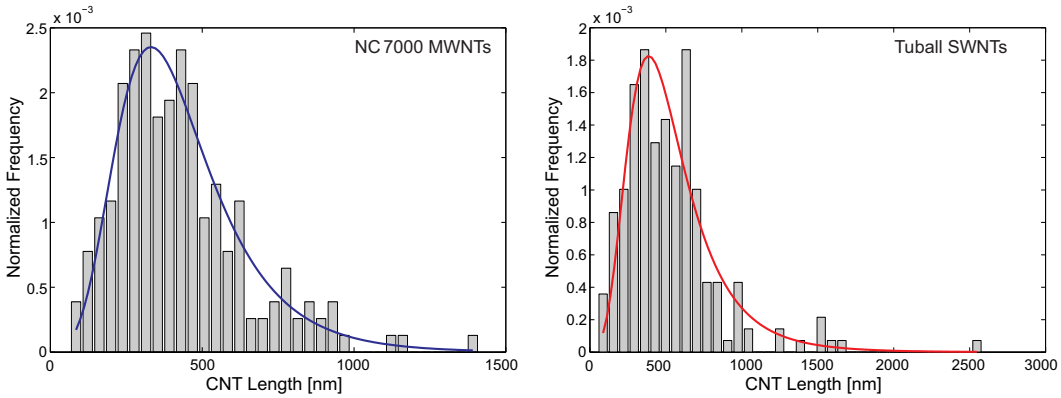

(a) NC7000 length distribution.

(b) Tuball length distribution.

Figure 8.1: CNTs length distributions approximated with the GEV probability density function. By fitting the data, the best CNT length distribution associated to the the NC7000 MWNTs was found for the parameters: $\mu = 338.16$, $\sigma = 156.56$, and $\xi = 0.044$; while the parameters for the Tuball SWNTs are $\mu = 407.17$, $\sigma = 202.59$, and $\xi = 0.107$.

CNT length L, a_2 is the diameter D of the CNT circular cross-section, and a_1 is equal to a_2, unless a shape factor ϵ would be considered to account for non perfectly cylindrical nanotubes. Hence, the ellipsoidal aspect ratio $e = L/D$ is equal to the CNT aspect ratio α, while the ellipsoidal aspect ratio is set to be $g \cong 1$ since it is assumed that the CNTs have a circular cross section.
To obtain the Eshelby tensor, the elliptic integrals and the depolarization factors must be defined as functions of the aspect ratios e and g, and the CNT Poisson ratio ν_C. For the complete expressions, see Mura [64].
However, according to the Eshelby theory, already described in Chap. 2, this is the case of a prolate ellipsoid since $a_1 \cong a_2 < a_3$. Thus, the Eshelby tensor can also be simplified by only one depolarization factor:

$$\Gamma = \frac{e}{2}\int_0^{+\infty} \frac{d\xi}{(\xi+1)^2(\xi+e^2)^{1/2}} = \frac{e}{4(\sqrt{e^2-1})^3}\left[2e\sqrt{e^2-1} + \ln\frac{e-\sqrt{e^2-1}}{e+\sqrt{e^2-1}}\right], \quad (8.6)$$

when $e > 1$. Thus, $\boldsymbol{S}$ in Voigt notation is given as:

$$\mathbf{S} = \begin{bmatrix} S_{1111} & S_{1122} & S_{1133} & 0 & 0 & 0 \\ S_{1122} & S_{1111} & S_{1133} & 0 & 0 & 0 \\ S_{3311} & S_{3311} & S_{3333} & 0 & 0 & 0 \\ 0 & 0 & 0 & (S_{1111}-S_{1122})/2 & 0 & 0 \\ 0 & 0 & 0 & 0 & S_{1313} & 0 \\ 0 & 0 & 0 & 0 & 0 & S_{1313} \end{bmatrix} \quad (8.7)$$

where its nonzero components are defined as follow, in terms of the depolarization factor Γ

$$\begin{aligned}
S_{1111} =& \frac{1}{8}\frac{13\Gamma - 3e^2 - 4e^2\Gamma + 8\Gamma\nu e^2 - 8\Gamma\nu}{(1-e^2)(1-\nu)},\\
S_{1122} =& -\frac{1}{8}\frac{e^2 + \Gamma - 4e^2\Gamma + 8\Gamma\nu e^2 - 8\Gamma\nu}{(1-e^2)(1-\nu)},\\
S_{1133} =& -\frac{1}{2}\frac{2e^2\Gamma - e^2 + \Gamma + 2\Gamma\nu e^2 - 2\Gamma\nu}{(1-e^2)(1-\nu)},\\
S_{3311} =& \frac{1}{8}\frac{e^2 + \Gamma - 4e^2\Gamma + 8\Gamma\nu e^2 - 8\Gamma\nu}{(1-e^2)(1-\nu)},\\
S_{3333} =& \frac{1 - 2e^2 + 4e^2\Gamma + -\Gamma + 8\nu e^2 - \nu - 2\Gamma\nu e^2 + 2\Gamma\nu}{(1-e^2)(1-\nu)},\\
S_{1313} =& -\frac{1}{4}\frac{e^2\Gamma + 2\Gamma - 1 + \Gamma\nu e^2 - \Gamma\nu - \nu e^2 + \nu}{(1-e^2)(1-\nu)},
\end{aligned} \tag{8.8}$$

In the present work, $\boldsymbol{S}$ was derived by adopting both the extended expressions (complete formulas for the Eshelby tensor in [64]) and the particularized expressions for the prolate ellipsoidal inclusions (presented above), and good agreement between both the results was found.

Once defined $\boldsymbol{S}$, the GEV normalized density function for the CNTs length $g(L;\mu,\sigma,\xi)$ can be introduced in the expression of the updated Eshelby tensor $\bar{\boldsymbol{S}}$ through an averaging operation:

$$\bar{\boldsymbol{S}} = \int_{L_1}^{L_2} \boldsymbol{S}(L)\, g(L;\mu,\sigma,\xi)\, dL \tag{8.9}$$

where L_1 and L_2 are the extreme values of the CNT length range estimated through the TEM analysis.

The expression of the modified Eshelby tensor $\bar{\boldsymbol{S}}$ can be introduced in Eq. 8.3 and subsequently into the expressions of the elastic and plastic tensor $\boldsymbol{L}_1$ and $\boldsymbol{L}_2$, respectively.

Elastic equivalent constitutive model. If we consider only the elastic part of the equivalent constitutive equation 8.1, $\boldsymbol{L}_1$ results to be equal to the elastic tensor derived from the Eshelby and Mori-Tanka model, already introduced in Chap. 6:

$$\boldsymbol{L} = \boldsymbol{L}_M + \phi_C \langle \bar{\boldsymbol{N}} \rangle \tag{8.10}$$

with

$$\boldsymbol{N} = [\![\boldsymbol{L}]\!] : \left(\boldsymbol{I} + \phi_M \bar{\boldsymbol{S}} : \boldsymbol{L}_M^{-1} : [\![\boldsymbol{L}]\!]\right)^{-1}. \tag{8.11}$$

In Eq. 8.10, the term enclosed in angle brackets represents the average over all orientations defined by the transformation from the inclusion-fixed frame to the global frame of the nanocomposite material domain.

The advantage of Eq. 8.10 is the significantly lower computational effort required to obtain $\boldsymbol{L}$ due to the fact that only $\boldsymbol{N}$ has to be averaged out over all possible CNT orientations. Indeed, for randomly oriented CNT nanocomposites, $\boldsymbol{N}$ must be first transformed in order to be expressed in the global frame as $\bar{\boldsymbol{N}}$, according to:

$$\bar{\boldsymbol{N}}_{ijkl} = \boldsymbol{c}_{ip}\boldsymbol{c}_{jq}\boldsymbol{c}_{kr}\boldsymbol{c}_{ls}\boldsymbol{N}_{pqrs} \tag{8.12}$$

where c_{ij} are the rotation tensors

$$\mathbf{c} = \begin{bmatrix} \cos\theta\cos\beta\cos\varphi - \sin\beta\sin\varphi & -\cos\theta\cos\beta\sin\varphi - \sin\beta\cos\varphi & \sin\theta\cos\beta \\ \cos\theta\sin\beta\cos\varphi + \cos\beta\sin\varphi & -\cos\theta\sin\beta\sin\varphi + \cos\beta\cos\varphi & \sin\theta\sin\beta \\ -\sin\theta\cos\varphi & \sin\theta\sin\varphi & \cos\theta \end{bmatrix} \tag{8.13}$$

Table 8.1: Young moduli and Poisson ratios for the nanocomposite constituents.

Material	Young Modulus [GPa]	Poisson Ratio
NC7000	900	0.1
Tuball	970	0.1
PP	1.45	0.42
PC	2.35	0.38
PBT	2.65	0.36

with β, θ, and φ representing the Euler angles (see Fig. 8.2).

Subsequently, $\bar{\boldsymbol{N}}$ can be averaged out over all directions given by the Euler angles as follows

$$\langle \bar{\boldsymbol{N}} \rangle = \frac{1}{8\pi^2} \int_0^{2\pi} \int_0^{\pi} \int_0^{2\pi} \bar{\boldsymbol{N}} \sin\theta \, d\varphi \, d\theta \, d\beta. \tag{8.14}$$

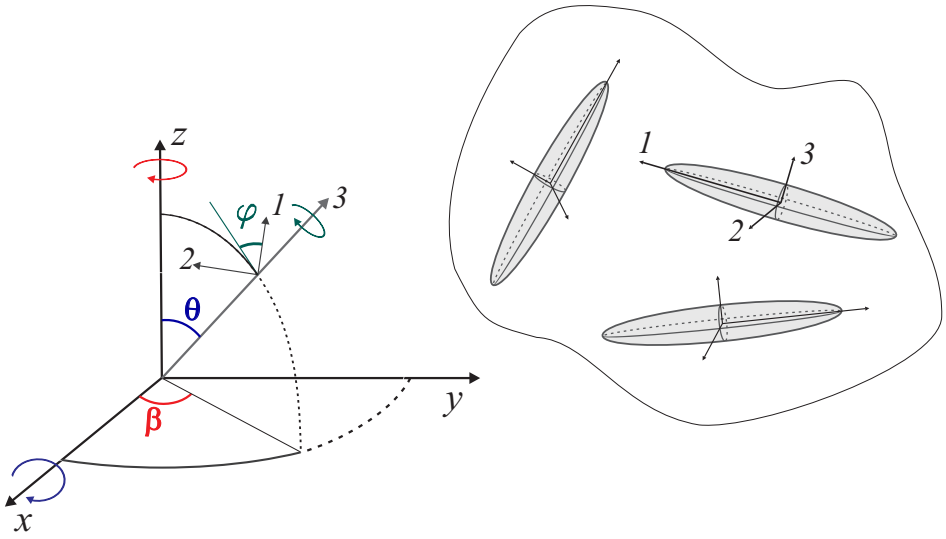

Figure 8.2: A random orientation of an inclusion is represented by the Eluler angles β, θ, and φ. The inclusion directions are expressed by the local axes *1*, *2*, *3*.

Elastic moduli estimation. The updated micromechanical model was employed to estimate the Young moduli of the CNT/PC and CNT/PBT nanocomposites and the predictions were compared with those of the classical Halpin-Tsai and Eshelby-Mori-Tanaka theories, described in Chap. 6.

The Young moduli [54] and Poisson ratios [16, 98] of the nanocomposites constituents adopted for the theoretical computations are reported in Table 8.1. The CNT length was initially set to be constant and equal to the nominal values, which are 1.5 μm for the MWNTs, and 5 μm for the SWNTs.

Subsequently an update of the actual CNT length distribution within the nanocomposites is considered and a much more significant agreement were found with the experimental data, as shown in Fig8.3.

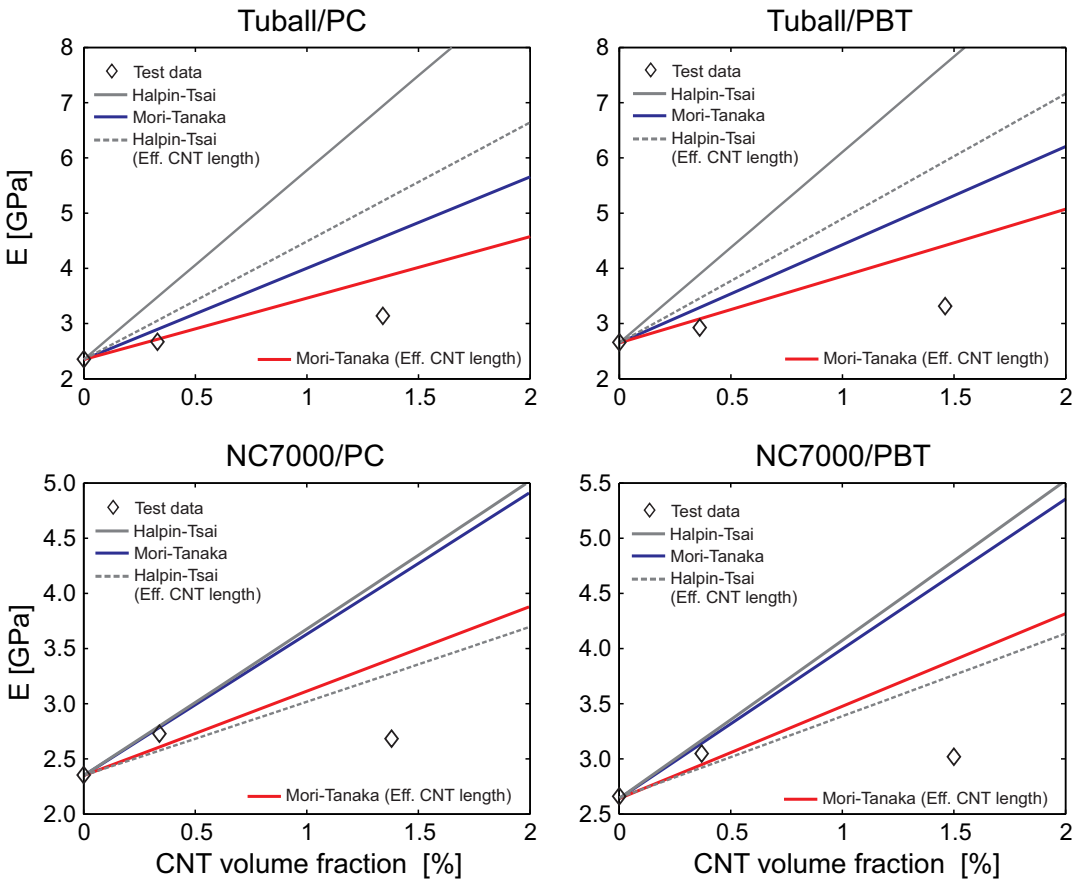

Figure 8.3: Predictions of the effective elastic moluli of the PC and PBT nanocomposites compared with the experimental data.

The predictions with the updated model are perfectly in agreement for the PC nanocomposites at low CNT volume fractions. However, increasing the CNT volume fraction, the theory predicts a linear augmentation of the Young modulus, which is not confirmed by the experimental results. This can be explained by the ideal assumption that the CNTs are all well-dispersed in the matrix and that a perfect bonding between the CNTs and the polymer is ensured.

By considering the morphological analysis on the CNT dispersion state of nanocomposites (Chap. 5), the CNT agglomeration area ratio A_{CNT}/A_0 reported for PC nanocomposite with low CNT content (0.5 wt%) is lower than 0.3%. This corresponds to a very good CNT dispersion degree since it is well accepted in the literature that if $A_{CNT}/A_0 < 1\%$, the CNT can be assumed to be well dispersed. For the other nanocomposites a higher state of CNT agglomeration is found and the potential of the CNT reinforcement is not completely expressed due to a reduction of the load transfer at the CNT/polymer interfaces.

As result, the updated model can work as an accurate tool for the description of the nanocomposite mechanical properties only if the nanofiller is well dispersed and there are no CNT agglomerates.

8.2.2 Scaling coefficient for the CNT volume fraction via the agglomeration index

Through the first adjustment of the nanofiller aspect ratio, the model improved their predictive capabilities, however the method still delivers a non negligible error in estimating the elastic moduli for higher values of the CNT content, due to the assumption of perfectly dispersed CNTs.
CNTs agglomeration is one of the most relevant issue to address during the fabrication process of CNT nanocomposites. In fact, it was found that when higher nanofiller contents are embedded in the polymer, an increasing CNT agglomerate area fraction is observed (see Fig. 8.4).

In order to better estimate the nanocomposite mechanical properties, a step forward is

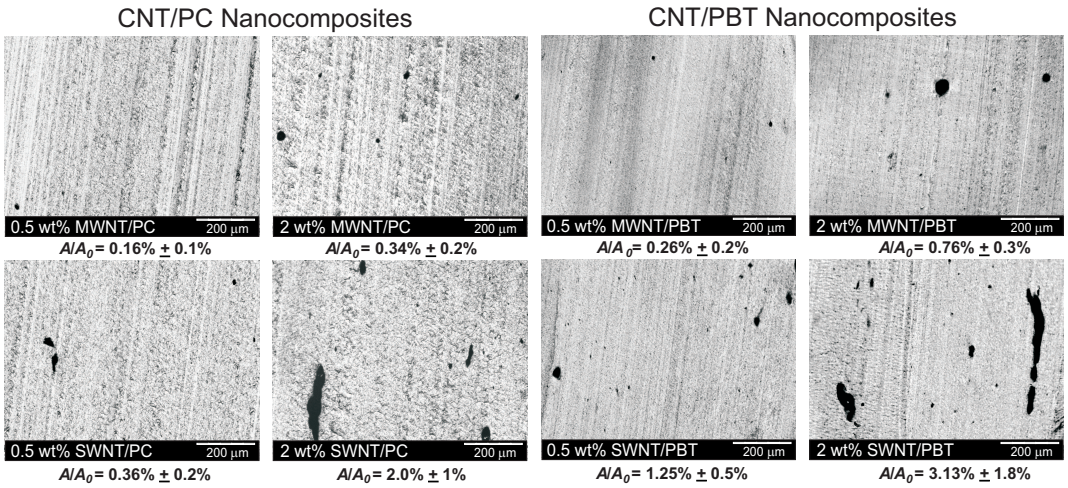

Figure 8.4: Light microscopy micrographs and corresponding area fraction for CNT/PC and CNT/PBT nanocomposites.

needed. It is necessary to account for the agglomeration state of the nanofiller by considering only the effective CNT volume fraction, here denoted by ϕ_D, which is defined as the CNTs portion that is actually well dispersed and exhibits good adhesion with the polymer chains. This leads to the substitution of the nominal CNT volume fraction ϕ_C with the effective well-dispersed CNT volume fraction ϕ_D in the expressions of the elastic and plastic tensors of Eq. 8.1 and in the particularized equivalent constitutive equation 8.10:

$$\boldsymbol{L} = \boldsymbol{L}_M + \phi_D \langle \bar{\boldsymbol{N}} \rangle \tag{8.15}$$

where

$$\boldsymbol{N} = [\![\boldsymbol{L}]\!] \left(\boldsymbol{I} + (1 - \phi_D) \bar{\boldsymbol{S}} \boldsymbol{L}_M^{-1} [\![\boldsymbol{L}]\!] \right)^{-1} . \tag{8.16}$$

The morphological analysis via the optical light microscopy can give a great contribution in understanding how to compute the effective ϕ_D. Indeed, an interesting measurement of the CNT macro-dispersion degree can be provided by the macro-dispersion index D, evaluated as the ratio of the dispersed volume fraction of CNTs to the whole CNT volume fraction.

The following expression is adopted [45]:

$$D := \frac{\phi_C - f\left(\frac{A_{CNT}}{A_0}\right)}{\phi_C} = \frac{\phi_D}{\phi_C}, \tag{8.17}$$

where f is the packing density of CNTs and represents the effective volume of the filler generally assumed equal to $f = 0.25$ for CNTs.
When D is closed to zero, it indicates a poor state of dispersion, while a dispersion index of 100% means that no agglomerates of size larger than 1 μm^2 can be found, indicating the best state of dispersion.
This allows to directly state a relationship between the nominal CNT volume fraction and the effective well-dispersed CNT volume fraction:

$$\phi_D = D\,\phi_C. \tag{8.18}$$

Therefore, the macro-dispersion index D works as a scaling factor for the CNT volume fraction, and it is expressed as a function of the CNT agglomeration area ratio $\mathrm{A}_{CNT}/\mathrm{A}_0 < 1\%$. The CNT agglomeration area ratio is a relatively fast data to obtain via optical light microscopy when a nanocomposite material is produced, and it was computed here for all the prepared nanocomposites.
A polynomial law can be associated to the CNT agglomerate area ratio A/A_0 as function of the increasing CNT nominal volume fraction ϕ_C:

$$\frac{A}{A_0} = 1 - b_1\phi_C + b_2\phi_C^2 + b_3\phi_C^3, \tag{8.19}$$

where b_1, b_2, and b_3 are coefficients to be derived through the LM analysis.

Elastic moduli estimation. By adopting ϕ_D as the effective CNT volume fraction, a further estimation of the Young modulus through the already adjusted model (with the CNT length distribution) can be performed.
Exploiting the experimental data collected through the LM analysis, the polynomial laws for the CNT agglomerate area fraction A/A_0 given in Eq.8.19 were found for both the CNT types, and the associated macrodispersion index D was given as function of the nominal CNT volume fraction, as shown in Fig. 8.5. The determined values for the coefficients of the A/A_0 functions are $b_1 = 0.725$, $b_2 = 0$ and $b_3 = 0.087$ for the NC7000 MWNTs, and $b_1 = 0.809$, $b_2 = 1.188$ and $b_3 = 0$ for the Tuball SWNTs. The degree of the polynomial law can be assumed to be lower or higher than three; however, it was found that this level of approximation was the best compromise for the examined cases.

Finally, by assuming the effective CNT agglomeration state in the nanocomposites, the modified Eshelby-Mori-Tanaka model predictions can provide a perfect match with the experimental data, especially for Tuball nanocomposites, as shown in Fig.8.6. The mismatch shown between the experimental data and predicted elastic moduli in NC7000 nanocomposites at higher CNT contents (see Fig.8.6 and 8.7) can be addressed to the wavy shape of the MWNTs, as shown in the TEM images. Indeed, the stiffening effect of the carbon nanotubes in nanocomposites is generally reduced by the CNT waviness [69]. The NC7000 waviness affects the elastic modulus in a more relevant way at higher CNT concentrations. This remarkable result is another proof of the importance of the designated nanofiller, whose morphology must be investigated for an accurate and correct selection of the constituents before the nanocomposite preparation.

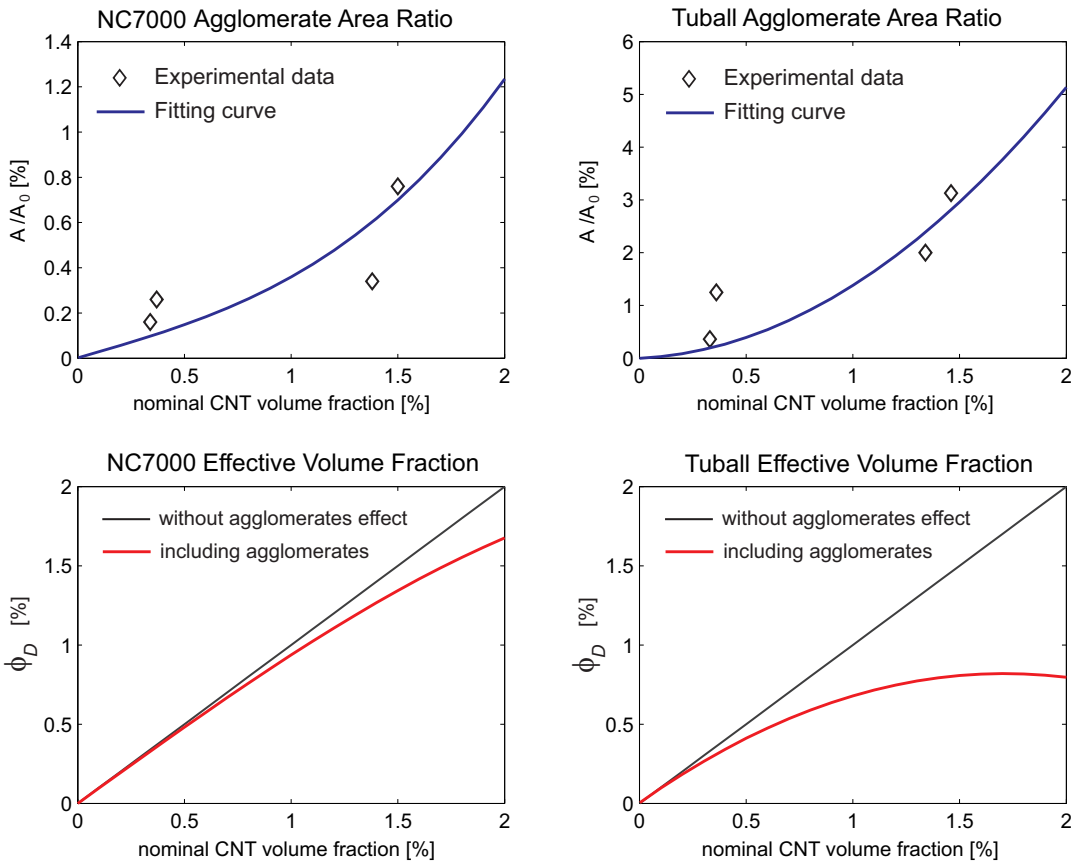

Figure 8.5: The CNT agglomerate area ratio polynomial laws are obtained by fitting the experimental data collected via LM analysis and the macrodispersion index D was adopted to compute the effective CNT volume fractions ϕ_D. The laws are given as functions of the nominal CNT volume fraction ϕ_C.

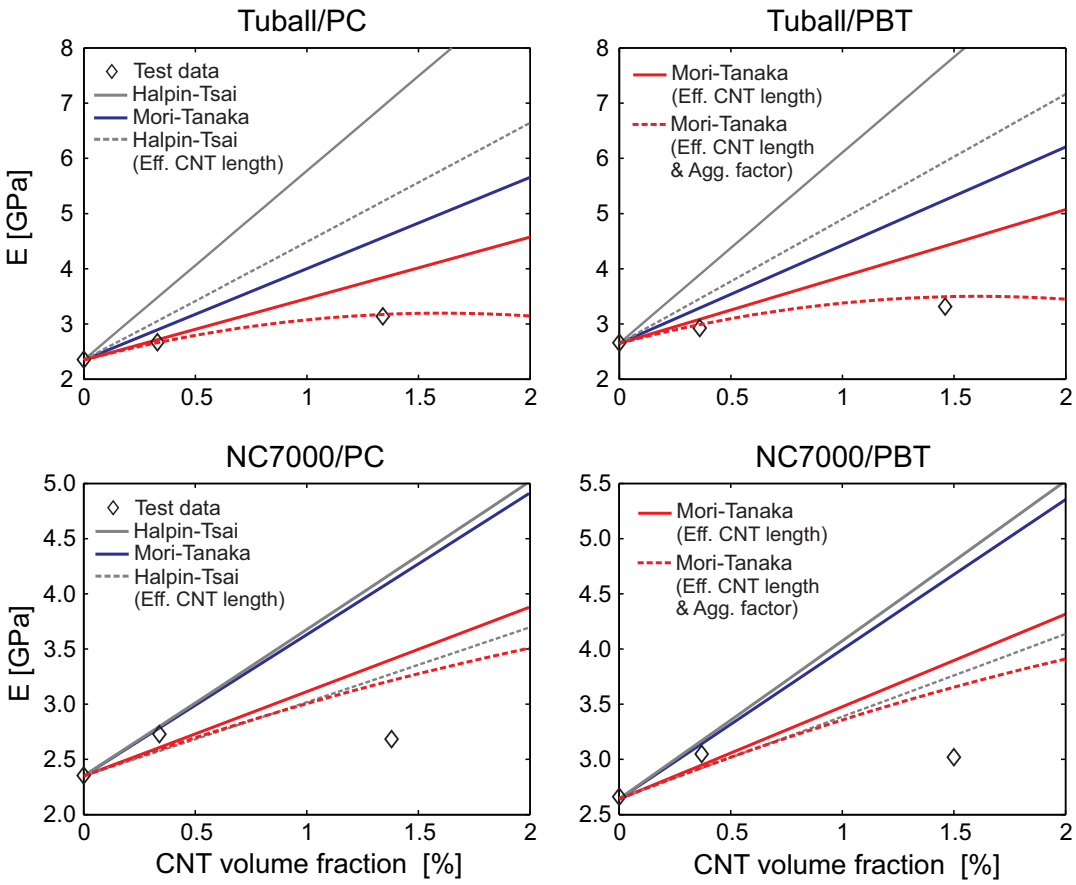

Figure 8.6: Predictions of the effective elastic moluli of the PC and PBT nanocomposites compared with the experimental data.

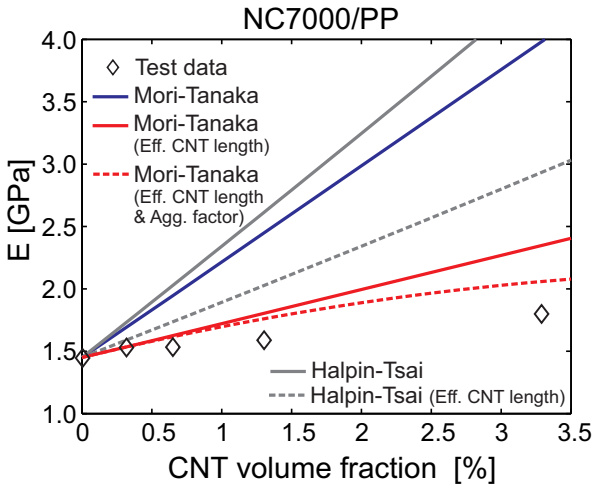

Figure 8.7: Predictions of the effective elastic moluli of the PP nanocomposites compared with the experimental data.

Chapter 9

Conclusions

9.1 The proposed equivalent constitutive model for CNT nanocomposites

In this work a new mesoscale constitutive model, describing the mechanical and damping response for nanocomposite materials, was presented. The developed theory is a combination of the mean-field homogenization method based on the Eshelby equivalent inclusion theory, the Mori-Tanaka average stress method, and the concept of inhomogeneous inclusions with inelastic eigenstrain due to Mura [64]. The idea of inhomogeneous inclusions which can exhibit inelastic eigenstrains as opposed to the purely homogeneous problem is the key to describe the shear stick-slip between CNTs and matrix by means of incremental plastic eigenstrains in the inclusions. The rate-independent evolution of the plastic eigenstrains is regulated by a power law based on a micromechanical adjustment of the von Mises stress function computed as the second invariant of the deviatoric part of the stress discontinuity across the interfaces. The resulting constitutive law, although used in a simplified one-dimensional context, shows the advantage of being directly implemented using time-integration schemes within standard finite element codes, and does not require the implementation of return mapping algorithms, which usually becomes the most meaningful part of the overall computational costs in elasto-plasticity.

The theory allows to investigate both mechanical and damping properties of the CNT nanocomposites. The specific damping capacity is computed as the ratio between the energy dissipated per cycle and the elastic energy stored during the loading phase considering a nanocomposite embedding a uniform dispersion of discontinuous, perfectly aligned or randomly oriented CNTs.

The hysteretic energy dissipation has been investigated by a variety of monotonic and cyclic shear tests. Comparisons of the theoretical results with experimental data – available from the literature and directly obtained during this work – indicate that energy dissipation from interfacial friction in CNT-reinforced polymers is subject to a considerable enhancement with respect to that of the pristine polymer matrices. An improvement in damping capacity, corresponding to an augmentation of 200% was observed via DMA tests for thermoplastic engineering nanocomposites with 1.35% volume fraction of randomly oriented SWNTs (2 wt% Tuball/PBT nanocomposites).

From the numerical sensitivity and parametric studies, it was shown that the damping ratio is

highly sensitive to the strain amplitude in the strain-controlled cyclic tests with a localization of maximum dissipation in the neighborhood of given strain amplitudes, a typical feature of rate-independent hysteresis. At the same time, it was found that (i) increasing the interfacial shear strength causes the onset of hysteretic dissipation to take place at higher strains, (ii) the maximum dissipation is attained at higher stains and (iii) the decrease of damping capacity at higher strains is much milder than the cases governed by lower interfacial shear strengths. This finding indicates that both strength and dissipation can be concurrently achieved by increasing the shear strength so long as the material is forced to sustain suitable operational ranges of strains.
Furthermore, the conducted study shows that the way the main constitutive parameters affect the mechanical response of the nanocomposites is highly complex and nonlinear. This means that optimization methods are necessary to identify the optimum set of parameters that maximizes the vibrational energy dissipation of the nanocomposite. The conducted gradient-free optimization analysis allowed to determine the key parameters so that the interfacial friction between the nanotubes and the polymer can be fully developed during cyclic motion within the operational strain amplitudes.

9.2 Experimental findings and tuning of the model features

The proposed analytical model aims to be a design tool for the mechanical and damping properties of the material. To achieve this goal an extensive experimental campaign of mechanical tests was carried out on a large variety of CNT nanocomposites, specifically prepared during this research work.
To broaden the study towards different and untackled aspects of nanocomposites mechanical behavior, four different polymers and two different kinds of nanotubes were employed during the samples fabrication. A representative thermosetting polymer (i.e., the epoxy resin), and three thermoplastic polymers covered the large spectrum of polymers, going from commodity polymers (polypropylene referred as PP), to amorphous engineering polymers with good mechanical properties (polycarbonate referred as PC), to the semi-crystalline and crystalline high-performance engineering polymers (polybutylene terephthalate referred as PBT and epoxy resin). High-aspect ratio Tuball SWNTs and low-aspect ratio NC7000 MWNTs were employed as fillers in order to explore the effects of CNT length, diameter and shape of the nanotubes on the macroscopic response of the nanocomposites. The morphology of the inner structure of the nanocomposite was investigated via light microscopy, scanning electron microscopy and transmission electron microscopy. The definition of the CNT dispersion, distribution and agglomeration degrees were crucial to achieve a better understanding of the mechanical and damping properties of the nanocomposites. In particular, a CNT macrodispersion index and a CNT agglomerate area ratio were computed and adopted for the definition of a scaling factor multiplying the CNT volume fraction in the model. This allowed to account for the actual volume fraction of well-dispersed CNT, effectively contributing to the mechanical and damping response of the nanocomposite.
The TEM analysis on the actual CNT length distribution led to the estimation of the effective aspect ratios of the CNTs, pointing out that there is a significant shortening effect of the CNTs length during the fabrication processes. This finding was taken into account by providing an updated expression of the Eshelby tensor in the stick-slip model, and thereby the actual shape and geometry of the randomly oriented CNTs was considered.
The characterization of the mechanical and damping properties via tensile and DMA tests

confirmed the role of the CNTs as effective nanofiller reinforcement for the polymers, when the CNTs exhibit specific morphological features. Indeed, it was found that the effect of the CNT reinforcement is generally more significant for high aspect ratio SWNTs that provide a larger interfacial surface area for the load transfer. This finding highlighted the CNT aspect ratio as key parameter for the optimization of the CNT nanocomposites features. Another interesting outcome obtained through DMA tests, was that the dominant factor affecting the mechanical and dissipative response of the nanostructured materials actually is the diameter of the nanotubes, which contributed even more than the CNT length in the performance of the materials. Indeed, CNTs with smaller diameter provide a larger interface area for a given volume fraction to be employed in load transfer, as well as a higher surface area for the stick-slip dissipation mechanism between CNTs and polymer chains.
Furthermore, an interesting trend of the damping capacity versus strain amplitude, obtained via the DMA analysis, revealed that the interfacial shear strength (ISS) can be identified experimentally. This may allow a future tuning of the effective ISS range values to be introduced into the model and, hence, regulate the activation of the interfacial stick-slip phenomenon.
Finally, the polymer structure and the stiffness of the hosting matrix has also an influence on the damping capacity of the nanocomposites, since the polymer chain mobility can interfere with the activation of the interfacial stick-slip phenomenon. Polymers that are too flexible absorb more energy and do not facilitate the sliding motion at the CNT/matrix interfaces, which could thus require more energy; on the contrary, if the polymer is too stiff, it may fail before the stick-slip mechanism takes place.
To achieve this level of understanding of the nanocomposites mechanical behavior, further analysis and experimental tests are required. The present experimental study can provide important guidelines for future developments and experimental campaigns.

9.2.1 Effective elastic moduli

The reported experimental outcomes revealed the strong connections between the morphology and the mechanical properties of the nanocomposites. The morphological investigations were exploited to improve the theoretical estimation of the effective elastic moduli of the nanocomposite materials.
Analyzing the acquired experimental data, an average improvement of 25% of the elastic moduli was found in all nanocomposites compared to the neat polymers, by adding a 2 wt% of CNTs. Due to a loss in the material ductility, a reduction of the elongation at break was also reported with the increase of the CNT content in the nanocomposites and an augmentation of the ultimate tensile strength was found in all samples, except for the materials that report an early break due to non optimal CNT dispersion.
The significant findings obtained through the extensive light and electron microscopy analysis allowed to perform a fine tuning of the equivalent constitutive model. In particular, some of the assumptions inherent in the most popular multi-pase model have been removed, such as the perfect dispersion of the CNTs and the perfectly bonded interphases between the constituents of the composite. The real agglomeration and dispersion state of the CNTs was taken into account by determining the actual CNT dispersed volume fraction. In addition, the effective shape and geometry of the CNTs was considered together with the actual distribution of the CNTs length, by modifying the Eshelby tensor. The variability of the CNT aspect ratio within the nanocomposite were considered through a probability density function, describing the variation of the CNT length in the nanocomposites, on the bases of TEM analysis.
The effective elastic moduli were estimated by adopting the proposed equivalent constitu-

tive model and the predictions were compared with those of the classical Halphin-Tsai and Mori-Tanaka models. The elastic moduli estimated through the updated model were much more aligned with the acquired experimental data, than the predictions provided by the more conventional classical approaches.

9.2.2 Future developments

During the dynamical mechanical analysis an interesting finding was obtained. By investigating the damping capacity of nanocomposite materials with increasing dynamic shear strain, the CNT nanocomposites revealed to be characterized by a critical strain value, after which a rapid raising trend of the damping capacity is observed. This behavior compared to the one of the polymer matrix could suggests that, the identified critical strain value corresponds to a critical stress after which the activation of the CNT/matrix interfacial sliding motion takes place. The value of the shear stress in the nanocomposites, associated to the critical shear strain, may allow the estimate of the actual interfacial shear strength (ISS), which is defined as the shear stress threshold value at the CNT/matrix interfaces at which the stick-slip mechanism occurs.
In the nonlinear constitutive model presented in Chap. 3, the ISS value regulates the arising of the plastic strain filed, $\boldsymbol{E}^*$, accounting for the interfacial stick-slip. A future development of the model could include a revision of the eigenstrain evolution law through the experimental data together with the choice of a more feasible range of the ISS parameter, to identify by experimental tests. Further experimental DMA tests are currently ongoing in tensile and bending modes, to capture the hysteretic dissipation arising from the interfacial stick-slip and several attempts are being made to fit the experimental data with the numerical simulations based on the proposed model.
Finally, in order to better investigate the damping capability of nanocomposites, the viscous part of the response delivered by the polymer matrix may be addressed. The present work focused the attention on the dissipation due to stick-slip phenomena localized at the CNT/matrix interfaces, thus the visco-elastic behavior of the polymers was not considered. However, phenomenological models are currently being employed in order to capture and describe the viscous hysteresis of the neat polymers, and consequently extend the theoretical model.
At the moment, the developed tool integrates only the dissipation energy due to the frictional sliding of the two constituents and does not consider the viscoelastic or elasto-plastic energy dissipation due to the constitutive behavior of the hosting matrix materials.
The introduction of new modeling features, such as the employment of more feasible values of the ISS parameter, the matrix viscosity, or deterioration factors for the Young modulus of the equivalent material, can further improve the macroscopic response prediction of nanocomposite materials.

Bibliography

[1] Ajayan P. M., Suhr J., Koratkar N., 2006. Utilizing interfaces in carbon nanotube reinforced polymer composites for structural damping. J. Mater. Sci. 41, 7824–7829.

[2] Alig I., Pötschke P., Lellinger D., Skipa T., Pegel S., Kasaliwal G.R., Villmow T., 2012. Establishment, morphology and properties of carbon nanotube networks in polymer melts. Polymer 53, 4–28.

[3] Anumandla V., Gibson R. F., 2006. A comprehensive closed form micromechanics model for estimating the elastic modulus of nanotube-reinforced composites. Compos. Part A-Appl. S. 37, 2178–2185.

[4] Ashrafi B., Hubert P., 2006. Modeling the elastic properties of carbon nanotube array/polymer composites. Compos. Sci. Technol. 66, 387–396.

[5] Auad M. L., Mosiewicki M. A., Uzunpinar C., Williams R. J.J., 2009. Single-wall carbon nanotubes/epoxy elastomers exhibiting high damping capacity in an extended temperature range. Compos. Sci. Technol. 69, 1088–1092.

[6] Avilés F., Cauich-Rodriguez J.V., Moo-Tah L., May-Pat A., R. Vargas-Coronado A., 2009. Evaluation of mild acid oxidation treatments for MWCNT functionalization. Carbon, 47, 2970–2975.

[7] Bal s., Samal S. S., 2007. Carbon nanotube reinforced polymer composites – A state of the art. Bull. Mater. Sci., 30, 379–386.

[8] Barai P., Weng G., 2011. A theory of plasticity for carbon nanotube reinforced composites. Int. J. Plasticity 27, 539–559.

[9] A. R. Bhattacharyya, P. Ṕotschke, 2006. Mechanical Properties and morphology of melt-mixed PA6/SWNT composites: effect of reactive coupling. Macromol. Symp., 233, 161–169.

[10] Breton Y., Desarmot G., Salvetat J.P., Delpeux S., Sinturel C., Beguin F., Bonnamy S., 2004. Mechanical properties of multiwall carbon nanotubes/epoxy composites: influence of network morphology. Carbon, 42, 1027–1030.

[11] Basiricó L., Lanzara G., 2012. Moving towards high-power, high-frequency and low- resistance CNT supercapacitors by tuning the CNT length, axial deformation and contact resistance. Nanotechnology 23, 305–401.

[12] Benveniste Y., 1987. A new approach to the application of Mori–Tanaka's theory in composite materials. Mech. Mater. 6, 147–157.

[13] Buldum A., Lu J. P., 1999. Atomic scale sliding and rolling of carbon nanotubes. Phys. Rev. Lett. 83, 5050–5053.

[14] Chaboche J. L., 2008. A review of some plasticity and viscoplasticity constitutive theories. Int. J. Plasticity 24, 1642–1693.

[15] Chen C.H., Cheng C.H., 2009. Effective elastic moduli of misoriented short-fiber composites. Int. J. Solids Struct. 33, 2519–2539.

[16] W. Chen, H. Cheng, Y. Liu, Radial mechanical properties of single-walled carbon nanotubes using modified molecular structure mechanics. Comput. Mat. Sci., 47 (2010) 985–993.

[17] Ci L., Ryu Z., Jin-Phillipp N.Y., Ruhle M., 2006. Investigation of the interfacial reaction between multiwalled carbon nanotubes and aluminum. Acta Mater. 54, 5367–5375.

[18] Doghri I., Ouaar A., 2003. Homogeneization of two-phase elasto-plastic composite materials and structures. Study of tangent operators, cyclic plasticity and numerical algorithms. Int. J. Solids Struct. 40, 1681–1712.

[19] Doghri I., Adam L., Bilger N., 2010. Mean-field homogeneization of elasto-viscoplastic composites based on a general incrementally affine linearization method. Int. J. Plasticity 26, 219–238.

[20] Dwaikat M.M.S., Spitas C., Spitas V., 2011. A model for elastic hysteresis of unidirectional fibrous nano composites incorporating stick-slip. Mat. Sci. Eng. A-Struct. 530, 349–356.

[21] Eshelby J.D., 1957. The determination of the elastic field of an ellipsoidal inclusion, and related problems. P. Roy. Soc. A-Math. Phy. 241, 376–396.

[22] Eshelby J.D., 1959. The elastic field outside an ellipsoidal inclusion. P. Roy. Soc. A-Math. Phy. 252, 561–569.

[23] Eitan A., Fisher F.T., Andrews R., Brinson L.C., Schadler L.S., 2006. Reinforcement mechanisms in MWCNT-filled polycarbonate. Composites Sci. and Tech., 66, 1159–1170.

[24] Formica G., Lacarbonara W., Alessi R., 2009. Vibrations of carbon nanotube-reinforced composites. J. Sound Vib. 329, 1875–1889.

[25] Formica G., Lacarbonara W., 2009. Eshelby continuum model of CNT-reinforced composites in free vibrations. In: Proc. XIX Congress AIMETA, Ancona.

[26] Formica G., Lacarbonara W., 2012. Debonding model of carbon nanotubes in a nanostructured composite. Compos. Struct. 96, 514–525.

[27] Formica G. , Taló M., Lacarbonara W., 2014. Nonlinear modeling of carbon nanotube composites dissipation due to interfacial stick-slip. Int. J. of Plasticity, 53, 148–163.

[28] Frankland S. J. V., Harik V. M., 2003. Analysis of carbon nanotube pull-out of a polymer matrix. Surf. Sci. Lett. 525, 103–118.

[29] Fraternali F., Blesgen T., Amendola A., Daraio C., 2011. Multiscale mass-spring models of carbon nanotube foams. J. Mech. Phys. Solids 159, 89–102

[30] Gardea F., Glaz B.,Riddick J., Lagoudas D. C., Naraghi M., 2015. Energy dissipation due to interfacial slip in nanocomposites reinforced with aligned carbon nanotubes. ACS Appl. Mater. Interfaces, 7, 9725–9735.

[31] Gibson R.F., 1994. Principles of composite material mechanics. McGraw-Hill, New York.

[32] Gibson R. F., Ayorinde E. O., Wen Y.F., 2007. Vibrations of carbon nanotubes and their composites: a review. Compos. Sci. Technol. 67, 1–28.

[33] Gonzalez C., Llorca J., 2000. A self-consistent approach to the elasto-plastic behavior of two-phase materials including damage. J. Mech. Phys. Solids 48, 675–692.

[34] Gou J., Minaie B., Wang B., Liang Z., Zhang C., 2004. Computational and experimental study of interfacial bonding of single-walled nanotube reinforced composites. Comp. Mater. Sci. 31, 225–236.

[35] Guhados G., Wan W. K., Sun X., Hutter J. L., 2007. Simultaneous measurement of Young and shear moduli of multiwalled carbon nanotubes using atomic force microscopy. J Appl. Phys., 101, 3514–3521.

[36] Guo S., Kang G., Wang B., Zhang J., 2013. A cyclic-visco-plastic constitutive model for time-dependent ratchetting of particle-reinforced metal matrix composites. Int. J. Plasticity 40, 101–125.

[37] Halphin J. C., Kardos J. L., 1976. The Halpin-Tsai equations: a review. Polymer Engineering and Sci. 16 - 5.

[38] Hill R., 1965. A self-consistent mechanics of composite materials. J. Mech. Phys. Solids 13, 213–222.

[39] Holscher H., Schwarz U.D., Zworner O., Wiesendanger R., 1998. Consequences of the stick-slip movement for the scanning force microscopy imaging of graphite. Phys. Rev. B 57, 2477–2481.

[40] Hu Y., Shen J., Li N., Ma H., Shi M., Yan B., Huang W., Wang W., Ye M., 2010. Comparison of the thermal properties between composites reinforced by raw and amino-functionalized carbon materials. Composite Sci. and Technol., 70, 2176–2182.

[41] Huang. Y., Tangpong X.W., 2010. A distributed friction model for energy dissipation in carbon nanotube-based composites. Commun. Nonlinear Sci. Numer. Simulat. 15, 4171–4181.

[42] Ju J. W., Sun L. Z., 1999. A novel formulation for the exterior-point Eshelby tensor of an ellipsoidal inclusion. J. Applied Mechanics, 66, 570–574.

[43] Ju J.W., Sun L.Z., 2001. Effective elastoplastic behavior of metal matrix composites containing randomly located aligned spheroidal inhomogeneities. Part I: micromechanics-based formulation. Int. J. Solids Struct. 38, 183–201.

[44] Kao C.C., Young R.J., 2009. Modeling the stress transfer between carbon nanotubes and polymer matrix during cyclic deformation. IUTAM Symposium on Modeling Nanomaterials and Nanosystems, 211–220.

[45] Kasaliwal G., Göldel A., Pötschke P., 2009. influence of processing conditions in small-scale melt mixing and compression molding on the resistivity and morphology of polycarbonate-MWNT composites. J.Appl. Polymer Sci., 112, 3494–3509.

[46] Khan S.U., Li C. Y., Siddiqui N.A., Kim J.-K., 2011. Vibration damping characteristics of carbon fiber-reinforced composites containing multi-walled carbon nanotubes. Compos. Sci. Technol. 71, 1486–1494.

[47] Kim K.T., Cha S.I., Hong S.H., Hong S.H., 2006. Microstructures and tensile behavior of carbon nanotube reinforced Cu matrix nanocomposites. Mater. Sci. Eng. A-Struct. 430, 27–33.

[48] Kim B. R., Lee H. K., 2010. Closed form solution of the exterior-point Eshelby tensor for an elliptic cylindrical inclusion. J. Applied Mechanics, 77 - 2.

[49] Krause B, Mende M, Petzold G, Boldt R, Pötschke P. Characterization of dispersibility of industrial nanotube materials and their length distribution before and after melt processing, in: D. Tasis (Ed.). Carbon Nanotube-Polymer Composites. Cambridge:UK Royal Society of Chemistry; 2013.

[50] Krause B., Mende M., Petzold G., Boldt R., Pötschke P., 2012. Methoden zur Charakterisierung der Dispergierbarkeit und Längenanalyse von Carbon Nanotubes. Chemie. Ingenieur. Technik. 84, 263–271.

[51] Iijima S., 1991. Helical microtubules of graphitic carbon. Nature, 354, 56.

[52] Lacarbonara W., Vestroni F., 2003. Nonclassical responses of oscillators with hysteresis. Nonlinear Dynam. 32, 235–258.

[53] Lanzara G., Chang F.K., 2009. Design and characterization of a carbon-nanotube-reinforced adhesive coating for piezoelectric ceramic discs. Smart Mater. Struct. 18, 1–18.

[54] Laua K.-T., Chiparab M., Linga H.-Y., Huic D., 2004. On the effective elastic moduli of carbon nanotubes for nanocomposite structures. Composites: Part B. 35, 95–101.

[55] Li X., Levy C., Agarwal A., Datye A., Elaadil L., Keshri A. K., Li M., 2009. Multifunctional carbon nanotube film composite for structure health monitoring and damping. The Open Construct. Building Technol. J. 3, 146–152.

[56] Lin R.M., Lu C., 2010, Modeling of interfacial friction damping of carbon nanotube-based nanocomposites. Key Eng. Mat. 334, 705–708.

[57] Liu A., Wang K.W., Bakis E.C., 2010. Damping characteristics of carbon nanotube-epoxy composites via multiscale analysis. In: Proc. 51^{th} AIAA/ASME/ASCE/AHS/ASC Structures, Structural Dynamics and Materials Conference. Orlando, USA.

bibitemLiu11 Liu A., Wang K.W., Bakis E.C., 2011. Effect of functionalization of single-wall carbon nanotubes (SWNTs) on the damping characteristics of SWNT-based epoxy composites via multiscale analysis. Compos. Part A 42, 1748–1755.

[58] Loos M. R., Pezzin S. H., Amico S. C., Bergmann C. P., Coelho L. A. F., 2008. The matrix stiffness role on tensile and thermal properties of carbon nanotubes/epoxy composites. J. Mater. Sci. 43, 6064–6069.

[59] Ma P.C., Siddiqui N.A., Marom G., Kim J.K., 2010. Dispersion and functionalization of carbon nanotubes for polymer-based nanocomposites: a review. Compos. Part A 41, 1345–1367.

[60] Ma P.C., Kim J.K., 2011. Carbon Nanotubes for Polymer Reinforcement. CRC Press, New York, USA.

[61] Man Y., Li Z., Zang Z., 2009. Interfacial friction damping characteristics in MWNT-filled polycarbonate composites. Front. Mater. Sci. China 3, 266–272.

[62] Mori T., Tanaka K., 1973. Average stress in matrix and average elastic energy of materials with misfitting inclusions. Acta Metall. Mater. 21, 571–574.

[63] M´uller M. T., Krause B., Kretzschmar B., Pötschke P., 2011. Influence of feeding conditions in twin-screw extrusion of PP/MWCNT composites on electrical and mechanical properties. Composites Sci. and Tech., 71, 1535–1542.

[64] Mura T., 1987. Micromechanics of defects in solids. Martinus Nijhoff, The Netherlands.

[65] Namilae S., Chandra N., 2005. Multiscale model to study the effect of interfaces in carbon nanotube-based composites. J. Eng. Mater. – T ASME 127, 222–232.

[66] Nemat-Nasser S., Hori M., 1993. Micromechanics: Overall Properties of Heterogeneous Materials. North-Holland Series in Applied Mathematics and Mechanics.

[67] Odegard G.M., Gates T.S., Wise K.E., Park C., Siochi E.J., 2003. Constitutive modeling of nanotube-reinforced polymer composites Compos. Sci. Technol. 63, 1671–1687.

[68] Ogasawara T., Tsuda T., Takeda N., 2011. Stress-strain behavior of multi-walled carbon nanotube/PEEK composites. Compos. Sci. Technol. 71, 73–78.

[69] J. Pan, L. Bian, H. Zhao, Y. Zhao, 2016. A new micromechanics model and effective elastic modulus of nanotube reinforced composites. Comp. Mater. Sci. 113, 21–26.

[70] Pegel S., P´otschke P. ,Petzold G. ,Alig I., Dudkin S. M. ,Lelinger D., 2009. Dispersion, agglomeration, and network formation of multi-walled carbon nanotubes in polycarbonate melts. Polymer, 49, 974–984.

[71] Pettermann H.E., Planskensteiner A.F., Bohm H.J., Rammerstorfer F.G., 1999. A thermo-elasto-plastic constitutive law for inhomogeneous materials based on an incremental Mori Tanaka approach. Comput. Struct. 71, 197–214.

[72] Pierard O., Gonzalez C., Segurad J., LLorca J., Doghri I., 2007. Micromechanics of elasto-plastic materials reinforced with ellipsoidal inclusions. Int. J. Solids Struct. 44, 6945–6962.

[73] Rajoria H., Jalili N., 2004. Determination of strength and damping characteristics of carbon nanotube-epoxy composites. In: Proc. 2004 ASME Int. Mech. Eng. Congress & Exposition. Anaheim, CA.

[74] Rajoria H., Jalili N., 2005. Passive vibration damping enhancement using carbon nanotube-epoxy reinforced composites. Compos. Sci. Technol. 65, 2079-2093.

[75] Sahooa N. G., Ranab S., Chob J. W., Li L., Chana S. H., 2010. Polymer nanocomposites based on functionalized carbon nanotubes. Progress in Polymer Sci., 35, 837–867.

[76] Savvas D. N., Papadopulus V., Papadrakakis M., 2012. The effect of interfacial shear sterngth on damping behavior of carbon nanotube reinforced composites. Int. J. Solids Struct. 49, 3823–3837.

[77] Simo J.C., Hughes T.J.R., 2000. Computational inelasticity. Springer-Verlag, USA.

[78] Shi D.L., Feng X.Q., Huang Y.Y., Hwang K.C., Gao H., 2004. The effect of nanotube waviness and agglomeration on the elastic property of carbon nanotube-reinforced composites. J. Eng. Mater. Technol. 126, 250–257.

[79] Slosberg M., Kari L., 2003. Testing of nonlinear interaction effects of sinusoidal and noise excitation on rubber isolator stiffness. Polym. Test. 22, 343–351.

[80] Socher R., Krause B., Müller M. T., Boldt R., P´otschke P., 2012. The influence of matrix viscosity on MWCNT dispersion and electrical properties in different thermoplastic nanocomposites. Polymer, 53 495–504.

[81] Storn R., Price K., 1997. Differential Evolution: A simple and efficient heuristic for global optimization over continuous spaces. J. Global Optimization 11, 341–359.

[82] Suhr J., Koratkar N., Ajayan P., 2004. Damping characterization of carbon nanotube thin films. Proc. SPIE–Smart Struct. and Mater. 2004: Damping and Isolation 5386, 153–161.

[83] Suhr J., Koratkar N. A., Keblinski P., Ajayan P., 2005. Viscoelasticity in carbon nanotube composites. Phys. Rev. Lett. 4, 134–137.

[84] Suhr J., Koratkar N. A., 2008. Energy dissipation in carbon nanotube composites: a review. J. Mater. Sci. 4, 4370–4382.

[85] Sun L.Z., Ju J.W., 2001. Effective elastoplastic behavior of metal matrix composites containing randomly located aligned spheroidal inhomogeneities. Part II: applications. Int. J. Solids Struct. 38, 203–225.

[86] Sun L., Warren G.L., OŔeilly J.Y. , Everett W.N., Lee S.M., Davis D., Lagoudas D., Sue H.-J., 2008. Mechanical properties of surface-functionalized SWCNT/epoxy composites. Carbon, 46, 320–328.

[87] Sun L., Gibson R.F., Gordaninejad F., Suhr J., 2009. Energy absorption capability of nanocomposites: a review. Compos. Sci. Technol. 69, 2392–2409.

[88] Sun G., Zheng L., Zhou J., Zhang Y., Zhan Z., Pang J.H.L., 2013. Load-transfer and mechanical reliability of carbon nanotube fibers under low strain rates. Int. J. Plasticity 40, 56–64.

[89] Teo E. H.T., Yung W.K.P., Chua D.H.C., Tay B.K., 2007. A carbon nanomattress: a new nanosystem with intrinsic, tunable damping properties. Adv. Mater. 19, 2941–2945.

[90] Thostenson E. T., Chou T. W., 2003. On the elastic properties of carbon nanotube-based composites: modeling and characterization. J. of Physics D: Applied Physics, 36, 573–582.

[91] Treacy M.M. J., Ebbesen T. W., Gibson J. M., 1996. Exceptionally high Young's modulus observed for individual carbon nanotubes. Nature, 381 678–680.

[92] Tsai C.H., Chang C.J., Wang K., Zhang C., Liang Z., Wang B., 2012. Predictive model for carbon nanotube-reinforced nanocomposite modulus driven by micromechanical modeling and physical experiments. IIE Transactions 44, 590–602.

[93] Tsuda T., Ogasawara T., Deng F., Takeda N., 2011. Direct measurements of interfacial shear strength of multi-walled carbon nanotube/PEEK composite using a nano-pullout method. Compos. Sci. Technol. 71, 1295–1300.

[94] Weng G.J., 1984. Some elastic properties of reinforced solids, with spherical reference to isotropic ones containing spherical inclusions. Int. J. Eng. Sci. 22,845–856.

[95] Weng G., 2009. A homogenization scheme for the plastic properties of nanocrystalline materials Rev. Adv. Mater. Sci. 19, 41–62.

[96] Yang S., Yu S.,Ryu J., Cho J., Kyoung W., Han D., Cho M., 2013. Nonlinear multiscale modeling approach to characterize elastoplastic behavior of CNT/polymer nanocomposites considering the interphase and interfacial imperfection. Int. J. Plasticity 41, 124–146.

[97] Zhao Y. H., Weng G.J., 1990. Effective elastic moduli of ribbon-reinforced composites. J. Appl. Mech. 57, 158–167.

[98] P. Zhao, G. Shi, Study of Poisson ratios of graphene and single-walled carbon nanotubes based on an improved molecular structural mechanics model, Tech. Science Press. SL., 5 (2011) 49–58.

[99] Zhou X., Shin E., Wang K.W., Bakis C.E., 2004. Interfacial damping characteristics of carbon nanotube-based composites. Compos. Sci. Technol. 64, 2425–2437.

[100] Zhou X., Wang K.W., Bakis C.E., 2004. The investigation of carbon nanotube-based polymers for improved structural damping. Proc. SPIE – Smart Struct. and Mater. 2004: Damping and Isolation 5386, 162–173.